

Quantum Molecular Dynamics of Guest Molecules in Supramolecular Complexes

Kuldeep Singh Panesar

School of Physics & Astronomy
University of Nottingham

Thesis submitted to the University of Nottingham
for the degree of Doctor of Philosophy

· December 2008 ·

Abstract

The quantum motion of guest molecules has been studied in a variety of calixarene host-guest complexes, and in an endohedral fullerene complex.

The guest molecules of the calixarene complexes studied each comprise weakly hindered methyl groups, which undergo rotation via quantum tunnelling, even at cryogenic temperatures. The rotational motion of the guest methyl-groups has been studied by making temperature and frequency-dependent measurements of proton T_1 , using field-cycling NMR, thus revealing the spectral density functions of the magnetic dipole-dipole interaction.

Crystallographically inequivalent methyl-group environments have been identified and characterised in *p-tert*-butylcalix[4]arene(1:1)toluene, *p-tert*-butylcalix[4]arene (1 : 1) γ -picoline and *p*-isopropylcalix[4]arene(2:1)*p*-xylene. In many of the calixarene complexes the proton spin-lattice relaxation has been observed to be strongly dependent on the thermal history of the sample. Temperature-dependent measurements of proton T_1 in samples of *p-tert*-butylcalix[4]arene(1:1)toluene with partially deuterated guest molecules reveal a systematic reduction in T_1 at low temperatures with increased degree of deuteration.

Calixarene and fullerene host-guest complexes have been identified as having a potential application in cryogenic MAS-NMR as cryorelaxor complexes, capable of being attached to a large biomolecule and encouraging proton spin-lattice relaxation. The suitability of the calixarene complexes for use in this capacity has been investigated by measuring the temperature-dependence of proton T_1 at low temperatures.

The quantised rotational and translational motion of dihydrogen confined within an open-cage fullerene—namely, aza-thio-open-cage-fullerene (ATO CF)—has been revealed by inelastic neutron scattering (INS) measurements. The splitting of excited rotational and translational states, due to the low symmetry of the ellipsoidal fullerene cavity, has been directly measured. Assignment of the peaks observed in the INS spectrum has been aided by analysis of the Q -dependence of excitation bands. The thermodynamics of ortho- and parahydrogen have been investigated via temperature dependence measurements. INS measurements have allowed the anisotropic rotational potential experienced by the H_2 rotor to be determined.

Acknowledgements

First and foremost, I would like to thank my supervisor, Prof. A.J. Horsewill, for his guidance and assistance over the past three years. During this time I have had the good fortune of working with a number of collaborators, whose contributions to this thesis have been invaluable. I would like to thank the group of Prof. M.H Levitt at the University of Southampton, especially Francesco Cuda, Alain Danquigny and Dr. Marina Carravetta, and Dr. Stephan Rols and Dr. Mark Johnson at Institut Laue-Langevin. Thanks to my fellow colleagues in the Quantum Molecular Dynamics group, Cheng Sun and Ilya Frantsuzov, for the numerous discussions; I can only hope they were as useful to you as they have been for me. Thanks also to Dr. Abdellah Aibout, and to Dr. Daniel Noble for showing me the ropes. This thesis would not have been possible without the expert support of the talented technical staff in the School of Physics and Astronomy, including Chris Pallender, David Holt, and Bob Chettle and his team.

I would like to acknowledge all of the teachers and individuals who have all played a part in inspiring, and enabling me to pursue the path of higher education, including the staff of St. Giles Middle School and Nicholas Chamberlaine Comprehensive School, particularly Mrs. Barbara Patch, Mr. Robert Jelley, Mr. Ian Frogget, Mr. Tony Forsythe, Mr. David Oddy, Mr. Peter Cambridge, and Mrs. Mary Bell. Thanks to Prof. M.E. Smith and Prof. J.R. Owers-Bradley for all of the advice, and to Dr. Nina Babbra for blazing the trail.

On a more personal note, I would like to acknowledge all of the friends that have made my time in Nottingham so enjoyable. Thanks especially to my good housemates Douglas Ashton, Myanna Duncan, Lester Hedges and to Alec Knight, for suggesting that I should study in this fair city. The boys in office C20 have consistently offered distractions of the welcome

and unwelcome kind, for which I am mostly grateful. One could not ask for a nicer bunch of colleagues than the splendid folks in ‘Ana’s tea-room crew’. Thanks to the staff and students of the Sir Peter Mansfield Magnetic Resonance Centre for helping me settle in. To my fellow warriors in the David Jephcote XI and the Physics post-graduate cricket team, it has been a pleasure to go into battle alongside you. Thanks to the cast and crew of the post-graduate theatre production of ‘Metamorphoses’ for a “truly lovely” experience. Thanks to Matt & Baz, and to Myanna & Alex for providing a roof over my head when I needed it! Dr. Paul Guerry: big yourself up.

Closer to home, thanks to all of the friends and families who have supported my family over the years. Special thanks to the late Mr. Malkit Singh Sagoo and family.

To my brothers, Hardeep and Jagdeep; “We family, baby!”. Thanks for looking out for your little brother.

Finally, I would like to thank my parents for their unwavering support and love. I would not be here without your countless sacrifices and hard work; I am forever indebted to you.

Contents

1	Introduction	1
1.1	Calixarenes and fullerenes	2
1.2	cryoMAS NMR	3
1.3	Quantum molecular motion	4
1.3.1	Methyl-group rotation	4
1.3.2	Dynamics of confined H ₂	6
1.4	Spin-symmetry species	6
1.5	Thesis layout	7
2	Theory	8
2.1	NMR fundamentals	8
2.1.1	Nuclear spin	9
2.1.2	Zeeman effect	9
2.1.3	Larmor precession	11
2.1.4	Interaction between a magnetic moment and a RF field	12
2.1.5	Bulk magnetisation	14
2.1.6	Bloch equations	16
2.1.7	Free induction decay	17
2.2	Spin-lattice relaxation	20
2.2.1	Two-level system	20
2.2.2	Correlation functions and spectral density functions	22
2.2.3	Two-spin system	23
2.3	Methyl-group dynamics	27
2.3.1	Rotational Hamiltonian	28
2.3.2	Rotational eigenstates	29
2.3.3	Spin-symmetry species	31
2.3.4	Relaxation rate	32

2.4	INS fundamentals	36
2.4.1	Scattering cross-section	37
2.4.2	Fermi pseudo-potential and scattering length	38
2.4.3	Coherent and incoherent scattering	39
2.5	Dynamics of confined H ₂	41
3	Experimental Details	44
3.1	Field-cycling NMR	44
3.1.1	Field-cycling magnet	44
3.1.2	Cryostat and VTI	46
3.1.3	NMR spectrometer	47
3.1.4	Probes	50
3.1.5	Pulse sequences	51
3.1.6	FID processing	53
3.1.7	Data analysis	56
3.2	INS measurements	56
3.2.1	Primary spectrometer	58
3.2.2	Secondary spectrometer	59
3.2.3	Time-focused INS	61
3.2.4	Spectrometer configurations	62
4	CH₃ rotation in calixarene complexes	64
4.1	Calixarene samples	64
4.2	Effect of thermal history on T_1	66
4.3	Rotation of <i>p</i> -xylene methyl groups in a calixarene host-guest complex	68
4.3.1	Structure	68
4.3.2	Thermal history effects	68
4.3.3	Methyl group dynamics in an annealed sample	72
4.4	Rotation of toluene methyl groups in a calixarene host-guest complex	77
4.4.1	Thermal history effects	77
4.4.2	Methyl-group dynamics in an annealed sample	78
4.5	Rotation of γ -picoline methyl groups in a calixarene host- guest complex	82
4.5.1	Thermal history effects	83
4.5.2	Methyl group dynamics in an annealed sample	83

4.6	The effect of host molecule deuteration on proton T_1	89
4.6.1	Temperature dependence of T_1	90
4.6.2	Calculation of the dipolar coupling constant	92
4.7	T_1 measurements in other calixarene complexes	95
4.8	Discussion and Summary	105
5	Quantum dynamics of confined H₂	110
5.1	Structure	111
5.2	Energy level diagram	112
5.3	INS Results	114
5.3.1	Temperature dependence of rotational sub-levels . . .	118
5.3.2	Calculation of the rotational potential	122
5.3.3	Q -dependence of rotational and translational peaks . .	123
5.4	Discussion and summary	128
6	Summary and Concluding Remarks	131

Chapter 1

Introduction

Supramolecular chemistry is an interdisciplinary science that brings together chemistry, physics and biology. In 1967 Charles J. Pedersen discovered a class of molecules that he dubbed the *crown ethers* [1, 2]. Pedersen demonstrated the ability of these electrically-neutral, ring-shaped molecules to form stable complexes with a variety of metal ions via an ion-dipole interaction between the metal ion and the oxygen atoms of the polyethers. This pioneering work signified a paradigm-shift in the world of chemistry. Having mastered chemistry of the molecule and ‘hard’ covalent bonds, chemists began to address the chemistry of complexes held together by non-covalent ‘soft’ interactions. It is for this reason that supramolecular chemistry is often described as ‘chemistry beyond the molecule’ [3].

Taking inspiration from the myriad of polymolecular systems and structures in Nature that owe their function or structure to reversible, non-covalent bonding (e.g. substrate-protein binding, enzymatic reactions, antigen-antibody binding, hydrogen-bonding in DNA [4]), synthetic chemists have developed a number of molecular classes that exploit intermolecular interactions in order to form host-guest complexes. Electrostatic interactions, hydrogen-bonding, van der Waals forces, hydrophobic effects, and π - π interactions between delocalised electrons in aromatic rings may all be utilised by the synthetic chemist in order to design novel, ‘tailored’ host molecules [5].

1.1 Calixarenes and fullerenes

The molecular complexes that serve as the focus of this thesis belong to either the *calixarenes* [6] or *fullerenes* [7]. Calixarenes are macrocyclic compounds, comprising several phenolic monomer units. The structure of calixarene molecules resembles a bowl or a chalice (the term ‘calixarene’ is derived from ‘calyx’, the Greek word for ‘chalice’). Calixarenes may be functionalised with ester groups to bind with metal ions, or they can host various molecules in their hydrophobic cavities. Calixarenes have been demonstrated to be useful in a number of applications, including molecular sensors and catalysis [6, 8].

The C_{60} fullerene molecule is an iconic molecule that has captured the imagination of scientists, and similar to DNA, it has penetrated the consciousness of the layperson due to its inherent aesthetic beauty. First ob-

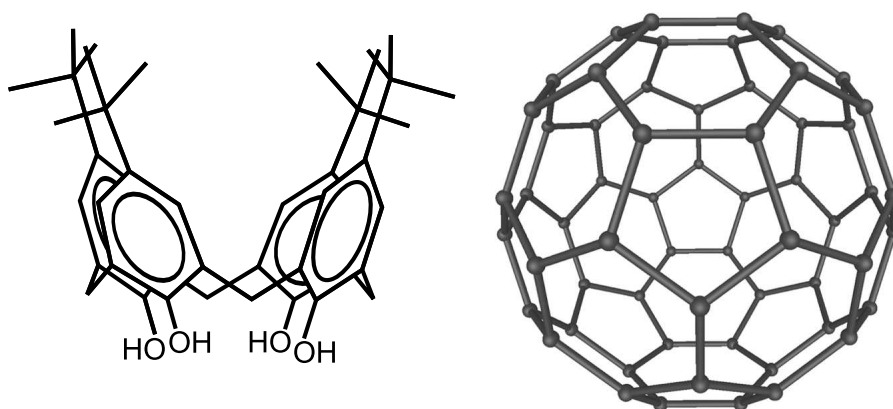


Figure 1.1: Examples of calixarene and fullerene molecules; *p*-tert-butylcalix[4]arene (left); C_{60} (right). C_{60} figure courtesy of Michael Ströck.

served in the laboratory in 1985 by Kroto and co-workers [9], C_{60} was subsequently discovered to occur in candle soot [10] (along with the larger C_{70} fullerene); it is an amazing notion that, in the seemingly mundane act of lighting a candle, one can produce a substance as wonderful as a fullerene (albeit in miniscule quantities!). Not long after the initial discovery of fullerenes, the existence of *endohedral fullerene* complexes was demonstrated. The first endohedral complexes were prepared by laser vaporisation of graphite targets doped with rare earth metals (lanthanum, yttrium) or transition metals (titanium, zirconium, hafnium) [7]. This forms fullerene

molecules with metal atoms confined within the cavity of the carbon skeleton.

Rubin and co-workers pioneered a method for inserting molecular hydrogen into fullerene cavities by opening an orifice in the fullerene cage via controlled chemical reactions, a process that was dubbed ‘molecular surgery’ [11]. In 2003 Komatsu and co-workers developed an alternative molecular surgery scheme, which achieved 100% yield of molecular hydrogen encapsulated in an open-cage fullerene [12, 13] (*cf.* 5% yield reported by Rubin *et al.* [11]). Subsequently, it was shown that by further chemical reactions the orifices created in the fullerene walls can be closed to form the supramolecular complex H₂@C₆₀ [14].

1.2 cryoMAS NMR

Potential applications have been identified for endohedral fullerenes and calixarene host-guest complexes within the nascent field of *cryoMAS NMR*, i.e. magic-angle-spinning NMR at cryogenic temperatures. The primary goal of the *cryoMAS* project, lead by Prof. M.H. Levitt of the University of Southampton, is to develop the necessary technology and techniques to study large biomolecules, such as proteins, using NMR at cryogenic temperatures. MAS NMR is a high-resolution technique that is routinely used to solve molecular structures. By performing MAS at cryogenic temperatures, the dual benefits of high-resolution and increased signal-to-noise should aid in providing answers to questions that are currently beyond the scope of conventional NMR.

There are a broad range of associated scientific and technological challenges associated with achieving this goal, one of which is the development of so-called *cryorelaxors* [15]. A downside of conducting MAS-NMR experiments at low-temperature is the increased proton spin-lattice relaxation time T_1 . The gains in signal afforded at low-temperature may be impracticable if the polarisation build-up time, i.e. T_1 , is too long. A cryorelaxor is a supramolecular complex that can be functionalised and attached to a large biomolecule so that it may deliver targeted relaxation. This may be achieved if the cryorelaxor complex comprises protons that are highly mobile at cryogenic temperatures. The motion of the protons causes surrounding protons to experience a time-dependent magnetic dipole-dipole interaction,

which drives the system towards thermal equilibrium; it is this motion that is the central theme of this thesis. More specifically, the rotational motion of weakly-hindered methyl groups in calixarene host-guest complexes, and the rotation-translation of endohedral hydrogen in an open-cage fullerene, has been investigated.

1.3 Quantum molecular motion

In molecular crystals, the constituent molecules and moieties experience electrostatic interactions with surrounding atoms, which give rise to potential barriers that hinder motional processes such as rotation and translation [16]. At low temperatures it is often the case that the molecules do not have enough kinetic energy to overcome these barriers. However, in particular systems, it is possible for motion to persist even at the lowest of temperatures, due to either the molecule being very weakly hindered, or the ability of the molecule to penetrate the barrier via quantum tunnelling. Protons in hydrogen-bonds and methyl-groups are two such examples of systems that exhibit quantum-tunnelling in the solid-state, and both have been studied extensively in the Quantum Molecular Dynamics laboratory of Prof. A.J. Horsewill at the University of Nottingham [17, 18].

1.3.1 Methyl-group rotation

The rotation of methyl-groups in molecular crystals is a fascinating, much-studied phenomenon. It is a model system for studying the complementarity between quantum and classical mechanics, and the transition between these two regimes.

The rotational motion of methyl-groups in molecular crystals was first inferred from anomalies in the measurements of bulk macroscopic properties such as heat capacity and the dielectric constant [19, 20]. The first studies of methyl group rotation in solids using NMR centred on observing changes in the shape of the proton NMR absorption peak, as a function of temperature. One of the primary causes of linewidth broadening is the interaction of nuclear spins with a local magnetic field, which has its origins in dipole-dipole interactions with surrounding magnetic nuclei. Molecular motion can average out the local magnetic fields to zero, thus causing the linewidth to narrow significantly. This effect is known as motional narrowing, and was

first described by Bloembergen, Purcell and Pound in their seminal paper “*Relaxation effects in NMR absorption*” [21].

Building on work by Van Vleck, who theoretically determined the dipolar broadening of the absorption linewidth in a rigid lattice [22], Gutowsky and Pake developed expressions for NMR lineshapes that took molecular reorientation into account [19]. This enabled them to estimate the nature of the motional processes and frequency of motion, from measurements of the second moment of the absorption peak. Following this, a series of papers by Gutowsky and co-workers was published [23, 24, 25, 26, 27], which reported results of measurements of the second moment as a function of temperature in a range of molecules containing methyl groups. The latter papers of this series went on to explore several models for the reorientational motion of the hindered methyl groups, and compared these to the experimental data. In the third paper of the series [25] a quantum mechanical tunnelling process was considered, along with a classical over-barrier hopping process. Both models could be made to give satisfactory accounts of the data by appropriately setting the values of certain parameters (i.e. activation energy, frequency factor), although the tunnelling model yielded estimates of these parameters that were physically more reasonable, despite the many approximations made. The final paper in this series [27] describes how measuring the proton spin-lattice relaxation time can give more quantitative information about the reorientational processes, compared to NMR linewidth measurements. The experimental data was found to agree well with the model developed by Stejskal and Gutowsky [26] that related the tunnelling frequency to proton T_1 .

A more complete model of methyl-group tunnelling, in which the spin and rotational degrees of freedom are coupled to lattice phonons, was developed further by Haupt [28]. The emergence of high resolution neutron scattering spectrometers in the latter half of the 1970s allowed direct measurement of tunnelling spectra via inelastic neutron scattering (INS) [29], and the Haupt model was verified by Müller-Warmuth and co-workers by comparing INS and NMR measurements [30]. Ever since, NMR investigations of methyl-group rotation have been complemented by INS measurements, and *vice versa*. Prager and Heidemann [31] have compiled an extensive bibliography of papers relating to methyl-group rotation in materials studied by INS, which also includes details of complementary NMR measurements.

1.3.2 Dynamics of confined H₂

The dynamics of molecular hydrogen confined in porous media has been the subject of many experimental and theoretical investigations because of its importance in the context of hydrogen storage, currently an area of high scientific and technological interest, due to the potential environmental and economic benefits of finding a clean and viable replacement for fossil-fuel powered vehicles [32].

In 1997 A.C. Dillon and co-workers identified single-walled carbon nanotubes (SWNTs) potentially as a promising hydrogen storage medium, by demonstrating their capability to adsorb molecular hydrogen [33]. INS measurements of similar samples, conducted by Georgiev et. al [34, 35] revealed that there are numerous adsorption sites amongst the nanotubes, the most preferential being the grooves between neighbouring nanotubes, on the outer surface of a nanotube ‘rope’.

Motivated by INS measurements of molecular hydrogen confined in the interstitial sites of C₆₀ (*intercalated* H₂, denoted H₂ : C₆₀) [36], Yildirim and Harris [37] used a variety of theoretical approaches to determine the rotational and translational energy levels of the confined hydrogen, and to develop expressions for the neutron scattering functions for transitions between the levels. Confinement of the H₂ molecule causes quantisation of the translational degrees of freedom, and the large rotational constant of H₂ results in rotational quantisation. The symmetry of the confinement cavity is reflected in the quantum dynamics of the molecule. These effects are also revealed in NMR studies of H₂ : C₆₀, as reported by Tomaselli [38, 39], and in endohedral hydrogen-fullerene complexes (Carravetta, Levitt and co-workers [40, 15]). The latter are much more stable than intercalated samples, which leach hydrogen at room temperature. Therefore endohedral hydrogen-fullerene complexes provide robust, practical systems for the investigation of quantum molecular dynamics.

1.4 Spin-symmetry species

Methyl-groups and molecular hydrogen are both examples of *spin-symmetry species*. The Pauli exclusion principle imposes particular symmetry restrictions on the wavefunctions of many-particle systems that contain fermions, which can cause spatial and spin degrees of freedom to become intercon-

nected.

More exactly, the Pauli exclusion principle states that the wavefunction of a many-particle system must be anti-symmetric upon the exchange of identical fermions [41]. The total wavefunctions of methyl-groups and confined hydrogen molecules are products of wavefunctions for a number of degrees of freedom, including vibrational, electronic, rotational, translational (H_2 only), and nuclear-spin degrees of freedom. These individual wavefunctions will have a particular symmetry for a given quantum state. Certain combinations of wavefunction symmetry are forbidden as a consequence of the Pauli exclusion principle.

Molecular hydrogen can exist as two species, namely *parahydrogen* and *orthohydrogen*. They are distinguished by the relative alignment of the proton spins with each other. The nuclear spin wavefunctions of parahydrogen and orthohydrogen are, respectively, anti-symmetric and symmetric upon the exchange of protons. This has implications for the rotational degrees of freedom, and is discussed in more detail in section 2.5.

Similarly, the protons of a methyl-group can be treated as a single particle, of either spin $1/2$ or $3/2$ (referred to as the *E* and *A* species, respectively). *E* species have anti-symmetric nuclear spin wavefunctions, and *A* species have symmetric nuclear spin wavefunctions. The resulting restrictions on the spatial degrees of freedom are discussed in section 2.3.3.

1.5 Thesis layout

This thesis is organised as follows; the fundamental concepts of NMR and INS, relevant to the work undertaken, are reviewed in chapter 2; the theoretical framework of methyl-group rotation, and the quantum dynamics of confined hydrogen is also introduced. Details of the field-cycling NMR, and INS experiments are discussed in chapter 3. Results from the investigation of methyl-group dynamics in a variety of calixarene host-guest molecules are presented in chapter 4. Results from INS measurements of the quantum rotation and translation of endohedral hydrogen in an open-cage fullerene are presented in chapter 5.

Chapter 2

Theory

In this chapter some fundamental concepts of nuclear magnetic resonance (NMR) and inelastic neutron scattering (INS) relevant to this thesis will be reviewed. The existing theoretical framework of spin-lattice relaxation via rotational tunnelling of methyl groups (the so-called Haupt model) will be discussed, as will the motivation behind using field-cycling NMR relaxometry as a technique to study rotational dynamics of methyl groups. The quantum motion of confined hydrogen is introduced in section 2.5.

2.1 NMR fundamentals

Nuclear magnetic resonance is a well-known phenomenon, and since the magnetic resonance of protons in solid paraffin was observed by Purcell, Torrey and Pound in 1946 [42], many NMR experimental techniques have become established. Today NMR is routinely exploited across a number of scientific disciplines in sophisticated spectroscopic and imaging techniques, in order to probe all states of conventional matter. Nuclear magnetic resonance imaging, more commonly referred to as MRI, is perhaps the most widely known application of the NMR phenomenon.

In NMR experiments the magnetic moments of nuclei are subjected to a large static magnetic field. The magnetic moments, or *spins*, are manipulated using weak radio-frequency electromagnetic (EM) radiation, and a wealth of information may be drawn from the response of the spins to the applied magnetic fields.

2.1.1 Nuclear spin

Many nuclei possess an intrinsic spin angular momentum. Rather than being due to an actual physical rotation, spin angular momentum is an inherent property of the nucleus, just as mass and charge are. Spin angular momentum is quantised, and since it is a vector quantity, there are two quantum numbers associated with it; these are the nuclear spin quantum number I , and the azimuthal quantum number m_I . I determines the magnitude of the spin angular momentum vector \mathbf{S} by

$$|\mathbf{S}| = \hbar\sqrt{I(I+1)}, \quad (2.1)$$

and may have integer or half-integer values. The azimuthal quantum number m_I defines the allowed orientations of the spin angular momentum, relative to a reference axis, conventionally defined as the z -axis. m_I may take on any of the $(2I+1)$ values allowed by the following expression;

$$m_I = -I, (-I+1) \dots I. \quad (2.2)$$

m_I is also referred to as the projection quantum number, as it describes the projection of the spin angular momentum along the z -axis thus

$$S_z = \hbar m_I. \quad (2.3)$$

2.1.2 Zeeman effect

The Zeeman effect is the fundamental interaction that makes NMR possible. When a nucleus with non-zero spin is exposed to a static magnetic field \mathbf{B}_0 , the interaction between the field and the nuclear magnetic moment $\boldsymbol{\mu}$, causes the degeneracy of the spin angular momentum states to be lifted. $\boldsymbol{\mu}$ is proportional to the spin angular momentum,

$$\boldsymbol{\mu} = \gamma \mathbf{S}. \quad (2.4)$$

The constant of proportionality γ is known as the magnetogyric ratio. The energy of a magnetic moment in the presence of a magnetic field is given by the classical expression

$$E = -\boldsymbol{\mu} \cdot \mathbf{B}_0. \quad (2.5)$$

If the \mathbf{B}_0 field is considered to be aligned with the z -axis, using (2.3) and (2.4), equation (2.5) can be rewritten as

$$E = -\gamma\hbar m_I B_z . \quad (2.6)$$

For a spin I nucleus, the $(2I + 1)$ spin states become separated by an energy

$$\Delta E = \hbar\gamma B_z . \quad (2.7)$$

This splitting of the energy of the spin states caused by exposure to a magnetic field is known as *Zeeman splitting*. Figure 2.1 illustrates the case for a nucleus with spin $I = 1/2$ (e.g. ^1H , ^{13}C , ^{15}N)*. The $m_I = +1/2$ state is referred to as the $|\alpha\rangle$ eigenstate, and $m_I = -1/2$ is the $|\beta\rangle$ eigenstate.

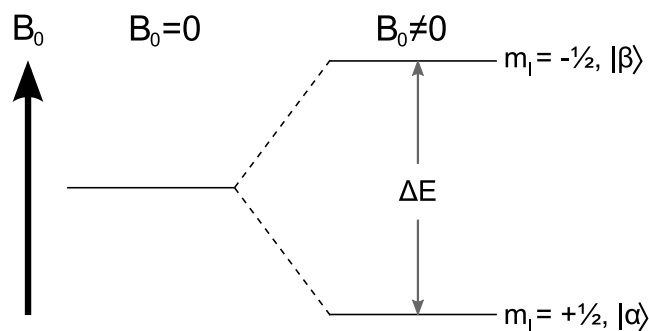


Figure 2.1: Zeeman splitting for spin 1/2 nucleus.

For magnetic field strengths typically available in the laboratory, and for typical values of γ , ΔE in frequency units corresponds to short-wave radio frequencies (RF) of electromagnetic radiation. NMR can be observed by driving transitions between the energy levels with resonant electromagnetic radiation. Consequently, NMR is impossible for nuclei with spin $I = 0$; such nuclei are referred to as being ‘NMR-silent’, and unfortunately includes the naturally ubiquitous ^{12}C isotope.

*As this thesis primarily deals with proton NMR, all subsequent examples are restricted to the $I = 1/2$ case, unless otherwise stated.

2.1.3 Larmor precession

A complete description of NMR phenomena and the behaviour and dynamics of nuclear spins is only possible by applying quantum mechanical theory. However it is expedient to employ a classical description of NMR, as many aspects of NMR experiments can be understood in terms of a classical vector model.

If we consider the nuclear spin to be an isolated magnetic moment $\boldsymbol{\mu}$ in the presence of a magnetic field \mathbf{B}_0 , the magnetic moment will experience a torque

$$\frac{d\mathbf{S}}{dt} = \boldsymbol{\mu} \wedge \mathbf{B}_0 . \quad (2.8)$$

By substituting in equation (2.4), this may be rewritten

$$\frac{d\boldsymbol{\mu}}{dt} = \gamma \boldsymbol{\mu} \wedge \mathbf{B}_0 . \quad (2.9)$$

If the magnetic field is aligned along the z -axis, we may write

$$\begin{aligned} \frac{d\mu_x}{dt} &= \gamma \mu_y B_z \\ \frac{d\mu_y}{dt} &= -\gamma \mu_x B_z \\ \frac{d\mu_z}{dt} &= 0 , \end{aligned} \quad (2.10)$$

where $\mu_{x,y,z}$ are the Cartesian components of the magnetic moment. The general solution to these equations is as follows;

$$\begin{aligned} \mu_x(t) &= \mu_x(0)\cos(\gamma B_z t) + \mu_y(0)\sin(\gamma B_z t) \\ \mu_y(t) &= -\mu_x(0)\sin(\gamma B_z t) + \mu_y(0)\cos(\gamma B_z t) \\ \mu_z(t) &= \mu_z(0) . \end{aligned} \quad (2.11)$$

These equations describe a precession of $\boldsymbol{\mu}$ about the z -axis in the xy -plane. The longitudinal component μ_z of the magnetic moment vector remains constant, and the tip sweeps out a circular path in the plane transverse to the applied field. The rate of precession is given by

$$\omega_L = \gamma B_z, \quad (2.12)$$

and ω_L is known as the *Larmor frequency*. Re-examination of equation (2.7)

reveals that $\hbar\omega_L$ is exactly equal to the Zeeman splitting of the spin states. ω_L is the rate of precession of spins about the applied magnetic field, and also the frequency of RF electromagnetic radiation required to induce transitions between spin states.

2.1.4 Interaction between a magnetic moment and a RF field

The manipulation of nuclear spins by applying RF electromagnetic radiation is a central feature of NMR experiments. Staying with the classical vector model introduced above, the affect of a RF electromagnetic field on a magnetic dipole, applied perpendicularly to the static B_0 field, is discussed here.

Consider a magnetic moment $\boldsymbol{\mu}$ in the presence of a static magnetic field \mathbf{B}_0 and a time-dependent RF magnetic field, $\mathbf{B}_1(t)$ (the electric field of the EM radiation may be safely neglected as it does not interact with the magnetic moment). If $\mathbf{B}_1(t)$ is linearly polarised along the x -axis it can be expressed

$$\mathbf{B}_1(t) = 2B_1 \cos(\omega t)\mathbf{i} . \quad (2.13)$$

This can be decomposed into two circular components, rotating at angular frequency ω in opposite senses in the xy -plane,

$$\begin{aligned} \mathbf{B}_{\text{res}}(t) &= B_1(\cos(\omega t)\mathbf{i} + \sin(\omega t)\mathbf{j}) \\ \mathbf{B}_{\text{non res}}(t) &= B_1(\cos(\omega t)\mathbf{i} - \sin(\omega t)\mathbf{j}) . \end{aligned} \quad (2.14)$$

$\mathbf{B}_{\text{non res}}(t)$ rotates in the opposite sense to ω_L . Under normal circumstances this component has a comparatively small effect on the motion of the spins, and may therefore be neglected. The equation of motion for the spin under the influence of the \mathbf{B}_0 and $\mathbf{B}_1(t)$ fields may be written

$$\frac{d\boldsymbol{\mu}}{dt} = \gamma\boldsymbol{\mu} \wedge (\mathbf{B}_0 + \mathbf{B}_{\text{res}}(t)) , \quad (2.15)$$

provided the RF frequency ω is equal to ω_L . Application of a perpendicular RF field at resonant frequency has the effect of introducing an additional torque, which has an axis of rotation orthogonal to the \mathbf{B}_0 field (figure 2.2). The torque acts to increase the angle subtended by $\boldsymbol{\mu}$ with \mathbf{B}_0 . This introduces an additional precession that superimposes itself on the Larmor precession, referred to as *nutation*.

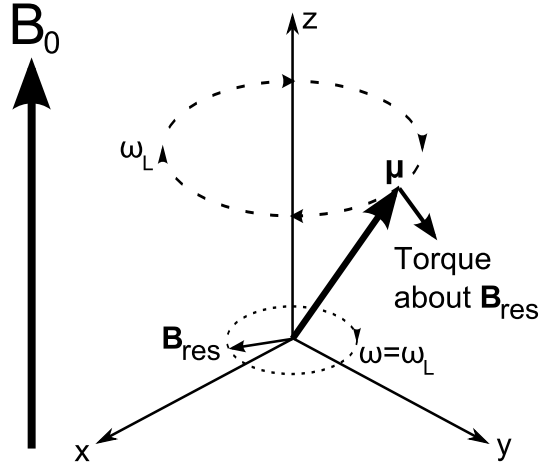


Figure 2.2: The interaction between a magnetic moment and a resonant RF magnetic field introduces a torque about \mathbf{B}_{res} , which causes the magnetic moment to nutate away from the z axis, defined by the direction of the static field B_0 .

The response of $\boldsymbol{\mu}$ to a RF field with frequency $\omega \neq \omega_L$ is simpler to handle by examining the problem in a frame of reference that rotates about the direction of the applied field (z -axis), with angular frequency ω with respect to the laboratory frame. A consequence of switching to the rotating frame of reference is that the applied \mathbf{B}_1 field becomes time independent. The equation of motion for $\boldsymbol{\mu}$ in the rotating frame of reference (denoted by primed co-ordinates) is expressed as

$$\left(\frac{d\boldsymbol{\mu}}{dt}\right)_{x',y',z} = \gamma\boldsymbol{\mu} \wedge \mathbf{B}_{\text{eff}}. \quad (2.16)$$

\mathbf{B}_{eff} is an effective field, which has the form

$$\mathbf{B}_{\text{eff}} = B_1\mathbf{i}' + B_0\left(1 - \frac{\omega}{\omega_L}\right)\mathbf{k}. \quad (2.17)$$

When the frequency of the applied RF field is “off-resonance” (i.e. $\omega \neq \omega_L$), $\boldsymbol{\mu}$ precesses about an axis of rotation that has components in the x' and z directions. However if the RF radiation is “on-resonance” ($\omega = \omega_L$), the component in the z direction disappears, and $\boldsymbol{\mu}$ nutates about the x' -axis

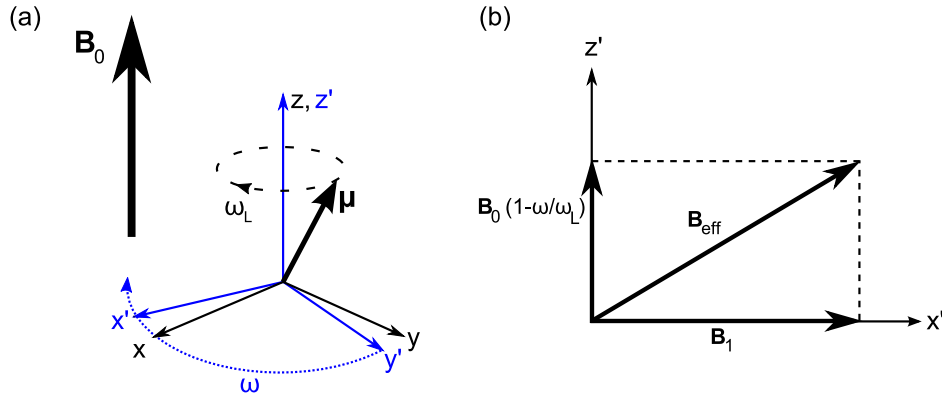


Figure 2.3: (a) In the frame of reference rotating about the z -axis at frequency ω_L , resonant RF radiation causes the magnetic moment to nutate about the x' -axis; (b) For RF radiation that is off-resonance, the magnetic moment nutates about the effective field B_{eff} .

with angular frequency

$$\omega_{\text{nut}} = \gamma B_1 . \quad (2.18)$$

2.1.5 Bulk magnetisation

The classical treatment of a dipole moment interacting with external magnetic fields, as outlined in sections 2.1.3 and 2.1.4, garners some results that are equivalent to those found from a quantum mechanical treatment of a single nuclear spin. However due to the quantum nature of a nuclear spin, a classical model for the dynamics of a spin has its limitations.

Another point to consider is that in practice, NMR experiments measure the response of an *ensemble* of interacting nuclear spins; a full quantum mechanical treatment of such a system is not a straightforward task.

The classical vector model comes in use again as it may be applied to the *bulk magnetisation* \mathbf{M} of a sample. The bulk magnetisation originates due to *nuclear paramagnetism*, and it is the macroscopic property of the sample that is observed by NMR experiments. \mathbf{M} can be considered to be representative of the average behaviour of the individual nuclear spins. The equations of motion for a single magnetic moment $\boldsymbol{\mu}$, introduced in the aforementioned sections, are applicable to \mathbf{M} .

The bulk magnetisation at thermal equilibrium \mathbf{M}_0 aligns itself with the B_0 field. The thermal equilibrium configuration is stable on a macroscopic

scale, whereas the microscopic configuration of the individual spins is far from static. Overall, the net contribution of each spin to the transverse components of M_0 average out to zero. However there is a slight anisotropy in the orientations of the spins, which gives rise to a net magnetisation, aligned with \mathbf{B}_0 . M_0 is proportional to the population difference between the spin states n , which is governed by Boltzmann statistics;

$$n = N_\alpha - N_\beta \quad (2.19)$$

$$\frac{N_\alpha}{N_\beta} = \exp\left(\frac{-\Delta E}{k_B T}\right). \quad (2.20)$$

N_i is the population of the $|i\rangle$ state, and ΔE is the Zeeman splitting (all other symbols have their usual meaning). In the high temperature approximation (i.e. at temperatures greater than a few mK) the Boltzmann exponential can be approximated as

$$\exp\left(\frac{-\Delta E}{k_B T}\right) \approx 1 - \frac{\hbar\gamma B_z}{k_B T}. \quad (2.21)$$

M_0 is the net magnetisation from the vector sum of the magnetic moments of the individual spins at thermal equilibrium, therefore the magnitude of M_0 may be calculated from

$$|M_0| = N_\alpha \mu_z^{(\alpha)} + N_\beta \mu_z^{(\beta)}. \quad (2.22)$$

Since $\mu_z^{(\alpha)} = -\mu_z^{(\beta)} = 1/2\hbar\gamma$, this may be written

$$|M_0| = \frac{n}{2} \hbar\gamma. \quad (2.23)$$

After some routine algebra, the Curie law for nuclear magnetism is obtained;

$$|M_0| = \frac{1}{4} N (\hbar\gamma)^2 \frac{B_z}{k_B T}, \quad (2.24)$$

where $N = N_\alpha + N_\beta$. The magnetisation is proportional to magnetic field strength, and inversely proportional to temperature.

Nuclear paramagnetism is many orders of magnitude smaller than the diamagnetism of typical samples. Therefore in order to measure the nuclear paramagnetism, it is necessary to manipulate \mathbf{M} so that it is oriented perpendicular to the applied static field. This is achieved by applying a pulse

of RF EM radiation with frequency ω_L .

Whilst the resonant RF pulse is applied, \mathbf{M} experiences a torque and nutates away from its alignment with the z -axis. The nutation is about an axis perpendicular to the z -axis; the desired axis of rotation can be set by appropriate selection of the phase of the RF pulse (by convention, phase $\phi = 0$ corresponds to the x' -axis). The angle subtended by \mathbf{M} and \mathbf{B}_0 as a result of the RF pulse is known as the *tipping angle*. The tipping angle is proportional to the duration of the pulse t_w (“pulse-width”) and the magnitude of \mathbf{B}_1 (“pulse amplitude”), i.e.

$$\begin{aligned}\theta_{\text{tip}} &= \gamma\omega_{\text{nut}} \\ &= \gamma B_1 t_w .\end{aligned}\tag{2.25}$$

Therefore \mathbf{M} can be diverted away from the z -axis into the transverse plane by application of a 90° pulse (or $\pi/2$ pulse), so that it may be detected and measured.

2.1.6 Bloch equations

Following a quick change in temperature, \mathbf{B}_0 and/or the application of a RF pulse, the magnetisation of a sample will be in a non-equilibrium state. The system may not persist in this state, and must return to the state of thermal equilibrium, $\mathbf{M} = (0, 0, M_0)$.

The process by which the magnetisation \mathbf{M} returns to the thermal equilibrium value is known as *relaxation*. Felix Bloch devised the following coupled equations, which phenomenologically describe the time-evolution of the components of \mathbf{M} in a static field $\mathbf{B}_0 = (0, 0, B_z)$, under the effects of relaxation [43];

$$\begin{aligned}\frac{dM_x}{dt} &= \gamma M_y B_z - \frac{M_x}{T_2} \\ \frac{dM_y}{dt} &= -\gamma M_x B_z - \frac{M_y}{T_2} \\ \frac{dM_z}{dt} &= 0 - \frac{M_z - M_0}{T_1} .\end{aligned}\tag{2.26}$$

T_1 and T_2 are time constants that each characterise a different exponential relaxation process. T_2 characterises the decay of the components of the magnetisation that are perpendicular to the applied field; this is referred

to as *spin-spin relaxation*, or *transverse relaxation*. Spin-spin relaxation is caused by spins interacting with each other, which results in a dephasing of the spin precession and therefore a decay in the transverse magnetisation.

T_1 characterises the recovery of \mathbf{M} in the z -direction; this is referred to as *spin-lattice relaxation*, or *longitudinal relaxation*. As the name suggests, spin-lattice relaxation is caused by spins interacting with the various degrees of freedom of the surrounding *lattice*; energy exchange between the spin system and lattice is necessary to drive the spins toward equilibrium. Spin-lattice relaxation is discussed in detail in section 2.2, as measurement of T_1 may reveal information about molecular motion.

2.1.7 Free induction decay

The bulk magnetisation \mathbf{M} is measured by manipulating the orientation of \mathbf{M} away from complete alignment with the static \mathbf{B}_0 field. In sections 2.1.4 and 2.1.5 it was shown that this may be achieved by applying pulses of RF radiation perpendicular to \mathbf{B}_0 . The Bloch equations predict that the transverse components of \mathbf{M} (i.e. M_x and M_y) rotate about the z -axis at the Larmor frequency, whilst simultaneously decaying exponentially with time constant T_2 . According to Maxwell's equations the time-varying magnetic field has an associated time-varying electric field. The oscillating electric field gives rise to a oscillating current in a wire coil surrounding the sample. This induced current is the NMR signal $S(t)$ and is referred to as the *free induction decay* (FID). The FID has two components which can be expressed by;

$$\begin{aligned} S_x(t) &= S_0 \sin(\omega_L t) \exp\left(\frac{-t}{T_2}\right) \\ S_y(t) &= S_0 \cos(\omega_L t) \exp\left(\frac{-t}{T_2}\right) \\ S(t) &= S_x(t) + iS_y(t) \\ &= S_0 \exp[(i\omega_L - \lambda)t], \end{aligned} \tag{2.27}$$

where S_0 is the maximum amplitude of the NMR signal ($S_0 \propto M_0$) and the damping factor λ is the inverse of T_2 . $S_x(t)$ and $S_y(t)$ are referred to as the real and imaginary parts of the complex signal $S(t)$. $S_y(t)$ is measured 90° out of phase with $S_x(t)$. This technique is known as *quadrature detection*,

and is necessary if the sign of ω_L is to be preserved after detection.

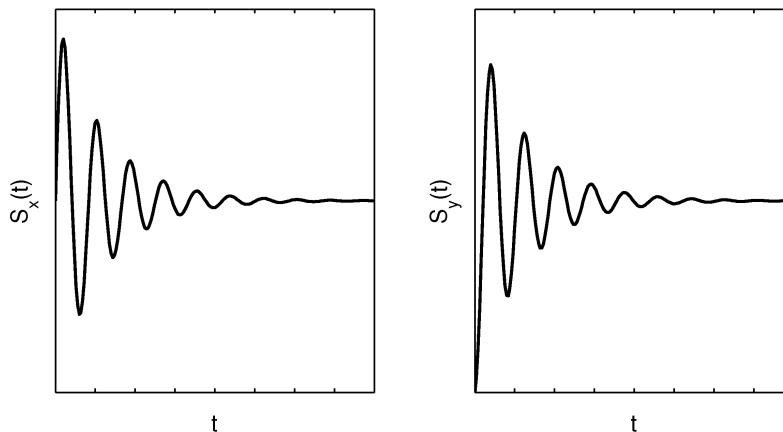


Figure 2.4: The real and imaginary parts of an off-resonance free induction decay signal. For quadrature detection the FID is sampled by two receivers separated by 90° of phase.

The simple example shown in figure 2.4 demonstrates a FID for one Larmor frequency only. In practice a FID may have many NMR frequencies encoded within it. Figure 2.5 illustrates how the constituent frequencies of a FID may be found by performing a *Fourier transform* of the NMR signal. Upon first inspection, the signals in figure 2.5(a) and 2.5(b) appear noisy. In fact, they are a superposition of three oscillating signals $S_j(t)$ of the form given by equation (2.27), each with distinct frequencies $\omega_L^{(j)}$;

$$\begin{aligned} S^{\text{FID}}(t) &= \sum_j^3 S_j(t) \\ &= \sum_j^3 S_0^{(j)} \exp[(i\omega_L^{(j)} - \lambda^{(j)})t]. \end{aligned} \quad (2.28)$$

Performing a Fourier transform causes a time-varying signal to be transformed into the frequency domain. Figure 2.5(c) shows the real part of the Fourier transform of $S^{\text{FID}}(t)$, also known as the *absorptive* part (the imaginary component is referred to as the *dispersive* part). The peaks have the form of Lorentzian lineshapes, and are centred about the frequencies encoded in $S^{\text{FID}}(t)$. The heights of the peaks are proportional to the amplitudes of each Fourier component and the widths of the peaks are inversely

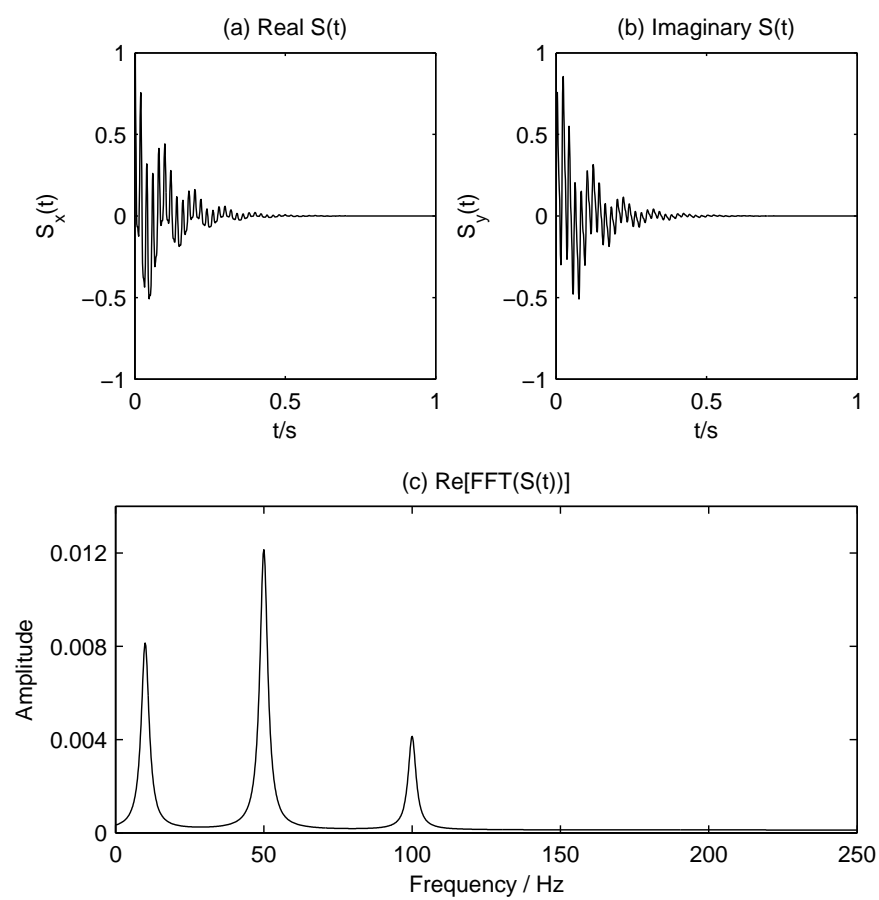


Figure 2.5: FID and corresponding absorptive spectrum for a simulated signal comprising three distinct frequencies.

proportional to the time constant of the signal decay envelope, T_2 .

2.2 Spin-lattice relaxation

Relaxation of longitudinal magnetisation M_z towards equilibrium magnetisation M_0 in an NMR sample occurs due to the existence of mechanisms for the exchange of energy between the nuclear spin system and thermal energy sinks or reservoirs. Examples of such thermal energy reservoirs include the motional modes of the molecule, i.e. translation, vibration and rotation. The reservoirs are collectively referred to as the *lattice*, hence relaxation due to interaction with the lattice is referred to as *spin-lattice relaxation*. Without the lattice, transitions from higher Zeeman energy levels (eigenstate $|\beta\rangle$) to lower ones (eigenstate $|\alpha\rangle$) would not be possible, as the spontaneous emission transition rate is negligible. Attainment of thermal equilibrium following, for example, a 90° RF pulse or a decrease in temperature is achieved through stimulated emission via interactions with the lattice. The model for spin-lattice relaxation described in this section was developed by Bloembergen, Purcell and Pound, and presented in a seminal paper in 1948 [21]. It is often referred to as the ‘BPP formalism’.

The main source of relaxation in non-quadrupolar, non-metallic, diamagnetic NMR systems is the nuclear dipole-dipole interaction [44]. However, before discussing relaxation due to the dipole-dipole interaction it will be useful to examine a simple two-level system, in order to introduce the relationship between transition probabilities and the spin-lattice relaxation time.

2.2.1 Two-level system

Consider a system of non-interacting spin 1/2 nuclei, in the presence of a static \mathbf{B}_0 field. If the relative population of each energy level is denoted by $n_{\alpha/\beta}$ the population difference n and total number of spins N are given by

$$\begin{aligned} n &= n_\beta - n_\alpha \\ N &= n_\alpha + n_\beta . \end{aligned} \tag{2.29}$$

We can define two transition rates, W_\downarrow and W_\uparrow , which are probabilities per unit time for transitions to occur between energy levels. W_\downarrow is a downward

transition ($|\beta\rangle \rightarrow |\alpha\rangle$), and W_{\uparrow} is an upward transition ($|\alpha\rangle \rightarrow |\beta\rangle$). The exact nature of the mechanism for energy exchange between the lattice and spin system is not specified; it is supposed that such a mechanism exists. The mechanism may be a time-varying magnetic field, or a randomly fluctuating molecular interaction.

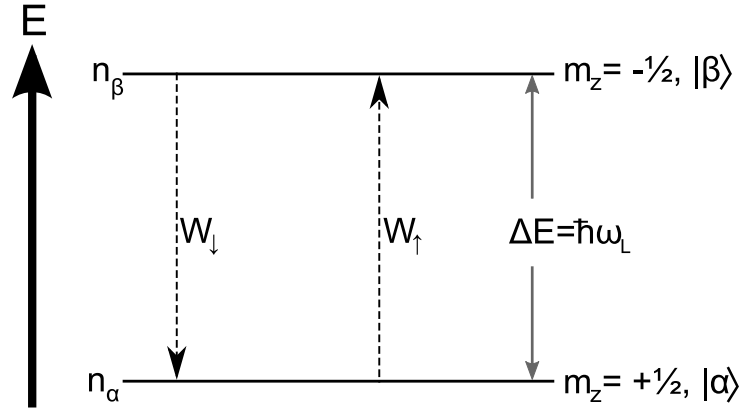


Figure 2.6: Zeeman splitting of spin states for spin 1/2 nucleus. Transition probabilities per unit time are denoted by $W_{\uparrow/\downarrow}$.

The rate of change of the population difference can be expressed in terms of the transition probabilities

$$\frac{dn}{dt} = 2W_{\downarrow}n_{\beta} - 2W_{\uparrow}n_{\alpha} . \quad (2.30)$$

Equations (2.29) can be rearranged to give

$$n_{\alpha} = \frac{1}{2}(N + n) \quad (2.31)$$

$$n_{\beta} = \frac{1}{2}(N - n) . \quad (2.32)$$

Substituting these into (2.30) gives

$$\frac{dn}{dt} = N(W_{\downarrow} - W_{\uparrow}) - n(W_{\downarrow} + W_{\uparrow}) . \quad (2.33)$$

Let $W = \frac{1}{2}(W_{\downarrow} + W_{\uparrow})$ so that we may write

$$\frac{dn}{dt} = 2W(n_0 - n) , \quad (2.34)$$

where $n_0 = N \frac{W_{\downarrow} - W_{\uparrow}}{W_{\downarrow} + W_{\uparrow}}$. A solution to this equation is

$$n(t) = n_0(1 - \exp(-2Wt)) . \quad (2.35)$$

The longitudinal magnetisation M_z is proportional to the population difference n , therefore it holds that

$$M_z(t) = M_0(1 - \exp(-2Wt)) . \quad (2.36)$$

This equation describes exponential growth of M_z towards equilibrium magnetisation M_0 . It is also a solution to the longitudinal component of the Bloch equation if we identify the transition probability with the relaxation rate thus

$$T_1 = \frac{1}{2W} . \quad (2.37)$$

The spin-lattice relaxation time is inversely proportional to the transition probability W , which can be determined using Fermi's Golden Rule, if the interaction that causes the transition is small compared to the Zeeman interaction.

2.2.2 Correlation functions and spectral density functions

The transitions of spins between energy levels would not be possible without a process to drive the transitions. In matter, the random Brownian motion of molecules causes random fluctuations of internuclear distances and angles, which results in a random fluctuation of the internuclear interactions.

The nature of the stochastic fluctuations of some time-varying quantity $p(t)$ can be characterised by a *correlation function*. The correlation function $\mathbb{G}(\tau)$ of a function $p(t)$ is defined as

$$\mathbb{G}(\tau) = \langle p(t)p^*(t + \tau) \rangle_{Av} . \quad (2.38)$$

$\mathbb{G}(\tau)$ is a measure of how well $p(t)$ is correlated with itself, after some time τ . For example, if $p(t)$ represents the position of a particle undergoing a random walk, the product $p(t) \cdot p(t + \tau)$ would be large for small τ ("good correlation"), and would get progressively smaller for larger values of τ ("poor correlation").

In spin-lattice relaxation, it is the stochastic fluctuation of the magnetic

dipole-dipole interaction that drives relaxation. If we express the Hamiltonian for this interaction as $\hat{\mathbf{H}}_{\text{DD}}$, the correlation function of the dipole-dipole interaction can be expressed as

$$\mathbb{G}(\tau) = \overline{\langle r | \hat{\mathbf{H}}_{\text{DD}}(t + \tau) | s \rangle \langle s | \hat{\mathbf{H}}_{\text{DD}}(t) | r \rangle} , \quad (2.39)$$

where $|r\rangle$ and $|s\rangle$ are the spin states of the system, and the over-bar denotes an ensemble average. It is assumed that $\mathbb{G}(\tau)$ is independent of t and is an even function. It is also assumed that the correlation function follows a single-exponential form

$$\mathbb{G}(\tau) \propto e^{-|\tau|/\tau_c} , \quad (2.40)$$

where τ_c is known as the *correlation time*. τ_c characterises the random fluctuations measured by $\mathbb{G}(\tau)$.

The *spectral density function* $\mathbb{J}(\omega)$ is defined as the Fourier transform of the correlation function

$$\mathbb{J}(\omega) = \int_0^\infty d\tau \mathbb{G}(\tau) e^{-i\omega\tau} . \quad (2.41)$$

It is a measure of the frequency dependence of the randomly fluctuating interaction described by $\mathbb{G}(\tau)$. If $\mathbb{G}(\tau)$ has the form as stated in equation (2.40) then

$$\mathbb{J}(\omega) \propto \frac{\tau_c}{1 + \omega^2 \tau_c^2} . \quad (2.42)$$

The general line-shape of a spectral density function is a Lorentzian function with half-width τ_c^{-1} . Examples of typical forms of autocorrelation functions and their corresponding spectral densities can be seen in figure 2.7. It should be noted that although only positive frequencies are displayed, spectral density functions are symmetric about the zero frequency axis.

2.2.3 Two-spin system

In this section a system of two interacting spins will be introduced, in which relaxation is driven by the fluctuation of the dipole-dipole interaction. The relationship between the spectral density functions and transition probabilities will also be established.

The Hamiltonian for the magnetic dipole-dipole interaction between two

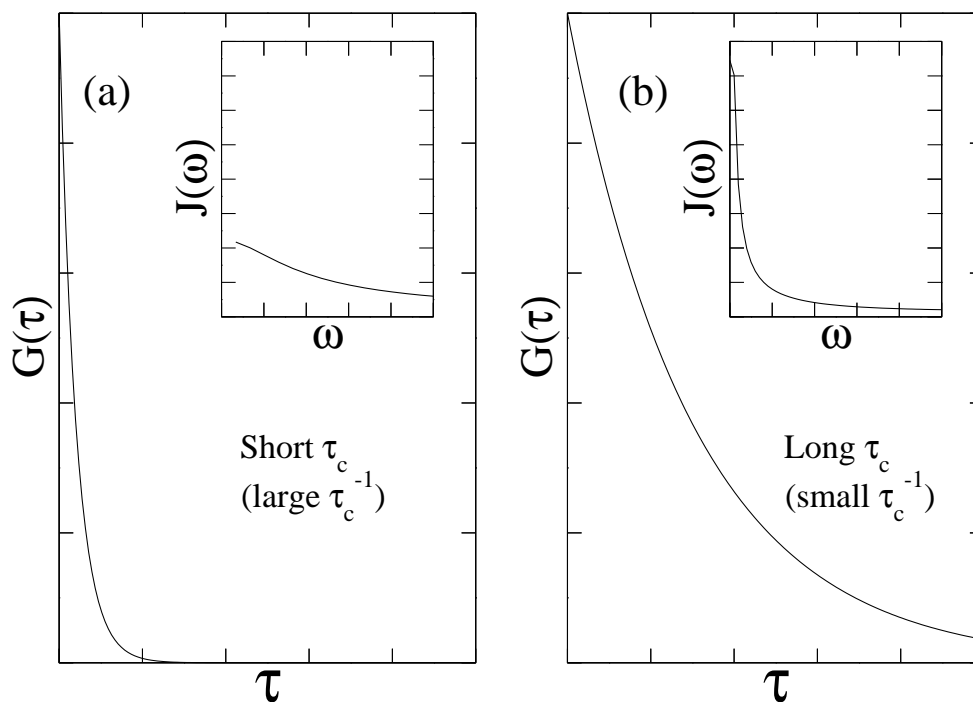


Figure 2.7: Comparison of autocorrelation functions and their respective spectral density functions (shown in insets). Graphs in figures (a) and (b) are plotted on identical scales. (a) Quickly fluctuating interactions (short τ_c ; narrow autocorrelation function; broad spectral density function); (b) Slowly fluctuating interactions (long τ_c ; broad autocorrelation function; narrow spectral density function).

spins can be written

$$\begin{aligned}\hat{\mathbf{H}}_{\text{DD}} &= \frac{\gamma_I \gamma_S \hbar \mu_0}{4\pi} r^{-3} (A + B + C + D + E + F) \\ A &= \hat{I}_z \hat{S}_z (3 \cos^2 \theta - 1) \\ B &= -\frac{1}{4} [\hat{I}_+ \hat{S}_- + \hat{I}_- \hat{S}_+] (3 \cos^2 \theta - 1) \\ C &= \frac{3}{2} [\hat{I}_z \hat{S}_+ + \hat{I}_+ \hat{S}_z] \sin \theta \cos \theta \exp(-i\phi) \\ D &= \frac{3}{2} [\hat{I}_z \hat{S}_- + \hat{I}_- \hat{S}_z] \sin \theta \cos \theta \exp(+i\phi) \\ E &= \frac{3}{4} [\hat{I}_+ \hat{S}_+] \sin^2 \theta \exp(-2i\phi) \\ F &= \frac{3}{4} [\hat{I}_- \hat{S}_-] \sin^2 \theta \exp(+2i\phi),\end{aligned}\quad (2.43)$$

where the internuclear vector between spin I and spin S is defined by the spherical polar co-ordinates (r, θ, ϕ) (the z -axis is defined by the direction of \mathbf{B}_0).

The Zeeman eigenstates for two interacting spin 1/2 nuclei can be represented by product states as shown in the energy level diagram in figure 2.8. Term B from the dipolar Hamiltonian alphabet links the $|\beta\alpha\rangle$ and $|\alpha\beta\rangle$

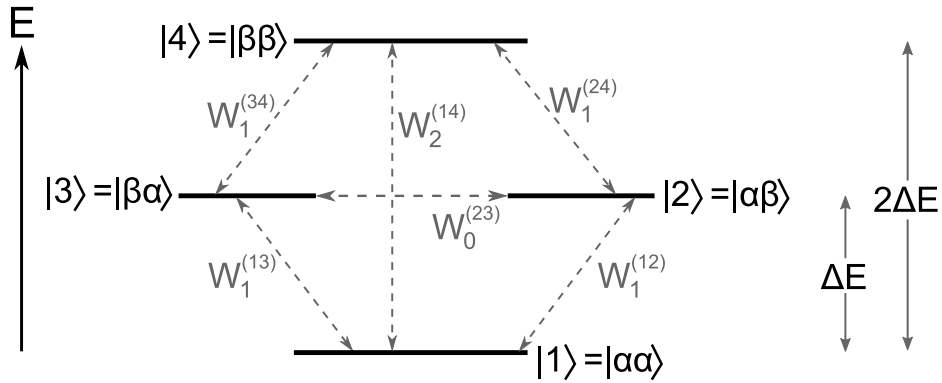


Figure 2.8: Energy level diagram of two interacting spin 1/2 nuclei. Zeeman eigenstates are given by product states. The various transition pathways are shown by dashed arrows.

states; when rendered time-dependent by fluctuations in the environment, it acts to simultaneously flip one spin up and the flip the other spin down, in

a process with zero net energy flow. The C and D terms cause single spin-flips, and join states separated by $\hbar\omega_L$. Finally, the E and F terms cause double spin-flips and join the $|\alpha\alpha\rangle$ and $|\beta\beta\rangle$ states, separated by $2\hbar\omega_L$.

The C , D , E and F terms cause the flow of energy between the spin system and the lattice. The corresponding transition rates W_i for these processes can be found from time dependent perturbation theory, as $\hat{\mathbf{H}}_{\text{DD}}$ is small compared to the Zeeman Hamiltonian $\hat{\mathbf{H}}_Z$. The subscript of W_i corresponds to the number of spins flipped during a transition.

As seen in section 2.2.1 a system of differential equations can be written that model the rate of change of population for each Zeeman state. Doing this for the two-spin system leads to the following differential equation for the rate of change of polarisation $\langle I_z \rangle$

$$\frac{d}{dt}\langle I_z \rangle = 2(W_1 + W_2)[\langle I_z \rangle - I_0] . \quad (2.44)$$

Polarisation $\langle I_z \rangle$ is directly proportional to M_z , so we may express a solution to this equation in terms of M_z ;

$$M_z(t) = M_0(1 - \exp(-t/T_1)), \quad (2.45)$$

where

$$T_1^{-1} = 2(W_1 + W_2) . \quad (2.46)$$

The transition probabilities per unit time, between states $|r\rangle$ and $|s\rangle$, can be evaluated using a Master equation;

$$\begin{aligned} \overline{W}_i &= \frac{1}{\hbar^2} \int_{-\infty}^{+\infty} G_{rs}(\tau) \exp(-i\omega_{rs}\tau) d\tau \\ &= \frac{1}{\hbar^2} \mathbb{J}_i(\omega_{rs}) . \end{aligned} \quad (2.47)$$

From equations (2.46) and (2.47) a general expression for T_1 can be found for a system of $I = 1/2$ spins [21];

$$T_1^{-1} = \frac{3}{2} I(I+1) \hbar^2 \gamma^4 [\mathbb{J}_1(\omega_L) + \mathbb{J}_2(2\omega_L)] . \quad (2.48)$$

The spectral density functions for single-flip and double-flip processes are determined by finding the Fourier spectra of the spatial parts of the relevant terms in $\hat{\mathbf{H}}_{\text{DD}}$ (i.e. terms C, D for single spin-flips, and E, F terms for

double spin-flips). If the spatial parts of the terms in the dipolar alphabet are expressed as

$$\begin{aligned}
 C &\rightarrow \frac{1}{r^3} \sin \theta \cos \theta \exp(-i\phi) = F^{(1)} \\
 D &\rightarrow \frac{1}{r^3} \sin \theta \cos \theta \exp(+i\phi) = F^{(-1)} \\
 E &\rightarrow \frac{1}{r^3} \sin^2 \theta \exp(-2i\phi) = F^{(2)} \\
 F &\rightarrow \frac{1}{r^3} \sin^2 \theta \exp(+2i\phi) = F^{(-2)} , \quad (2.49)
 \end{aligned}$$

then the spectral density functions can be written

$$\mathbb{J}_i(\omega) = \int_{-\infty}^{+\infty} \langle F^{(i)*}(\tau) F^{(i)}(0) \rangle \exp(i\omega\tau) d\tau . \quad (2.50)$$

If the correlation function is assumed to be mono-exponential, the following expression for T_1 is found by using equation (2.48) and evaluating the spectral density functions;

$$T_1^{-1} = S_D^2 \left(\frac{\tau_c}{1 + \omega^2 \tau_c^2} + \frac{4\tau_c}{1 + 4\omega^2 \tau_c^2} \right) . \quad (2.51)$$

The factor S_D is a strength factor determined by the geometrical arrangement of the atoms. The form of the strength factor is dependent on whether the sample is a powder or a single-crystal. In the case of a single-crystal sample S_D has an angular dependency, as the magnitude of the dipole-dipole interaction is dependent on the angle between the internuclear vector and the reference field. For a powder sample S_D is a constant. In both cases, S_D represents a lattice sum over all nuclear pairs.

Equation 2.51 has the form of two superimposed absorption Lorentzian lineshapes. Examination of this equation reveals how measurement of the longitudinal relaxation time gives information about motional processes that are central to causing spin-lattice relaxation to occur.

2.3 Methyl-group dynamics

At low temperature, methyl groups can be thought of as rigid rotors. The rotors experience a potential barrier, due to both inter- and intra-molecular electrostatic interactions, which hinders the rotational motion. Often, the

de Broglie wavelength of the methyl protons is comparable to the width of the hindering potential barriers, making quantum tunnelling possible. This section gives an overview of the quantum tunnelling model of methyl group rotation.

2.3.1 Rotational Hamiltonian

Methyl group moieties that are attached to larger molecules have only one rotational degree of freedom. Vibrational degrees of freedom can be ignored at room temperature and below, therefore the CH_3 group can be treated as a rigid rotor that rotates about the covalent bond between the carbon atom and the rest of the molecule. The rotational motion can be described

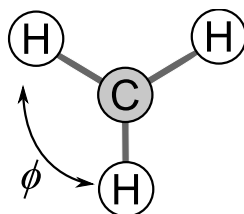


Figure 2.9: Schematic diagram of methyl rotor undergoing uniaxial rotation. ϕ is an angle describing the position of the methyl rotor.

in terms of the angle ϕ , and the Hamiltonian of a hindered methyl group is given by

$$\hat{\mathbf{H}}_{\text{R}} = \frac{-\hbar^2}{2I} \frac{\partial^2}{\partial \phi^2} + V(\phi), \quad (2.52)$$

where I is the moment of inertia of the methyl rotor (for a typical rotor, $I = 5.31 \times 10^{-47} \text{kg m}^2$), and $V(\phi)$ is a periodic hindering potential [18]. $V(\phi)$ has origins in both intermolecular and intramolecular electrostatic interactions [16]. Due to the three-fold symmetry of methyl groups, $V(\phi)$ is expressed as a Fourier sum of three-fold, six-fold and higher harmonics:

$$V(\phi) = \sum \frac{V_{3l}}{2} [1 - \cos(3l(\phi + \chi_{3l}))], \quad (2.53)$$

where l is an integer and χ is a phase angle. The minima of the hindering potential function correspond to the preferred orientations of the methyl rotor. The minima (or wells) are separated by a potential barrier (figure 2.10).

Methyl groups with one rotational degree of freedom are described by

the C_3 symmetry group. The rotational and nuclear spin eigenfunctions must transform according to the three irreducible representations of the C_3 group, A , E_a and E_b . The character table for this group is presented in table 2.1.

C_3	E	C_3^1	C_3^2
A	1	1	1
E	1	ϵ	ϵ^*
	1	ϵ^*	ϵ

Table 2.1: Character table for C_3 symmetry group ($\epsilon = \exp(2\pi i/3)$) [45].

2.3.2 Rotational eigenstates

The eigenstates of the rotational Hamiltonian can be found by a variation method, using harmonic oscillator pocket states which overlap in the barrier region, or by direct numerical diagonalisation of the rotational Hamiltonian, using the quantum free rotor eigenfunctions as the basis. The former method is accurate for high barrier systems, whereas direct diagonalisation is most suitable for low barrier systems; the latter method is described in detail below.

The free rotor eigenfunctions are given by

$$\varphi^{\text{free}} = (2\pi)^{-1/2} \exp(im\phi) \quad (2.54)$$

where $m = 0, \pm 1, \pm 2 \dots$. The matrix elements of $\hat{\mathbf{H}}_R$ are written

$$\begin{aligned} \hat{\mathbf{H}}_R^{(m,m')} &= \langle \varphi_m | \hat{\mathbf{H}}_R | \varphi_{m'} \rangle \\ &= \left(\frac{\hbar^2}{2I} m^2 + \frac{V_3}{2} + \frac{V_6}{2} \right) \delta(m, m') \\ &\quad - \frac{V_3}{4} \delta(m, m' \pm 3) - \frac{V_6}{4} \delta(m, m' \pm 6) . \end{aligned} \quad (2.55)$$

where $\delta(i, i) = 1$, and $\delta(i, j) = 0$ ($i \neq j$). The size of the matrix is determined simply by the computational power and time available. The matrix can be separated into three non-interacting matrices, which correspond to eigenstates with A , E_a and E_b symmetry. The $m = 0, \pm 3, \pm 6 \dots$ basis functions specify the A species, and the $m = 1, (1 \pm 3), (1 \pm 6) \dots$ and

$m = -1, (-1 \pm 3), (-1 \pm 6) \dots$ basis functions specify the E_a and E_b species, respectively. These matrices can be separately diagonalised and the resulting eigenstates are a ladder of librational (or torsional) states (ground state denoted by $n = 0$), which are split into states of A symmetry, and two degenerate states with E symmetry (see figure 2.10). The ordering of the

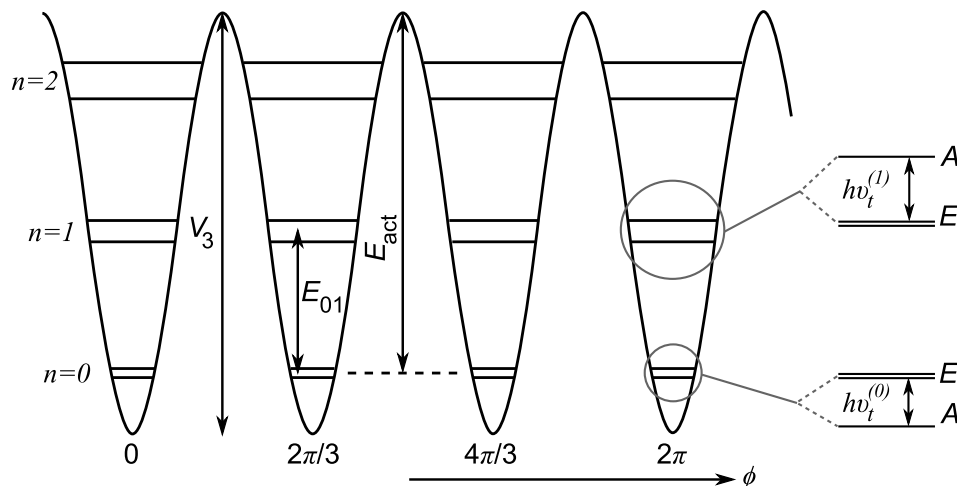


Figure 2.10: Schematic diagram of methyl rotor energy levels under the influence of a three-fold hindering potential. Librational energy levels denoted by quantum number n . E_{0n} is the transition energy between the ground state and the n^{th} librational level. Librational levels are split by tunnelling frequency $\nu_t^{(n)}$, into states with A and E symmetry. E_{act} is the energy barrier height, V_3 , minus the ground state energy. Figure adapted from [18].

symmetry species alternates with increasing librational energy level, i.e. the A species has lower energy when the torsional energy quantum number, n , is even, and the E species has lower energy when n is odd.

The splitting of the librational levels is proportional to the tunnelling frequency, $\nu_t^{(n)}$. The tunnel splitting is due to the quantum tunnelling of the methyl rotor. The values of the tunnel splitting and energy differences between librational states depend almost exclusively on the values of the harmonics of V (V_3, V_6 etc), which describe the hindering potential. The tunnelling frequency is extremely sensitive to the hindering potential that the rotor experiences. The dependence of the torsional splitting E_{01} , and the tunnel splitting of the ground state $\nu_t^{(0)}$, on the height of the potential barrier is presented in figure 2.11. E_{01} and $\nu_t^{(0)}$ were calculated by the diagonalisation process described above.

The torsional splitting E_{01} is often defined as the energy difference be-

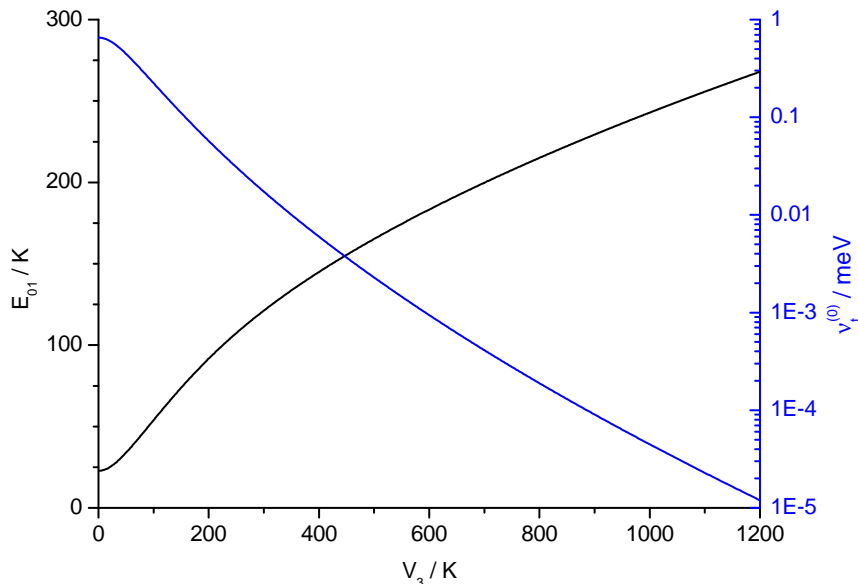


Figure 2.11: Dependence of E_{01} and $\nu_t^{(0)}$ on the height of a purely threefold barrier, calculated by diagonalisation of $\hat{\mathbf{H}}_R$.

tween the average energy of the tunnel-split ground librational state and the first excited librational state. However, for low barrier systems the torsional splitting has been observed to be the energy difference between the states of E -symmetry, in the ground and excited librational states [46]. For $V_3 > 300\text{K}$ the values of E_{01} as stated by these alternate definitions begin to converge, and the difference is negligible.

2.3.3 Spin-symmetry species

The Pauli Exclusion Principle imposes certain symmetry restrictions on the nuclear and spatial (i.e. rotational) wavefunctions of methyl groups. This results in the existence of spin-symmetry species. The total wavefunction of a methyl group is the product of vibrational, electronic, spatial and nuclear spin wavefunctions

$$\Psi_{\text{tot}} = \Psi_{\text{vib}}\Psi_{\text{elec}}\Psi_{\text{rot}}\Psi_{\text{nuc}} . \quad (2.56)$$

At low temperatures methyl groups are in the vibrational and electronic ground state, which are symmetric. Rotations of methyl groups are equivalent to even permutations of the protons; odd permutations are effectively

impossible at low temperature as this would require energies of many electronvolts. Therefore the product $\Psi_{\text{rot}}\Psi_{\text{nuc}}$ must be symmetric, i.e. of type A symmetry. Hence the only allowed wavefunctions are $|\Psi_{\text{rot}}^A\rangle|\Psi_{\text{nuc}}^A\rangle$, $|\Psi_{\text{rot}}^{E_a}\rangle|\Psi_{\text{nuc}}^{E_b}\rangle$ and $|\Psi_{\text{rot}}^{E_b}\rangle|\Psi_{\text{nuc}}^{E_a}\rangle$.

The nuclear spin wavefunctions are listed in table 2.2. Wavefunctions

Γ_S	m_I	$\psi_S(\Gamma_S, m_I)$
A	$3/2$	$ \alpha\alpha\alpha\rangle$
$I = 3/2$	$1/2$	$(1/\sqrt{3})(\alpha\alpha\beta\rangle + \alpha\beta\alpha\rangle + \beta\alpha\alpha\rangle)$
	$-1/2$	$(1/\sqrt{3})(\beta\beta\alpha\rangle + \beta\alpha\beta\rangle + \alpha\beta\beta\rangle)$
	$-3/2$	$ \beta\beta\beta\rangle$
E	$1/2$	$(1/\sqrt{3})(\alpha\alpha\beta\rangle + \epsilon \beta\alpha\alpha\rangle + \epsilon^* \alpha\beta\alpha\rangle)$
$I = 1/2$	$-1/2$	$(1/\sqrt{3})(\beta\beta\alpha\rangle + \epsilon \alpha\beta\beta\rangle + \epsilon^* \beta\alpha\beta\rangle)$
	$1/2$	$(1/\sqrt{3})(\alpha\alpha\beta\rangle + \epsilon^* \beta\alpha\alpha\rangle + \epsilon \alpha\beta\alpha\rangle)$
	$-1/2$	$(1/\sqrt{3})(\beta\beta\alpha\rangle + \epsilon^* \alpha\beta\beta\rangle + \epsilon \beta\alpha\beta\rangle)$

Table 2.2: Nuclear-spin wavefunctions for methyl groups. Γ_S denotes symmetry of wavefunction, and m_I is the z component of nuclear spin I . As above, $\epsilon = \exp(2\pi i/3)$ [16].

with type A symmetry are spin $3/2$ species, and type E species have spin $1/2$. In the presence of an external magnetic field the spin-symmetry species undergo Zeeman splitting, and the A species form a spin quartet, and the E species a pair of degenerate doublets.

2.3.4 Relaxation rate

A model for spin-lattice relaxation of rotating methyl groups was developed by Haupt [28] (see reference [30] for a review in English). In this model it is assumed that relaxation between librational levels are driven by phonons modulating the potential. The rapid transitions between librational levels ensure that thermal equilibrium is maintained between the lattice and the librational levels.

Due to the interdependence of the rotational and spin states, transitions between tunnelling states must be accompanied by a simultaneous transition between nuclear spin states. In the absence of paramagnetic impurities, transitions between A and E spin states are only possible via weak time-dependent intramolecular dipolar interactions, which couple spatial and spin degrees of freedom. Therefore conversion between A and E symmetry species is an extremely slow process in low-barrier systems, where

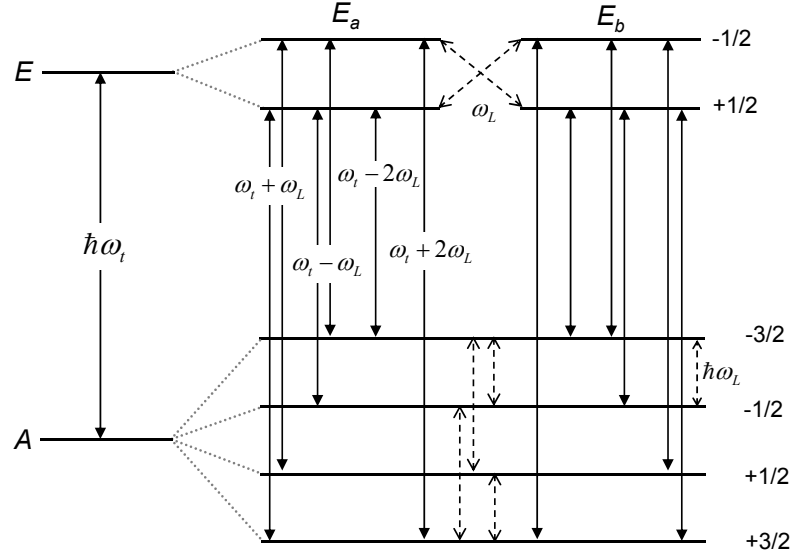


Figure 2.12: Zeeman splitting of tunnelling states in librational ground state, and non-zero matrix elements of intramolecular (solid arrows) and intermolecular (dashed arrows) dipolar Hamiltonian.

the tunnel splitting is large compared to the dipolar interaction. Matrix elements for transitions between tunnelling states are non-zero for frequencies $\omega_t^0 + \omega_L$, $\omega_t^0 - \omega_L$, $\omega_t^0 + 2\omega_L$ and $\omega_t^0 - 2\omega_L$.

Relaxation amongst levels of the same symmetry is driven by intermolecular dipolar interactions. A - A and E - E transitions have no symmetry restrictions, and occur much more readily. The non-zero matrix elements for these transitions are at frequencies ω_L and $2\omega_L$.

By summing up the probabilities of the individual transitions, Haupt obtained the following expression for the spin-lattice relaxation rate [28];

$$\begin{aligned}
 \frac{1}{T_1} &= C_{AE} f(\omega_t, \omega_L, \tau_c) + C_{EE} g(\omega_L, \tau_c) \\
 &= C_{AE} \sum_{n=1}^2 \left(\frac{n^2 \tau_c}{1 + (\omega_t + n\omega_L)^2 \tau_c^2} + \frac{n^2 \tau_c}{1 + (\omega_t - n\omega_L)^2 \tau_c^2} \right) \\
 &\quad + C_{EE} \sum_{n=1}^2 \frac{n^2 \tau_c^2}{1 + n^2 \omega_L^2 \tau_c^2} \tag{2.57}
 \end{aligned}$$

where C_{AE} and C_{EE} are the intramolecular and intermolecular dipolar coupling constants, respectively. τ_c is a correlation time, which is characteristic of the motion of the methyl group. In the low temperature limit τ_c is given by the Arrhenius rate law

$$\tau_c^{-1} = \tau_0^{-1} \exp(-E_{01}/k_B T) , \quad (2.58)$$

where E_{01} is the energy difference between the ground and first excited librational state. Notice the similarity between the Haupt expression for spin-lattice relaxation due to methyl group tunnelling, and the “classical” expression from the BPP formalism (equation (2.51)). Indeed the Haupt expression reduces to the BPP expression for high barriers and high temperatures.

Equation (2.57) describes the spectral density function of the dipole-dipole interaction in powder samples with rotating methyl groups. The relaxation rate is dependent on ω_L and the correlation time τ_c . These variables are themselves dependent on the magnetic field strength and temperature, respectively (equations (2.12) and (2.58)). This dictates the experimental approach for studying the methyl group dynamics. T_1 is measured as a function of temperature and also as a function of magnetic field, in order to determine the spectral density function of the magnetic dipolar interaction.

The evolution of the spectral density functions as temperature increases is shown in figure 2.13(a). The width of the Lorentzian function that describes the spectral density function is proportional to the correlation rate τ_c^{-1} . As τ_c^{-1} is governed by the Arrhenius rate law, broadening of the spectral density functions occurs with increasing temperature. Resonant tunnelling sideband peaks occur in the spectral density functions when the Larmor frequency is of a similar magnitude to the tunnelling frequency. However, in the low-barrier systems studied in this thesis, the tunnelling frequencies are much greater than the Larmor frequencies achievable in the laboratory, therefore no resonant features were expected, and the AE term in equation (2.57) could be neglected.

Measurements of T_1 as a function of temperature sample the spectral density function at fixed positions, depending on the relaxation field. Figure 2.13(b) shows T_1^{-1} vs. inverse temperature curves for three distinct relaxation fields. For each field strength the value of T_1 goes through a

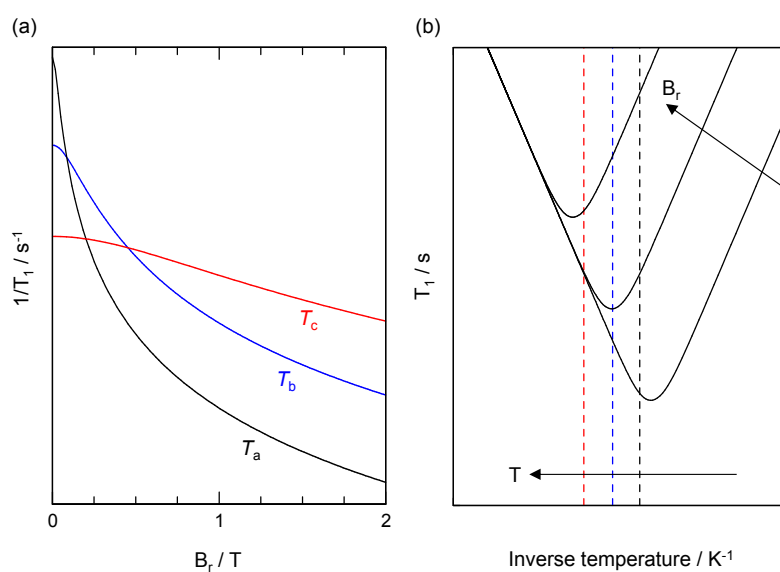


Figure 2.13: Characteristic curves of (a) T_1^{-1} vs. B_r (spectral density functions) and (b) T_1 vs. T^{-1} . Spectral density functions shown for three distinct temperatures ($T_a < T_b < T_c$). Dashed coloured lines in figure (b) correspond to the temperatures indicated by the colours in figure (a). The curves shown are typical of those expected from BPP theory, or from methyl rotor systems with low hindering barriers, where $\omega_t \gg \omega_L$.

minimum point at some temperature θ_{\min} . The gradient of the T_1 vs. inverse temperature curves either side of θ_{\min} is determined by E_{01} , the energy difference between the ground and first excited librational state.

For higher fields the position of θ_{\min} occurs at higher temperatures and the minimum is less deep (i.e. $T_1(\theta_{\min})$ is longer). The BPP expression for T_1 is minimised when $\omega_L\tau_c = 0.6158$. In cases where the Larmor frequency is of a similar magnitude to the tunnelling frequency a second minimum becomes apparent, the position of which is field-independent. In low-barrier systems no such peak is expected for the reasons described above.

At high temperatures the system enters the fast motion regime, where T_1 is given by $(5\tau_c C)^{-1}$. In the fast motion limit, the relaxation time is independent of ω_L , therefore the T_1 vs. inverse temperature curves for different field strengths converge. This corresponds to spectral density functions that are very broad and flat.

Temperature and field-dependent measurements of T_1 are typically carried out over several days and weeks, during which time the distribution of methyl groups of *A* and *E*-type symmetry approaches equilibrium. However the conversion between symmetry species does not affect the proton spin-lattice relaxation, as long as there is no resonant contact between the Zeeman and methyl-tunnelling energy reservoirs.

2.4 INS fundamentals

Neutron scattering is an experimental technique used for studying condensed matter. Neutrons are electrically neutral particles, which makes them very useful for penetrating matter and probing the positively charged atomic nucleus. Moreover, they can be used to study magnetic phenomena due to their non-zero spin ($I = 1/2$).

Broadly speaking, neutron scattering experiments can be divided into two types: elastic neutron scattering, and inelastic neutron scattering (INS). INS is used to study dynamic processes, such as molecular motion or diffusion, whereas elastic neutron scattering is used to study the structure or texture of a sample.

In this thesis, INS has been employed to observe the quantum mechanical motion of a hydrogen molecule entrapped in a fullerene cage. This section will introduce some fundamental concepts of INS, and demonstrate how it

may shed light on dynamical processes in condensed matter.

2.4.1 Scattering cross-section

INS involves measuring the energy and momentum of neutrons scattered by a sample, and comparing this to the energy and momentum of the incident beam of monochromatic neutrons. The momentum transfer $\hbar\mathbf{Q}$ and energy transfer $\hbar\omega$ are given by the following;

$$\begin{aligned}\hbar\mathbf{Q} &= \hbar\mathbf{k}' - \hbar\mathbf{k}_0 \\ \hbar\omega &= \hbar^2 \left(\frac{k'^2 - k_0^2}{2m_n} \right)\end{aligned}\quad (2.59)$$

where \mathbf{k}_0 and \mathbf{k}' are the incident and scattered neutron wave-vectors, and m_n is the neutron mass (figure 2.14).

The ability of the scattering systems to scatter neutrons is characterised by a quantity known as the *scattering cross-section* σ_S , which has units of area (usually expressed in Barns; 1 Barn = 10^{-28}m^2). In neutron scattering experiments the *partial differential cross-section* is measured. σ_S is a measure of the scattering cross-section over all energies, and in all directions. The differential scattering cross-section $d\sigma/d\Omega$, is a measure of the number of neutrons scattered per second into a small solid angle $d\Omega$, in the direction defined by θ and ϕ .

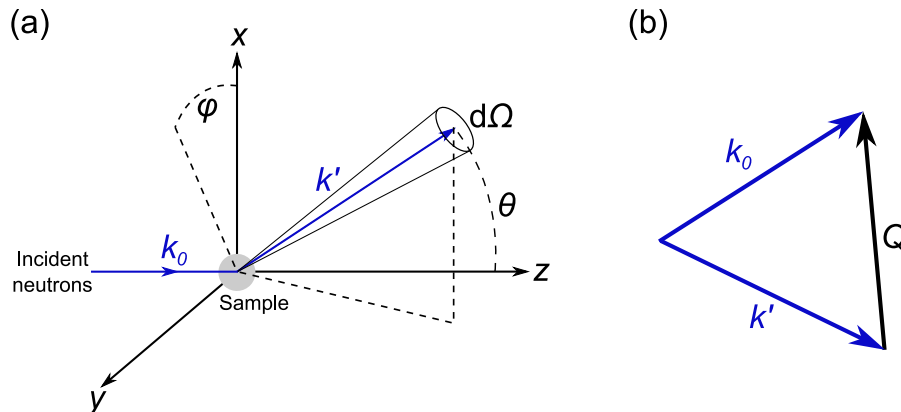


Figure 2.14: (a) Geometry of INS system; (b) Momentum transfer Q is defined as the difference between k_0 and k' , the incident and scattered neutron wave vectors, respectively.

The partial differential cross-section (or *double differential cross-section*) $d^2\sigma/d\Omega dE'$ is the number of neutrons per second through a small solid angle $d\Omega$ (in the direction θ and ϕ), with final energy between E' and dE' .

The scattering cross-section depends on the probability of a neutron causing a transition in the sample, between states λ_0 and λ' . If the probability of such a transition is denoted by $W_{k_0\lambda_0\rightarrow k'\lambda'}$, we may write

$$\left(\frac{d\sigma}{d\Omega}\right)_{\lambda_0\rightarrow\lambda'} = \frac{1}{\Phi} \frac{1}{d\Omega} \sum_{\substack{k' \\ \text{in } d\Omega}} W_{k_0\lambda_0\rightarrow k'\lambda'} , \quad (2.60)$$

where Φ is the neutron flux.

$W_{k_0\lambda_0\rightarrow k'\lambda'}$ can be evaluated using Fermi's Golden rule

$$W(k_0\lambda_0\rightarrow k'\lambda') = \frac{2\pi}{\hbar} |\langle k'\lambda' | \widehat{V} | k_0\lambda_0 \rangle|^2 \delta(E_{\lambda'} - E_{\lambda_0} - \hbar\omega) \quad (2.61)$$

where \widehat{V} is a potential which describes the interaction between the neutron and the sample (e.g. a nuclear interaction with matter, magnetic interaction between a nucleus and neutron). The delta function in the expression above ensures the conservation of energy (energy imparted to sample $\hbar\omega$ is equal to energy lost by neutrons $E_{\lambda_0} - E_{\lambda'}$ or vice-versa).

By combining equations (2.60) and (2.61), and by using box normalisation, the following expressions for the differential and double-differential cross-sections can be derived [47];

$$\left(\frac{d\sigma}{d\Omega}\right)_{\lambda_0\rightarrow\lambda'} = \frac{k'}{k} \left(\frac{m_n}{2\pi\hbar^2}\right)^2 |\langle k'\lambda' | \widehat{V} | k_0\lambda_0 \rangle|^2 \quad (2.62)$$

$$\left(\frac{d^2\sigma}{d\Omega dE'}\right)_{\lambda_0\rightarrow\lambda'} = \left(\frac{d\sigma}{d\Omega}\right)_{\lambda_0\rightarrow\lambda'} \delta(E_{\lambda_0} - E_{\lambda'} - \hbar\omega) , \quad (2.63)$$

where m_n is the neutron mass.

2.4.2 Fermi pseudo-potential and scattering length

The exact form of \widehat{V} in equation (2.61) is not known, but as it is small compared to the wavelength of the incident neutrons (i.e. within the limits of the Born approximation) it may be expressed as a *Fermi pseudo-potential*. \widehat{V} is characterised by a delta function and a single parameter \mathbf{b} , known as

the scattering length

$$\widehat{V}(\mathbf{r} - \mathbf{r}_i) = \frac{2\pi\hbar^2}{m_n} b_i \delta(\mathbf{r} - \mathbf{r}_i) . \quad (2.64)$$

r_i is the position of nucleus i , which has scattering length b_i ; r is the neutron position.

The equation for the partial-differential scattering cross-section, introduced above, only deals with specific transitions in the sample, i.e. the sample going from initial state λ_0 to final state λ' . The actual partial differential cross-section that is measured by experiment accounts for transitions between a multitude of states. It is therefore necessary to carry out a sum over all of the final states λ' , whilst keeping the initial state λ_0 fixed, and then average over λ_0

$$\begin{aligned} \left(\frac{d^2\sigma}{d\Omega dE'} \right) &= \sum_{\lambda_0 \lambda'} p_{\lambda_0} \left(\frac{d^2\sigma}{d\Omega dE'} \right)_{\lambda_0 \rightarrow \lambda'} \quad (2.65) \\ &= \frac{k'}{k_0} \sum_{\lambda_0} p_{\lambda_0} \sum_{\lambda'} |\langle \lambda' | \sum_{i=1}^N \mathbf{b}_i \exp(i\mathbf{Q} \cdot \mathbf{r}_i) | \lambda_0 \rangle|^2 \delta(\hbar\omega + E_{\lambda_0} - E_{\lambda'}) . \end{aligned}$$

p_{λ_0} is the probability of the scattering system being in initial state λ_0 , and is determined by the Boltzmann distribution.

2.4.3 Coherent and incoherent scattering

In practice, a sample studied using neutron scattering will have numerous scattering systems, with a distribution of scattering lengths \mathbf{b}_i , which are dependent on the type of isotope and the spin state at each site. The scattering cross-section measured by experiment is very close to the cross-section averaged over all the scattering systems. From inspection of equation (2.65) it can be seen that the cross-section is essentially governed by

$$\left| \sum_{i=1}^N \mathbf{b}_i \langle \lambda' | \exp(i\mathbf{Q} \cdot \mathbf{r}_i) | \lambda_0 \rangle \right|^2 = \sum_{j=1}^N \mathbf{b}_j^* \langle \lambda' | \exp(i\mathbf{Q} \cdot \mathbf{r}_j) | \lambda_0 \rangle^* \sum_{i=1}^N \mathbf{b}_i \langle \lambda' | \exp(i\mathbf{Q} \cdot \mathbf{r}_i) | \lambda_0 \rangle . \quad (2.66)$$

Seeing as each individual \mathbf{b}_i cannot be known, this must be rewritten as an average

$$\begin{aligned}
\left| \sum_{i=1}^N \mathbf{b}_i \langle \lambda' | \exp(i\mathbf{Q} \cdot \mathbf{r}_i) | \lambda_0 \rangle \right|^2 &= \sum_{i=j} |\mathbf{b}_i|^2 \langle j |^* \langle i \rangle + \sum_{i \neq j} \mathbf{b}_j^* \mathbf{b}_i \langle j |^* \langle i \rangle \\
&= \overline{(b^2)} \left| \sum_i \langle i \rangle \right|^2 + (\bar{b})^2 \sum_{i \neq j} \langle j |^* \langle i \rangle \\
&= \left(\overline{(b^2)} - (\bar{b})^2 \right) \left| \sum_i \langle i \rangle \right|^2 + (\bar{b})^2 \sum_{i,j} \langle j |^* \langle i \rangle . \quad (2.67)
\end{aligned}$$

In the above rearrangement it is assumed that there is no correlation between different nuclei, i.e.

$$\begin{aligned}
\overline{b_{j'} b_j} &= (\bar{b})^2, & j' \neq j \\
\overline{b_{j'} b_j} &= \overline{(b^2)}, & j' = j .
\end{aligned} \quad (2.68)$$

This allows us to rewrite equation (2.65) as the sum of two components, namely an *incoherent* component and a *coherent* component

$$\begin{aligned}
\left(\frac{d^2 \sigma}{d\Omega dE'} \right) &= \left(\frac{d^2 \sigma}{d\Omega dE'} \right)_{\text{coh}} + \left(\frac{d^2 \sigma}{d\Omega dE'} \right)_{\text{inc}} \quad (2.69) \\
\left(\frac{d^2 \sigma}{d\Omega dE'} \right)_{\text{coh}} &\propto \frac{k'}{k_0} \sigma_{\text{coh}} S_{\text{coh}}(Q, \omega) \\
\left(\frac{d^2 \sigma}{d\Omega dE'} \right)_{\text{inc}} &\propto \frac{k'}{k_0} \sigma_{\text{inc}} S_{\text{inc}}(Q, \omega) .
\end{aligned}$$

$S_{\text{coh}}(Q, \omega)$ and $S_{\text{inc}}(Q, \omega)$ are the coherent and incoherent *scattering functions* (often referred to as the *scattering laws*), respectively, and σ_{coh} and σ_{inc} are the coherent and incoherent scattering cross-sections, respectively, given by

$$\begin{aligned}
S_{\text{coh}}(Q, \omega) &= \frac{1}{N} \sum_{\lambda_0, \lambda'} p_{\lambda_0} \sum_i |\langle \lambda' | \exp(i\mathbf{Q} \cdot \mathbf{r}_i) | \lambda_0 \rangle|^2 \delta(\hbar\omega + E_{\lambda_0} - E_{\lambda'}) \quad (2.70) \\
S_{\text{inc}}(Q, \omega) &= \frac{1}{N} \sum_{\lambda_0, \lambda'} p_{\lambda_0} \sum_{i,j} \langle \lambda' | \exp(i\mathbf{Q} \cdot \mathbf{r}_i) | \lambda_0 \rangle \langle \lambda_0 | \exp(i\mathbf{Q} \cdot \mathbf{r}_j) | \lambda' \rangle \delta(\hbar\omega + E_{\lambda_0} - E_{\lambda'})
\end{aligned}$$

$$\begin{aligned}
\sigma_{\text{coh}} &= 4\pi (\bar{b})^2 \\
\sigma_{\text{inc}} &= 4\pi \left(\overline{(b^2)} - (\bar{b})^2 \right) . \quad (2.71)
\end{aligned}$$

The coherent scattering is dependent on the correlation of the position of different atoms, and therefore gives rise to interference effects. The incoherent scattering contains no information about correlation between different

atoms; the incoherent scattering is dependent on the mean square deviation of the scattering lengths from their mean value. The incoherent scattering function $S_{\text{inc}}(Q, \omega)$ is a double Fourier transform of the autocorrelation function of the atom positions. Likewise, the coherent scattering function related to the pair-correlation function of the atom positions via a double Fourier transform.

In INS experiments the energy of scattered neutrons is compared to the energy of the incident neutrons to produce an energy excitation spectrum of the sample. The spectrum is governed by the incoherent scattering function. $S_{\text{inc}}(Q, \omega)$ also has a dependence on momentum transfer Q ; Q -dependence of $S_{\text{inc}}(Q, \omega)$ can reveal spatial information about dynamic processes that occur in the sample (e.g. rotation and translation).

2.5 Dynamics of confined H₂

At low temperatures, confined endohedral hydrogen molecules have three translational and two rotational degrees of freedom (the vibrational splitting is approximately 6000K and so may be neglected). Both the rotational and translational motion of endohedral hydrogen is quantised and the Hamiltonian for the quantum motion is given by [48]

$$\hat{\mathbf{H}} = -\frac{\hbar^2}{2\mu}\nabla^2 + \frac{\hbar^2}{B_J}\hat{L}^2 + \hat{V}(r, \theta, \phi) , \quad (2.72)$$

where μ is the mass of the molecule, $B_J = 7.4\text{meV}$ (86K in temperature units) is the rotational constant of molecular hydrogen, and \hat{L} is the angular momentum quantum operator. The spatial states of the confined molecule are describable by five quantum numbers; the rotational quantum numbers $\{J, m_J\}$ and the translational quantum numbers $\{n, l, m_l\}$. Rotational-translational coupling is omitted from the Hamiltonian for simplicity.

In a perfectly spherical rotational potential, the H₂ rotational levels have a g_J -fold degeneracy, where $g_J = 2J + 1$, and the translational levels have a degeneracy of $g_L = 2L + 1$ (figure 2.15). A non-spherical cavity causes the H₂ molecule to experience a non-isotropic rotational potential, which lifts the degeneracy of the excited rotational levels. The degeneracy of the translational states is also lifted as the spherical symmetry of the cavity is

broken. Splitting of these levels may be revealed in an INS spectrum.

As with rotating methyl-groups, the Pauli exclusion principle places restrictions on the symmetry of the wavefunction that describes the hydrogen molecule. The total wavefunction of molecular hydrogen is a product of the rotational, translational, vibrational, electronic and nuclear wavefunctions [49]

$$\Psi_{\text{tot}} = \Psi_{\text{rot}} \Psi_{\text{trans}} \Psi_{\text{vib}} \Psi_{\text{elec}} \Psi_{\text{nuc}} . \quad (2.73)$$

By considering the symmetry properties of the component wavefunctions, it emerges that the product $\Psi_{\text{rot}} \Psi_{\text{nuc}}$ must be anti-symmetric upon exchange of identical fermions. The rotational wavefunctions are given by the spherical harmonics $Y_J^{m_J}(\theta, \phi)$. The spherical harmonics are also eigenfunctions of the parity operator, with eigenvalue $(-1)^J$. Therefore $J = \text{even}$ rotational states are symmetric and must combine with anti-symmetric nuclear spin states in order to satisfy the Pauli exclusion principle. Likewise $J = \text{odd}$ rotational states are anti-symmetric and must combine with symmetric nuclear spin states.

For a two spin- $\frac{1}{2}$ system there are four possible spin states, denoted χ_{I,m_I} , where I is the spin quantum number. There is a spin $I = 0$ *singlet* state given by

$$\chi_{0,0} = \frac{1}{\sqrt{2}}(\alpha(1)\beta(2) - \beta(1)\alpha(2)) , \quad (2.74)$$

which is anti-symmetric in the exchange of spin coordinates. The $I = 1$ states form a spin *triplet*

$$\begin{aligned} \chi_{1,1} &= \alpha(1)\alpha(2) \\ \chi_{1,0} &= \frac{1}{\sqrt{2}}(\alpha(1)\beta(2) + \beta(1)\alpha(2)) \\ \chi_{1,-1} &= \beta(1)\beta(2) , \end{aligned} \quad (2.75)$$

which are symmetric in the exchange of spin coordinates. The spin singlet and spin triplet describe distinct species of molecular hydrogen. The $I = 0$ species is known as *parahydrogen*, which has symmetric rotational wavefunctions of $J = \text{even}$. The $I = 1$ species is known as *orthohydrogen*, and has antisymmetric rotational wavefunctions of $J = \text{odd}$.

The symmetry constraint that links the rotational states and nuclear spin states ensures that inter-conversion between para- and orthohydrogen is a

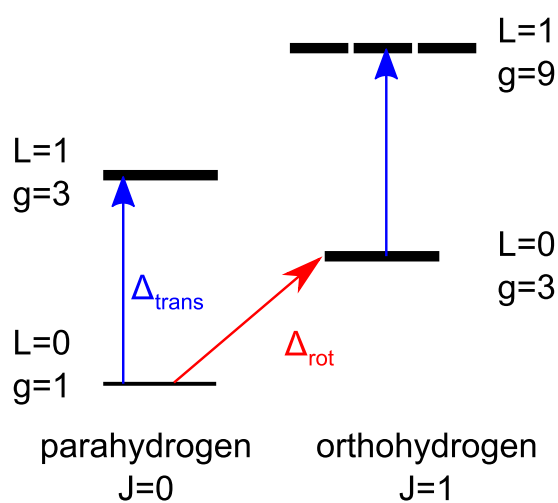


Figure 2.15: Energy level diagram of molecular hydrogen confined in a spherical environment. Two lowest-lying translational and rotational states shown only. Degeneracy of energy levels is denoted $g = g_J g_L$.

spin-dependent transition, which occurs with vanishingly small probability in the absence of a paramagnetic species. The transition may also be induced by interaction with a neutron, due to its non-zero magnetic moment. It is apparent that, in addition to effects such as quantisation, the Pauli exclusion principle can have a profound influence on the dynamics of the H_2 molecule in its cage.

Chapter 3

Experimental Details

3.1 Field-cycling NMR

Field-cycling NMR is a powerful technique for measuring the frequency dependence (or dispersion) of magnetic relaxation rates. In the previous chapter the dependence of the proton spin-lattice relaxation rate T_1^{-1} on the Larmor frequency was established (section 2.2.1 and 2.3.4). Stochastic motion within the sample causes protons to experience time-dependent magnetic dipole interactions over a large range of frequencies; the frequency dependence of these interactions is referred to as the spectral density function. The components of these interactions that are close to ω_L or $2\omega_L$ are able to induce relaxation of the protons. Field-cycling NMR is the preferred method of measuring T_1^{-1} as a function of ω_L (or equivalently the magnetic field B) in order to directly measure spectral density functions.

3.1.1 Field-cycling magnet

NMR is an inherently narrowband technique, due to the trade-off that exists between bandwidth and sensitivity of RF detection circuits (see section 3.1.3). In order to make frequency-dependent measurements of relaxation times it is necessary to be able to make rapid excursions in magnetic field strength.

The vast majority of superconducting magnets used for NMR spectroscopy operate in *persistent* mode i.e. the solenoid, once cooled below the critical temperature, is energised with an electric current, which circulates indefinitely without Ohmic loss. Altering the magnetic field pro-

duced by persistent mode superconducting magnet requires changing the current, which is an involved process that can take hours to complete. However field-cycling NMR is possible with a persistent mode magnet by using the ‘sample-shuttle technique’, in which the sample is mechanically moved within the magnet bore, to regions of lower field strength [50]. This technique requires moving the sample in a controlled way with a necessarily high degree of precision, which can be challenging to implement. Alternatively, it is possible to achieve fast-switching of magnetic field strength by using a low-inductance superconducting solenoid connected to a power supply capable of quickly switching the current through the coil —this is the approach adopted by our laboratory at the University of Nottingham.

According to Faraday’s Law, changing the current I passing through a solenoid induces a back EMF, and the terminal voltage across the solenoid is equal to

$$V = L \frac{dI}{dt}, \quad (3.1)$$

where L is the self-inductance of the coil, given by

$$L = \frac{\mu_0 \mu_r N^2 A}{l}, \quad (3.2)$$

for a coil of length l , N turns, and cross-sectional area A . μ_r is the relative permeability of the medium filling the coil, and μ_0 is the vacuum permeability. The magnetic field produced by a solenoid is given by

$$B = \frac{\mu_0 \mu_r N I}{l}. \quad (3.3)$$

It is clear from equation (3.1) that for a constant applied voltage across a solenoid, the current-switching (and therefore field-switching) rate is higher for coils of lower inductance. Inductance can be minimised by reducing the number of turns, but this also has the effect of reducing the magnetic field. Strong magnetic fields are favourable for NMR experiments due to the benefits in signal-to-noise, and in order to achieve this with a low-inductance coil, large currents are necessary. All of these factors need to be considered in designing a field-cycling magnet. Table 3.1 lists the compromised specifications of the custom-built niobium-tin magnet used in our laboratory, when working in conjunction with a Cryogenic SMS160C-H power supply.

The magnet has two modes of operation, namely *Internal* control and

Inductance	23mH
Max. operating current	160A
Max. field	2.5T
Max. ramping rate	10Ts ⁻¹
Field/current ratio	167GA ⁻¹
Length	72mm
Bore diameter	35.4mm
Duty cycle	Infinity

Table 3.1: Specifications of the University of Nottingham field-cycling magnet.

External control. In internal mode, a constant field can be set via the front panel of the power supply. Using external control the magnet power supply is controlled via a custom-built software GUI, which makes specially designed, time-dependent field profiles possible (section 3.1.5).

If a superconductive magnet loses its superconductivity and develops a finite resistance, it is said to have become ‘quenched’. This can cause a hazardous amount of helium boil-off, and even damage the solenoid. When operating in internal mode, the magnet power supply has a built-in quench detection facility, which instantaneously switches the current to zero in the event of detecting an increasingly resistive load. In external mode it was necessary to employ a home-built quench-protection system. This consists of a PC that monitors the shunt resistance of the power supply. A Visual Basic program running on the monitoring PC triggers a relay to disable the magnet power supply if a quench is detected.

3.1.2 Cryostat and VTI

The magnet is situated in a standard helium bath cryostat. During operation, the magnet is immersed in a liquid helium reservoir in order for it to remain under the critical superconducting temperature. Insulation from room temperature is achieved via an evacuated barrier and a large liquid nitrogen reservoir, which serves to reduce the rate of helium boil-off. The electrical connection leads between the magnet and the power supply act as heat conductors between the helium reservoir and the outside world, and their finite resistance cause them to heat up when carrying current. Both of these factors contribute to the helium boil-off rate.

The cryostat is equipped with a stainless steel variable temperature in-

sert (VTI). The VTI has a 24mm diameter sample bore, into which an NMR probe can be loaded. An evacuated outer jacket isolates the sample space and the cryogenic liquid reservoirs. The sample temperature is controlled by the combined action of a resistive wire heater mounted on the probe, and a flow of helium gas over the sample. Helium is drawn from the main reservoir into the sample space through a thin capillary and a heat exchanger. Flow through the capillary is regulated via a precision stainless steel needle valve. Increased helium flow, and therefore lower sample temperatures, can be achieved by pumping the sample space with a vacuum pump.

The sample temperature is monitored by a calibrated Cernox resistor, mounted on the probe. The Cernox thermometer and sample heater are both connected to a Lakeshore 331 temperature controller, and the desired sample temperature is maintained by PID control. Sample temperatures between 4.2 and 300K are routinely possible, with a drift of less than $\pm 1\%$ once settled.

3.1.3 NMR spectrometer

Broadly speaking a NMR spectrometer has two functions; to transmit pulses of radio frequency electromagnetic radiation to a sample, and then to detect and record the nuclear magnetic resonance signal (FID) generated by the spins. A simplified diagram is displayed in figure 3.1.

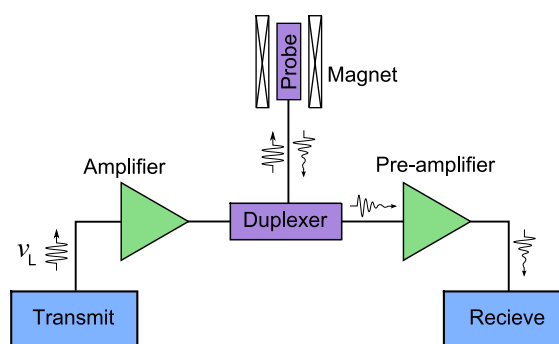


Figure 3.1: Schematic diagram of a NMR spectrometer

The pulses of RF radiation are produced by the transmitter section of the spectrometer (described in further detail below). After amplification, the RF pulse (of frequency ν_L , i.e. the Larmor frequency of the nuclei of

interest) reaches the duplexer. The duplexer acts as a fulcrum between the transmitter and receiver sections of the spectrometer. It is designed to protect the receiver section of the spectrometer from high voltages. The receiver section is designed to carry the weak voltages generated by the sample and may be damaged if exposed to the strong RF pulses. The duplexer must therefore direct strong RF pulses through the probe for transmission to the sample, and divert weak RF signals induced by the sample towards the receiver.

The probe is a LC tank circuit that has a resonant frequency equal to the Larmor frequency of the nuclei of interest. The inductance coil of a probe is located in the region of highest field homogeneity. The sensitivity of a NMR probe is characterised by the quality factor $Q = \nu_0/\Delta\nu$, where ν_0 is the resonant frequency and $\Delta\nu$ is the bandwidth. Due to the small magnitude of NMR signals, it is necessary to use high Q circuits for NMR applications, at the expense of the probe bandwidth.

Inductance coils in NMR probes routinely serve the dual purpose of acting as transmission and receiver coils. Following the last pulse of a sequence of RF pulses, and after a short delay known as the *dead time*, the spectrometer detects the FID signal generated in the coil. The signal passes through the duplexer and is directed towards the receiver via a *signal preamplifier*.

For the NMR experiments presented here, a Tecmag Apollo heterodyne spectrometer was used. The Apollo console incorporates both transmission and receiver electronics. The timing resolution of the spectrometer is 100ns, with minimum pulse lengths of 300ns. On the receiver side, the Apollo console incorporates a quadrature receiver and two ADC cards. The sampling interval was 400ns, and the FID was sampled over 1024 points. The Apollo spectrometer is controlled by the software package NTNMR, also developed by Tecmag. NTNMR supports OLE (object linking and embedding) control, which enables the spectrometer to be controlled vicariously by custom-built software. A Visual Basic (VB) program has been developed in-house in order to gain a high level of automation over controlling the spectrometer, and also processing the acquired FIDs (section 3.1.6).

A schematic diagram of a simple heterodyne NMR spectrometer is displayed in figure 3.2. The main advantage of a heterodyne system is that the observation frequency of the spectrometer can be altered simply by changing the probe; no further changes to the receiver electronics is necessary. The

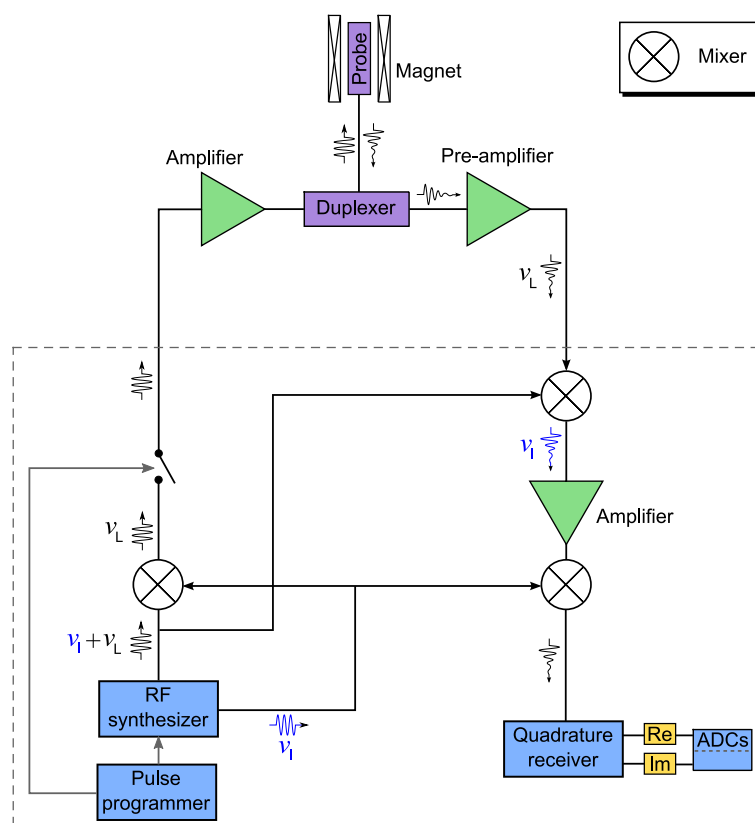


Figure 3.2: Schematic diagram of a heterodyne NMR spectrometer. Dashed lines show the components integrated into the Tecmag Apollo console.

technique of heterodyning involves generating waveforms by mixing together two waveforms of different frequencies. In practice this is achieved by using double balanced mixers, which take two waveforms as inputs and produces the sum and difference frequencies as outputs [51].

In a heterodyne system the receiver amplifier, is tuned to a particular frequency (the intermediate frequency ν_1) in order to minimise the contribution of broadband noise. All signals detected by the probe are shifted to this frequency before being amplified and recorded by the quadrature receiver.

The quadrature receiver records two signals, separated by 90° of phase, known as the real and imaginary parts of the signal. This is necessary in order to distinguish the relative sign of NMR frequencies that are greater or less than ν_L (see section 2.1.7). The real and imaginary signals are encoded by *analogue-to-digital convertors* (ADCs). Typical ADC cards are not able to encode signals greater than a few MHz, therefore it is necessary to down-shift the signal to more manageable frequencies. This is done by mixing the NMR signal with the intermediate frequency ν_1 —the resulting FID is effectively the NMR signal in the rotating frame of reference. Following the analogue-to-digital conversion, the FID is ready to be manipulated and analysed using appropriate computer software.

3.1.4 Probes

Given the fields that could be produced by the field-cycling magnet, the resonant frequency of the probes used for measurements in this thesis ranged from 29.8 to 38.6MHz (see table 3.2). The tank circuits were series LC circuits, with copper solenoid inductors. The solenoids were mounted on Kel-F formers for stability, and were 1cm in length, with a diameter of 8mm. The probes have been designed such that the filling factor of the

Probe	ν_0/MHz	$B_{\text{nmr}}(^1\text{H})/\text{T}$	Sample bore
A	29.8	0.7	5mm
B	36.7	0.86	5mm
C	38.64	0.91	3mm

Table 3.2: Specifications of NMR probes used. All probes were manufactured in-house. ‘Sample bore’ refers to the diameter of the bore.

coil is large for samples of limited mass and availability. The magnitude of

the NMR signal from a sample that only partially fills the receiver coil will suffer due to a reduced filling factor. Small coils were necessary as many of the samples studied in this thesis were synthesised in batches of the order of 100mg.

Another important design consideration for a field-cycling probe is the quality factor and its effect on the *excitation spectrum* of the probe. As mentioned in section 3.1.3, sensitivity is maximised for probes with large Q -factors. However, this is at the expense of the frequency response of the probe. For a field-cycling system where the reproducibility of the field may be the order of 1 Gauss following a field switch, it is desirable for the frequency response to be fairly flat about ν_0 . The magnetic field at the time of FID acquisition can take any of a range of values, which results in a disparity between the Larmor frequency of the protons and ν_0 . As well as using probes with a flat frequency response about ν_0 , the effect of deviations from the target field on the NMR signal can also be countered by calibrating the signal (see section 3.1.6).

The probe excitation spectrum is a product of the frequency response of the probe and the spectrum of the RF pulse used to excite the spins (*pulse excitation spectrum*). The pulses used are sine waves modulated by top-hat functions, which give rise to pulse excitation spectra that are describable by sinc functions. Therefore in order to excite the spins as uniformly as possible about ν_0 , it is necessary to use short, high-power pulses. Pulse lengths were typically of duration 1–2 μ s.

3.1.5 Pulse sequences

The spin-lattice relaxation time T_1 is intimately dependent on the dynamical processes that occur throughout a sample. Therefore accurate measurement of T_1 as a function of temperature and magnetic field is key to elucidating the nature of the molecular motion that takes place.

Unlike measurements of the transverse relaxation time T_2 , there are no practical ‘one-shot’ pulse sequences possible for measuring T_1 in solids. Measurements of T_1 are inherently longer compared to measurements of T_2 . The most popular pulse sequences for measuring T_1 are the *saturation-recovery* and *inversion-recovery* sequences. Inversion-recovery is more suitable for samples with comparatively short T_1 (~ 0.1 s), and saturation-recovery is the most practical sequence for long T_1 values. The field-cycling magnet

allows for a third possible pulse sequence known as *polarisation-recovery*, which allows measurement of T_1 at low B -fields. It can also be used for samples of low mass and/or if the sample has a low concentration of the nuclei of interest. The saturation-recovery and polarisation-recovery pulse sequences were used for T_1 measurements in this thesis. The sequences are shown diagrammatically in figure 3.3.

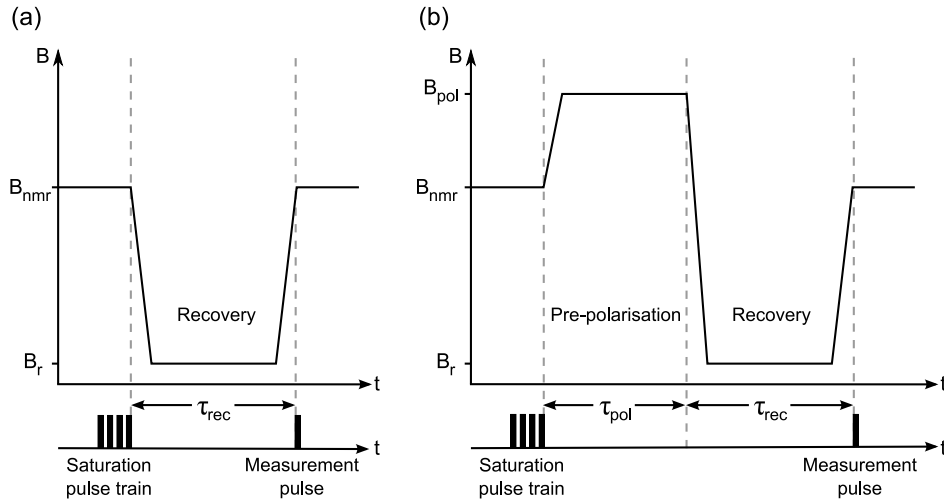


Figure 3.3: Schematic diagrams of the field-cycling pulse sequences. (a) Saturation-recovery sequence; (b) Polarisation-recovery sequence.

Pulse sequences for measuring T_1 all follow a similar routine. The first step is to manipulate the populations of the Zeeman levels so that the bulk magnetisation is in an easily reproducible initial state. The second step is to allow the populations to relax for some incremental delay time τ_{rec} . The final step is to measure the magnitude of the bulk magnetisation that has recovered during the interval τ_{rec} . These steps are repeated for a range of values of τ_{rec} , revealing the magnetisation relaxation curve.

For saturation-recovery, the initial state is *saturation* of the Zeeman levels, i.e. equalisation of the relative populations, resulting in zero bulk magnetisation. This is achieved by applying a series of 90° pulses (a so-called *pulse train*). Effective saturation is only possible if the delay between the pulses in the train are separated by a time greater than T_2 . Typical pulse trains of 12 pulses separated by 350ms were used. Saturation is carried out at field strength $B_{nmr} = \omega_{ref}/\gamma$, where $\omega_{ref}/2\pi$ is the frequency of the probe

circuit and spectrometer. Following saturation, the field is rapidly switched to the recovery field B_r and the magnetisation is allowed to recover for some time τ_{rec} . After the τ_{rec} delay, the field is switched back to B_{nmr} and a final pulse is applied to measure the recovered magnetisation M_z . Normally the incremented values of τ_{rec} form a geometric sequence, so that the relaxation curve is sampled at regular intervals along a plot of M_z versus $\ln(\tau_{\text{rec}})$. The sequence is determined by the VB program, based on the initial and final values of τ_{rec} specified by the user. The maximum value of τ_{rec} is required to be at least around ten times T_1 in order for the relaxation curve to reach M_0 .

The polarisation-recovery sequence is identical to saturation-recovery, however the former sequence has an additional polarisation step between saturation and recovery. After saturation the field is switched to some field $B_{\text{pol}} > B_r$, where the magnetisation is allowed to develop for a fixed time τ_{pol} . If B_{pol} and τ_{pol} are large enough, the dynamic range between the initial and equilibrium magnetisation values can be increased, compared to saturation-recovery. This pulse sequence was necessary for measuring T_1 at low field, i.e. $B_r < 0.1\text{T}$. Typical relaxation curves from saturation-recovery and polarisation-recovery measurements are presented in section 3.1.7.

Despite the capability of the magnet to switch at a rate of $10\text{T}\text{s}^{-1}$, the optimal values of field-switching rates were $8\text{T}\text{s}^{-1}$ for switching between B_{nmr} and B_r , and $5\text{T}\text{s}^{-1}$ for the reverse switch that occurs before the measurement pulse. A rate of $5\text{T}\text{s}^{-1}$ was quick enough to ensure measurement of T_1 of the order of hundreds of milliseconds, yet slow enough to minimise the field-overshoot that occurred after field-switching [52]. Overshooting can not be completely eliminated for any reasonable switching rate, however the effect is fairly reproducible for given initial and target fields. By applying an appropriate offset to the value of the target field, the strength of the field at the instance of acquisition can be such that it matches B_{nmr} . Appropriate values of the offset parameter for given initial and target fields were determined, and look-up tables were produced. The largest offset field used was 40 Gauss.

3.1.6 FID processing

Each FID collected underwent a series of processing steps in order to determine the magnitude of the recovered magnetisation. The data processing

steps were incorporated into the VB controlling program, and utilised some pre-written macros included with NTNMR.

The FIDs were baseline corrected to account for the DC offset, and the first few points were discarded (*'left shifted'*), in order to completely eliminate any remaining dead time signal and spurious points from the receiver switching on. The next step was to apply an *apodization* process, which reduced the contribution of stochastic noise to the NMR spectrum. The FID was multiplied by a monoexponential function $f(t) = \exp(-a.t)$, where a is a constant determined by the user. This is analogous to convolving the signal in the frequency domain (i.e. the NMR spectrum) with a Lorentzian function. The parameter a determines the width of the Lorentzian, and the extent to which the signal is attenuated. Finally the FIDs were Fourier transformed to give an NMR spectrum.

Phasing of the spectrum was necessary in order to separate out the absorptive and dispersive components of the spectrum, and this was also automated using a VB algorithm. The algorithm applied a series of phase shifts to the spectra and compared the integrated area under the left and right wings of the absorption spectrum. The absorption spectrum is completely absorptive when the sum of the areas under the wings is minimised. Finally, the magnitude of the recovered magnetisation was determined by integrating about the centre of the peak. The spectra were almost exclusively broad, single peaks. The spectra were dominated by dipolar broadening, and so very little, if any, structural information could be gained from the spectra.

The final stage of processing was to scale the integrated area under the absorption spectrum according to a 'calibration curve'. The non-uniform probe excitation spectrum causes the magnitude of absorption peaks to be frequency dependent. This has obvious implications for determining the recovered magnetisation from spectra that are collected off-resonance, due to the effects of rapid field-switching. The calibration curve, which is exactly analogous with the probe excitation spectrum (section 3.1.4), was determined by measuring the intensity of the absorption peak over a range of B_{nmr} field offsets (typically $\pm 50\text{G}$, in steps of 5G). The data were then fitted to a Lorentzian function which was then normalised (figure 3.4)). This process was carried out for each probe periodically, as small physical changes to the probe could cause a change in the frequency response.

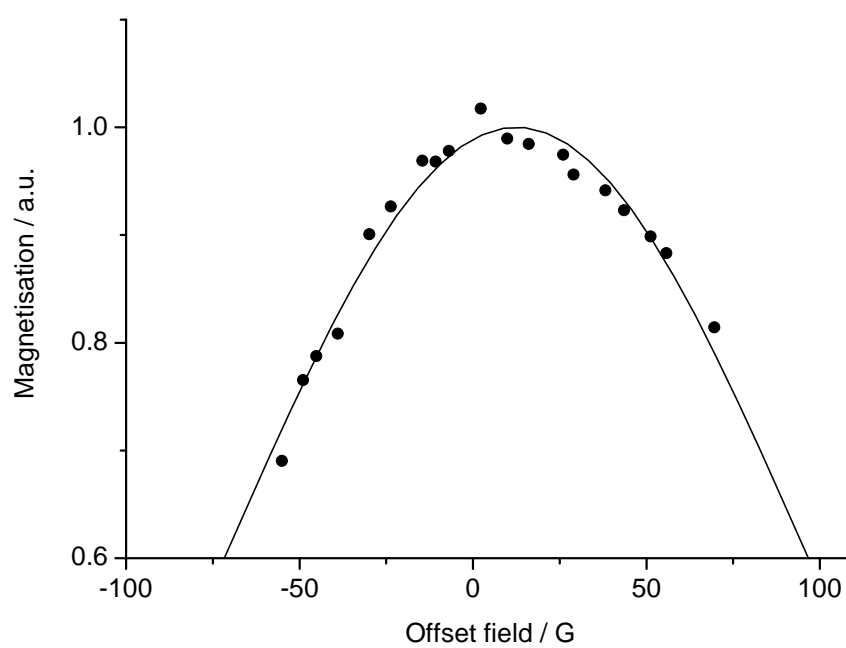


Figure 3.4: Probe excitation spectrum/calibration curve for 29.8MHz probe (solid line). Filled circles show integrated area under absorption peak for a range of B_{nmr} field offsets.

3.1.7 Data analysis

For each measurement of T_1 a magnetisation relaxation curve was collected, consisting of 15–50 points (i.e. 15–50 different values of τ_{rec}), depending on the length of T_1 and the shape of the relaxation curve.

A typical relaxation curve from a saturation-recovery measurement is presented in figure 3.5(a). The recovery of the magnetisation towards equilibrium is governed by an exponential growth equation $M_z(t) = M_0(1 - \exp(-t/T_1))$ (equation (2.36)), therefore relaxation curves from saturation-recovery measurements were fitted to the following expression;

$$y = a \left(1 - \exp \left(\frac{-\tau_{\text{rec}}}{T_1} \right) \right) + c . \quad (3.4)$$

M_0 is given by $a + c$. The fit parameter c is a baseline correction factor. The baseline region of the saturation curve (i.e. short τ_{rec}) may be non-zero due to imperfect saturation, and the recovery of magnetisation during field-switching. The latter effect is more significant for samples with short T_1 . The value of T_1 obtained from fitting remains unaffected by the non-zero baseline, so long as the dynamic range between the initial and equilibrium magnetisation was large. The same equation was used to fit recovery curves from polarisation-recovery measurements (figure 3.5(b)).

3.2 INS measurements

INS measurements were carried out using the IN4 time-of-flight (TOF) spectrometer at Institut Laue-Langevin (ILL), Grenoble, France [53]. The neutron source, namely the high-flux reactor (HFR), currently provides the most intense neutron flux of any reactor in the world[†]. High energy neutrons produced by the HFR are cooled by passing them through a moderator. Depending on the choice of moderating material, the peak of the Maxwellian distribution of neutron energy can be altered to a value appropriate to the spectrometer. IN4 is a thermal neutron spectrometer; neutrons are moderated by D₂O at 300K to give a peak at 1.2Å (56meV)[‡] in the Maxwellian

[†]The spallation neutron source (SNS) at Oak Ridge National Laboratory, Tennessee, USA is currently the most intense neutron source on Earth.

[‡]Wavelength $\lambda[\text{Å}]$ and energy $E[\text{meV}]$ of thermal neutrons are related by the expression $\lambda = 9.045 \frac{1}{\sqrt{E}}$.

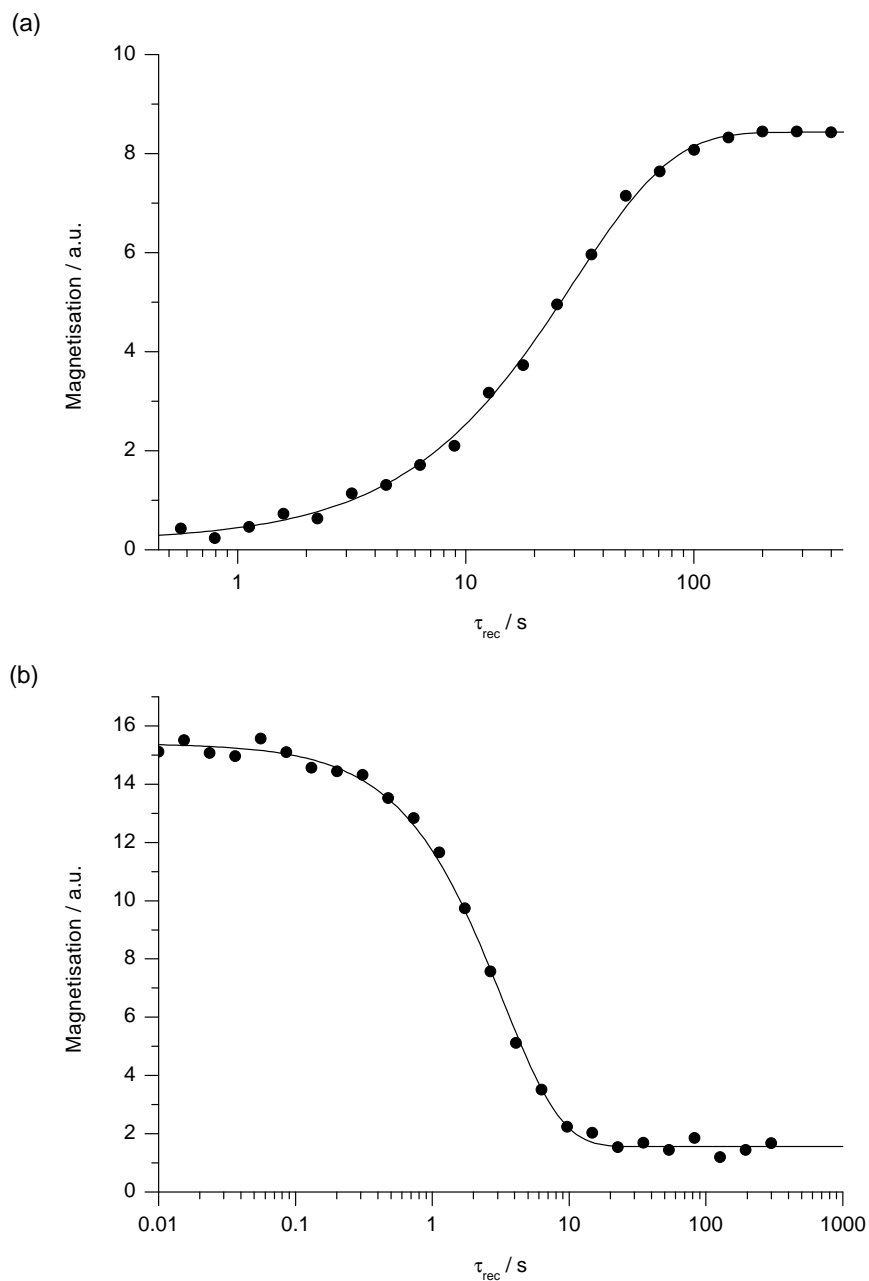


Figure 3.5: Examples of longitudinal magnetisation recovery curves from (a) saturation-recovery ($T_1 = 29.7 \pm 0.7\text{s}$) and (b) polarisation-recovery methods ($T_1 = 3.23 \pm 0.09\text{s}$). Solid lines are fits to equation (3.4).

distribution.

In general, neutron spectrometers consist of a primary spectrometer and a secondary spectrometer. The primary spectrometer selects neutrons of a particular energy from the broad energy distribution of the moderated beam—the secondary spectrometer analyzes the energy and momentum of the neutrons scattered by the sample, by measuring the neutron time-of-flight and the scattering angle, respectively.

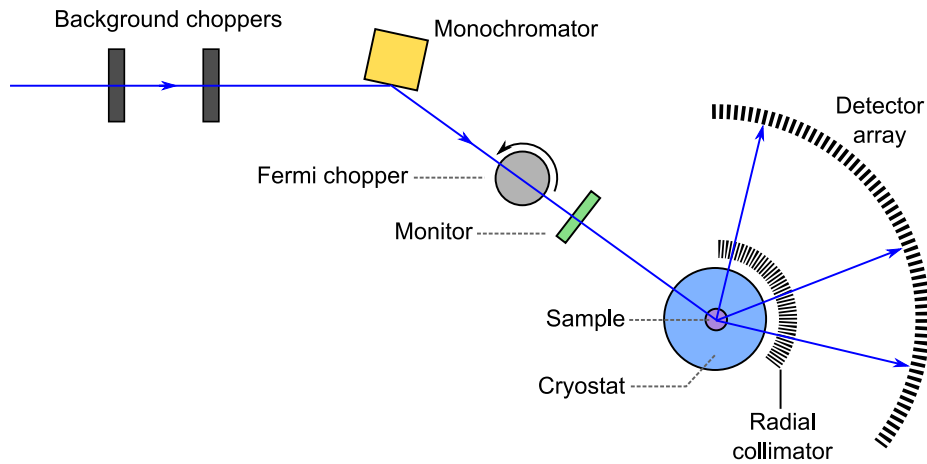


Figure 3.6: Schematic diagram of the IN4 TOF spectrometer, ILL, Grenoble.

3.2.1 Primary spectrometer

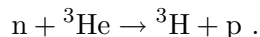
The main components of the primary spectrometer of IN4 are the background choppers, crystal monochromator, and Fermi chopper. The background choppers are rapidly-pulsating beam shutters that filter out high-energy neutrons and/or gamma rays, which would otherwise contribute to the background noise of the spectra. The required neutron energy is selected by a large-area crystal monochromator. The monochromator is made up of 55 pieces of crystal that form a double-curved surface. The curvature of the surface may be altered in the ‘vertical’ direction (i.e. perpendicular to the Bragg plane) and the ‘horizontal’ direction (in the Bragg plane) to give a neutron beam that is spatially focused at the sample position [54] (see section 3.2.3 for more detail). The Fermi chopper is a slit package that rotates about an axis perpendicular to the Bragg plane, and transmits short pulses

of neutrons (10–50 μ s). The frequency and the phase of the Fermi chopper is carefully set to be synchronous with the background choppers. By creating short, precisely controlled pulses of neutrons, the neutron time-of-flight may be accurately measured, which is crucial to determining the energy of the scattered neutrons.

3.2.2 Secondary spectrometer

The secondary spectrometer consists of a bank of 300 neutron detectors, covering scattering angles up to 120°, and a radial collimator, which minimises scattering from the sample environment. The sample environment can accommodate a variety of cryostats and furnaces. For the results presented in chapter 5, a standard ILL Orange cryostat was used, capable of routinely achieving temperatures between 2.5 and 300K.

Each element of the detector array is an aluminium tube filled with ^3He gas at a pressure of 6 bar. A gold-plated tungsten wire runs down the centre of the tube, and acts as an anode. Incident neutrons are absorbed by ^3He gas, causing the following reaction;



The recoil particles are detected via ionisation of the detector gas. The detectors are operated in proportional mode; the anode is kept at a sufficiently high voltage so that primary electrons created by the initial ionisation event have enough energy to create secondary electrons via further ionisation. The result is an amplification of the initial ionisation by an avalanche process, and a measurable electrical signal. The ^3He detectors are only useful for counting the number of incident neutrons, as they give very limited energy resolution. Energy discrimination of the neutrons is achieved via measuring the neutron time-of-flight.

Figure 3.7 shows an example of data collected from a TOF spectrometer. The data is presented as a surface plot of neutron intensity plotted against scattering angle and channel number of the digital acquisition card. The intensity is normalised to the average neutron intensity measured by the monitor (a neutron counter with high transmission, placed between the Fermi chopper and sample). This corrects for the fact that the neutron flux may vary over time, and allows direct comparison of spectra collected at

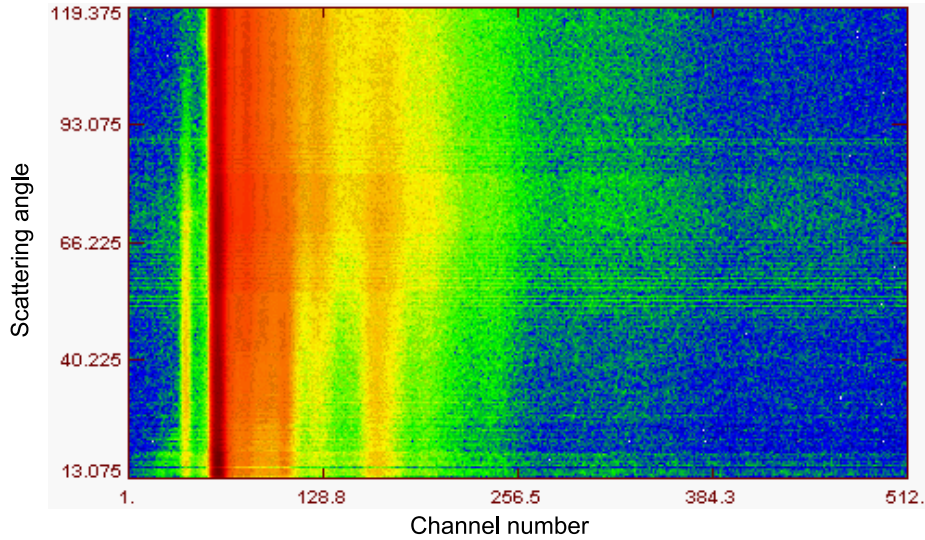


Figure 3.7: Example of INS data acquired from IN4 TOF spectrometer, presented as a surface plot. The colours denote the intensity of scattered neutrons detected; blue corresponds to low intensity, and red corresponds to high neutron intensity. Scattering angle is plotted along the vertical direction, and in the horizontal direction channel number is plotted (channel number is proportional to time-of-flight). Scattering angle and time-of-flight may be converted into momentum transfer Q and energy transfer ω , respectively.

different times. The peak due to elastic collisions (the ‘*elastic peak*’) can be easily identified as the deep red area at around channel 60. Such data can be processed and presented in numerous ways. Most often the neutron intensity is summed across the range of detectors (i.e. along the y direction), and presented as a plot of $S(Q, \omega)$ vs. ω , which gives the excitation spectrum of the sample. Alternatively, at a particular energy range of interest, the neutron intensity can be plotted as a function of scattering angle to give a plot of $S(Q, \omega)$ vs. Q . These latter plots can give spatial information about motional processes.

Transformation from channel number to time-of-flight t_F is a straightforward process as the channel width is a known quantity. The transformation from time-of-flight to energy is also simple, provided that the length of the neutron flight path L_F is accurately known;

$$\begin{aligned} E_k &= \frac{1}{2}m_n v^2 \\ v &= \frac{L_F}{t_F} . \end{aligned} \quad (3.5)$$

3.2.3 Time-focused INS

IN4 utilises a doubly curved monochromator in order to maximise the neutron flux incident on the sample, and to ensure that the neutron beam is spatially focused [54]. However initial gains in neutron intensity are offset by loss in energy resolution, due to the increased width of the wavelength distribution $\Delta\lambda_0$. Figure 3.8(a) shows how the wavelength distribution comes to be. The curved monochromator is approximated as three flat crystal

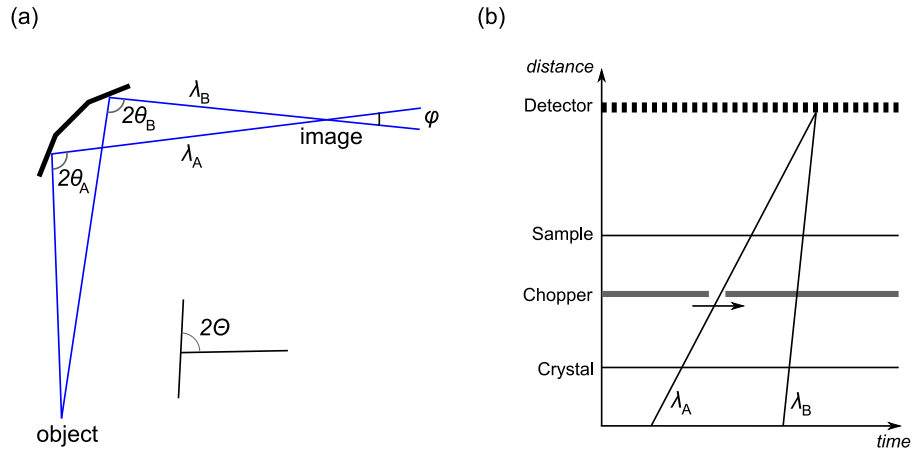


Figure 3.8: (a) The curvature of a curved monochromator (here approximated by three flat surfaces) causes a range of neutron wavelengths $\Delta\lambda_0$ to be focused at the image point; (b) By appropriately setting the sense and frequency of rotation of the chopper, slower neutrons (λ_A) can be transmitted before faster neutrons (λ_B), therefore achieving both time and spatial focusing at the detector.

elements at different relative orientations. These present a range of Bragg angles for the polychromatic neutron source (*‘object’*), which results in λ_A being larger than λ_B . Neutrons of wavelength λ_A are slower than those of wavelength λ_B , and the difference in their flight time over some general distance L is given by [55]

$$\Delta\tau = CL \cdot 2d \cos \Theta \cdot \frac{\phi}{2}, \quad (3.6)$$

where d is the interplanar distance of the crystal, and C is a constant that relates the speed of a thermal neutron to its wavelength ($C = 252.77\mu\text{s} \cdot \text{m}^{-1}\text{\AA}^{-1}$).

Time-focusing involves rotating the Fermi chopper at a particular frequency and sense of rotation so that the beams of different wavelengths arrive at the detector at the same time. The resulting energy resolution is frequency dependent and is described by a *resolution function*. Time-focusing improves the energy resolution in a selected region of the spectrum, however the downside is that resolution away from this region can be poor.

The sense of rotation of the Fermi chopper is set so that the ‘A’ beam is allowed through some time Δt before the ‘B’ beam, where Δt is given by

$$\Delta t = \frac{\phi}{2\pi\nu} . \quad (3.7)$$

ν is the frequency of rotation. Equating equations (3.6) and (3.7) gives the condition for the appropriate value of ν to achieve time focusing of the beams at the detector;

$$2\pi\nu = (L_{\text{FD}}C \cdot d \cos \Theta)^{-1} , \quad (3.8)$$

where L_{FD} is the distance from the chopper to the detector.

3.2.4 Spectrometer configurations

The resolution and width of an INS spectrum are both dependent on the wavelength of the thermal neutrons λ_0 . Longer wavelengths increase the spectral resolution, however shorter wavelengths enable spectra to be measured over wider energy ranges but at lower resolution; there is a trade-off between resolution and spectrum width.

An appropriate value of λ_0 is chosen based on the desired resolution and spectrum width. Also the time-focusing parameters can be set accordingly in order to maximise the resolution in the region of interest. Table 3.3 shows the specifications of IN4 in the various configurations that were employed.

$\lambda_0/\text{\AA}$	Monochromator	$\Delta\hbar\omega_{\text{El}}/\text{meV}$	$(\hbar\omega)_{\text{min}}/\text{meV}$	$(\hbar\omega)_{\text{max}}/\text{meV}$
1.24	Cu 220	2.75	-54	48
1.8	Cu 111	1.08	-24	22
3.6	PG 022	0.24	-36	5

Table 3.3: Performance specifications of IN4 in the configurations used for the measurements presented in chapter 5. $\Delta\hbar\omega_{\text{El}}$ denotes the FWHM of the elastic line; PG—*pyrolytic graphite*.

The $\lambda_0 = 1.8\text{\AA}$ configuration was used to maximise resolution in the energy range 12–20meV on the neutron energy lost side ($\Delta\hbar\omega = 0.83\text{meV}$ FWHM). The $\lambda_0 = 3.6\text{\AA}$ configuration was used to study this same energy window on the neutron energy gained side of the spectrum, and the resolution in the region of interest was 1.3meV FWHM.

Chapter 4

Rotational dynamics of guest methyl groups in calixarene supramolecular complexes

The cavity of a calixarene molecule provides an environment which smaller guest molecules may occupy, via non-covalent bonding. It has been shown that for some methyl-substituted aromatic compounds incarcerated in calixarene host-guest complexes, the rotation of the guest methyl groups is hindered by a very low potential barrier. Low-temperature INS measurements on such complexes by Caciuffo and co-workers have shown that the rotation of the methyl groups approaches the quantum free-rotor limit [56].

NMR relaxometry measurements were performed on a variety of calixarene host-guest molecules. Temperature dependent measurements of T_1 were carried out on all of the samples in order to assess their suitability as candidates for cryorelaxors in cryoMAS NMR. Several of the complexes were studied in greater detail, by measuring the dispersion of the relaxation rate via field-cycling NMR, in order to characterise the methyl-group rotational potentials. The effect of deuteration of the host complex on the efficiency of proton spin-lattice relaxation is also explored.

4.1 Calixarene samples

Calixarenes are oligomeric molecules, i.e. they comprise a limited number of monomer units (as opposed to a polymer which has no limit to the num-

ber of repeat units). Phenolic molecules are used as the monomers from which calixarenes are formed. The samples studied in this thesis were based on one of two calixarenes, namely *p-tert*-butylcalix[4]arene (figure 4.1(b)) and *p*-isopropylcalix[4]arene (figure 4.1(d)). The monomer units of these

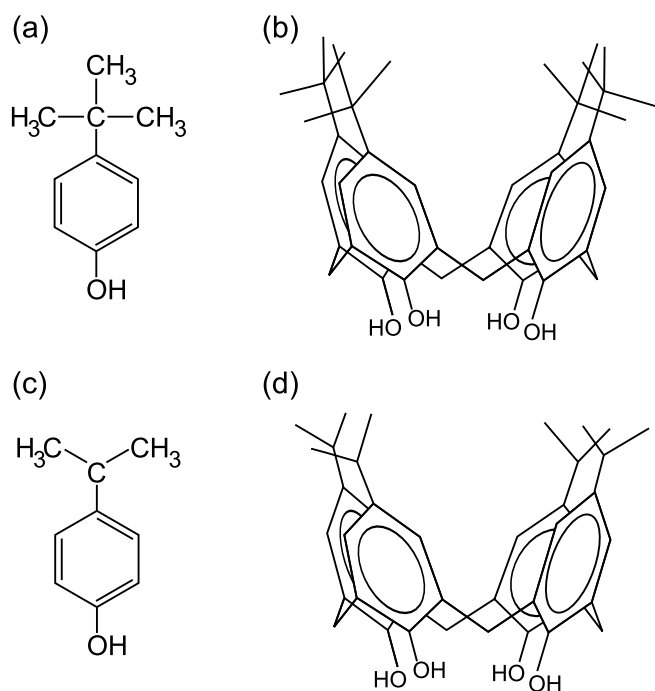


Figure 4.1: Chemical structure of (a) *p-tert*-butylphenol (b) *p-tert*-butylcalix[4]arene (c) *p*-isopropylphenol and (d) *p*-isopropylcalix[4]arene.

calixarenes are *p-tert*-butylphenol (figure 4.1(a)) and *p*-isopropylphenol (figure 4.1(c)), respectively. In the calixarene naming system, the number in brackets denotes the number of monomer units.

In calixarene molecules the phenol molecules are bridged by methylene groups ($-\text{CH}_2-$), which link the units to form the characteristic bowl shape. The bowl has four-fold symmetry, and the shape is maintained by a cyclic network of 4 hydrogen bonds located at the ‘base’ of the bowl. The tertiary butyl or isopropyl groups line the edge of the ‘upper’ rim.

All of the calixarene-based samples studied in this thesis (table 4.1) were synthesized by our collaborators at the University of Southampton School of Chemistry. All samples were in powder form.

With the exception of sample **XI**, the samples were host-guest inclusion complexes comprising calixarene host molecules and guest molecules that

Sample No.	Host molecule	Guest molecule
I	<i>p-tert</i> -butylcalix[4]arene	toluene
II		γ -picoline
III		chlorotoluene
IV		fluorotoluene
V		4-methylanisole
VI		acetone
VII	<i>p</i> -isopropylcalix[4]arene	<i>p</i> -xylene
VIII		iodomethane
IX		2-butyne
X	<i>p-tert</i> -butylcalix[4]arene-tetracarbonate	nitromethane
XI	<i>p-tert</i> -butyl[(Methyl-toluene-2, ... 6-diacetamide)dihydroxy]calix[4]arene	N/A

Table 4.1: List of calixarene host-guest complexes studied. The chemical structures of the guest molecules are shown on the corresponding plots of T_1 versus inverse temperature (section 4.7. All complexes were of (1 : 1) co-ordination with the exception of samples **VII** and **XI**. Complex **VII** comprises two calixarene molecules enclosing a single *p*-xylene molecule.

had at least one methyl group in their structure. Sample **XI** was a *p-tert*-butylcalix[4]arene molecule with an additional ‘bridge’ between two of the hydroxyl oxygen atoms (figure 4.2(b)). Part of the bridge was a toluene molecule, complete with a single methyl group. The host molecule of sample **X** was also adapted from *p-tert*-butylcalix[4]arene. The 4 hydroxyl groups were substituted with carbonate groups to form *p-tert*-butylcalix[4]arene-tetracarbonate.

4.2 Effect of thermal history on T_1

Upon measuring the temperature dependence of T_1 in the calixarene samples it became clear that, in most cases, the thermal treatment of the samples had an effect on the relaxation of the proton magnetisation. In order to study this effect more closely, several of the samples were subjected to different thermal treatments, and the temperature dependence of T_1 was measured and compared. The two thermal treatments were as follows; ‘*quench-cooling*’ involved quickly cooling the sample from room temperature to cryogenic temperatures, and ‘*annealed*’ samples were prepared by slowly cooling the samples from room temperature.

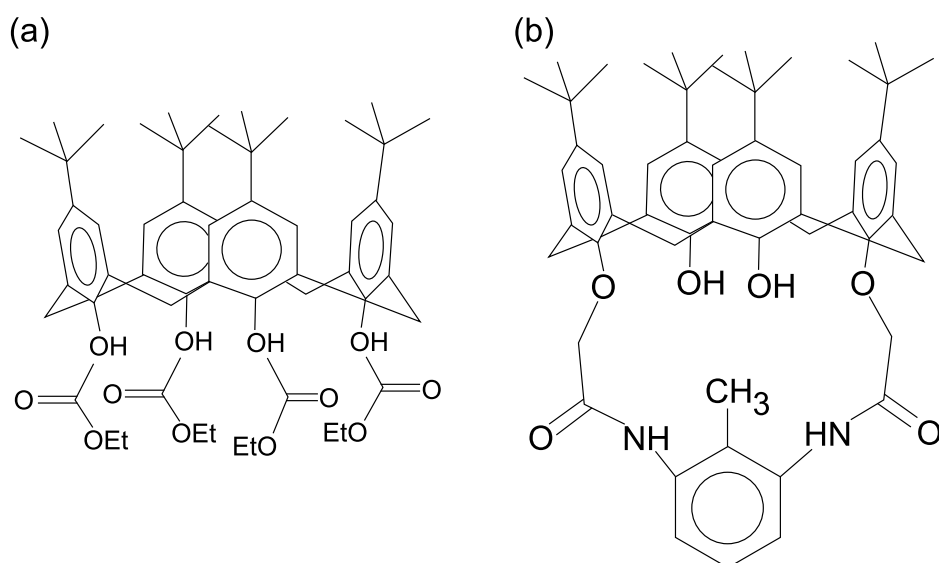


Figure 4.2: Chemical structures of adapted calixarene molecules. (a) host molecule for sample **X**. Ethyl carbonate groups are substituted at the hydroxyl positions of the calixarene bowl (ethyl groups $-\text{CH}_2\text{CH}_3$) are represented by the symbol ‘Et’); (b) sample **XI**.

Samples were quench cooled by inserting the loaded NMR probe into a cold cryostat and then pumping the sample space to maximise helium gas flow over the sample, until the sample reached the desired low temperature. Loading the probe into the cold cryostat could cause the sample temperature to drop as low as 220K within a few seconds. By pumping the cryostat, cooling rates of 15K min^{-1} were typical.

Samples were annealed by slowly cooling from room temperature at a controlled rate. This was achieved by using the temperature ramp feature on the Lakeshore temperature controller. Temperature ramps of -0.3K min^{-1} were typical.

In general the T_1 values measured for samples that were quickly cooled from room temperature to cryogenic temperatures (*‘quench-cooled’*) were smaller than for samples that were slowly cooled (*‘annealed’*). This effect was observed in samples **I–IV**, and the most dramatic example of this behaviour was observed in sample **VII** (figure 4.4). The results from relaxation measurements from this sample are described in detail in the following section.

4.3 Rotation of *p*-xylene methyl groups in a calixarene host-guest complex

In this section, results from measurements of the temperature dependence of T_1 in quench cooled and annealed samples of a calixarene/*p*-xylene complex are presented. The annealed sample was analysed further by measuring the temperature dependence of T_1 at several relaxation fields, and by measuring the dispersion of T_1 over a range of low temperatures (i.e 5.4–9.1K).

4.3.1 Structure

The *p*-xylene/calixarene complex studied (sample **VII**) was a 2 : 1 complex of *p*-isopropylcalix[4]arene and *p*-xylene. The x-ray crystal structure of sample **VII** (Fig.4.3) shows that the calixarene molecules are arranged so that their cavities are facing each other, and the *p*-xylene molecule sits in the closed cavity formed by the calixarene molecules [46].

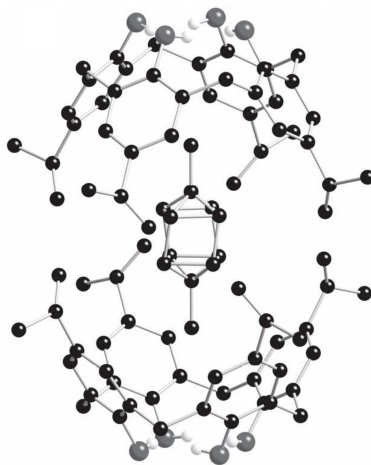


Figure 4.3: Crystal structure of sample **VII**, *p*-xylene guest [46].

4.3.2 Thermal history effects

In figure 4.4 the temperature dependence of T_1 in sample **VII** is presented for both annealed and quench cooled preparations. At temperatures below 50K, T_1 values measured in the annealed sample of complex **VII** are larger than T_1 measured in the quenched sample by a factor of between 20 and

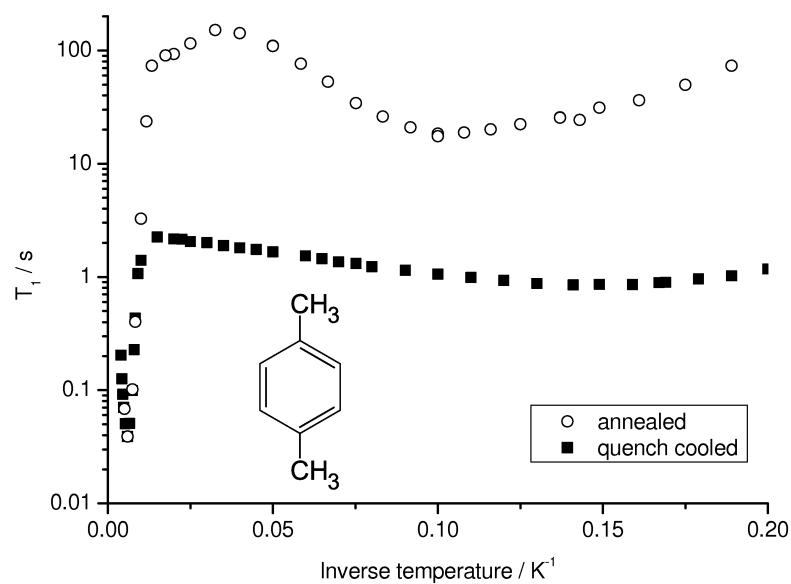


Figure 4.4: Temperature dependence of T_1 in sample **VII**, *p*-xylene guest, $B_r = 0.7T$ (probe **A**, constant field). T_1 values for annealed sample include relaxation times determined by fitting relaxation curves to either the monoexponential or biexponential relaxation expressions, where appropriate; in the case of biexponential relaxation, only the dominant T_1 value is plotted. Error bars are small compared to marker size.

80. The minima at low temperatures are caused by the rotational motion of the weakly hindered methyl groups that belong to the guest *p*-xylene molecule. At temperatures above 50K the T_1 versus inverse temperature curves change with a very steep gradient ($\sim 1100\text{K}$), and the values converge for both annealed and quench cooled samples. The curves pass through a minimum point at 167K ($5.99 \times 10^{-3}\text{K}^{-1}$). This feature is caused by the strongly hindered methyl groups belonging to the iso-propyl groups of the calixarene host. This feature consistently appeared in the temperature dependent measurements performed on all of the calixarene samples studied. Relaxation at low temperatures was primarily dictated by the rotation of the guest methyl groups, therefore measurements were concentrated in the low temperature region, for all samples.

The dependence of T_1 on the thermal history has been interpreted as being reflective of the level of disorder present in the sample after the thermal treatment. Slowly cooling the samples allow the constituent molecules to explore the potential energy surface and settle into the minimum energy orientation; conversely, quench cooling freezes in any disorder that may be present at room temperature. The fast relaxation times in the quench cooled sample indicate the presence of very efficient relaxation sinks, which are most likely to be weakly hindered, highly mobile molecules or moieties.

Apart from affecting the value of T_1 , the thermal history also had an affect on the shape of the relaxation curve. After quench cooling and the initial annealing treatment, the relaxation in sample **VII** was *monoexponential*, i.e. the relaxation curve could be characterised by equation (3.4) and a single relaxation time. However after some slow-cooling treatments the relaxation curves could not be satisfactorily described by monoexponential relaxation and it was necessary to fit the relaxation curves to the expression

$$M(t) = M_0^{(a)} \left(1 - \exp \left(\frac{-t}{T_1^a} \right) \right) + M_0^{(b)} \left(1 - \exp \left(\frac{-t}{T_1^b} \right) \right). \quad (4.1)$$

This expression describes *biexponential* relaxation. The protons in the sample are effectively separated into two groups, distinguishable by their relaxation times. The relaxation time of protons in a sample is dependent on the environment of the proton; different environments will cause the protons to have different relaxation times. Even in the case of monoexponential recovery curves, the observed value of the relaxation rate T_1^{-1} is a weighted value

of the different proton relaxation rates in the sample. If there is inadequate spin diffusion between protons belonging to different environments, the T_1 values remain distinct and manifest themselves in the profile of the relaxation. The amplitude parameters $M_0^{(a)}$ and $M_0^{(b)}$ are proportional to the relative number of protons in each environment. There is no upper limit to the number of different relaxation components that may manifest themselves in the relaxation curve. For relaxation curves displaying more than two relaxation components it is not possible to accurately determine each component, however estimates of particular components may be possible.

In figure 4.5 an example of a biexponential relaxation curve for **VII** is presented. The two relaxation components differed by an order of magni-

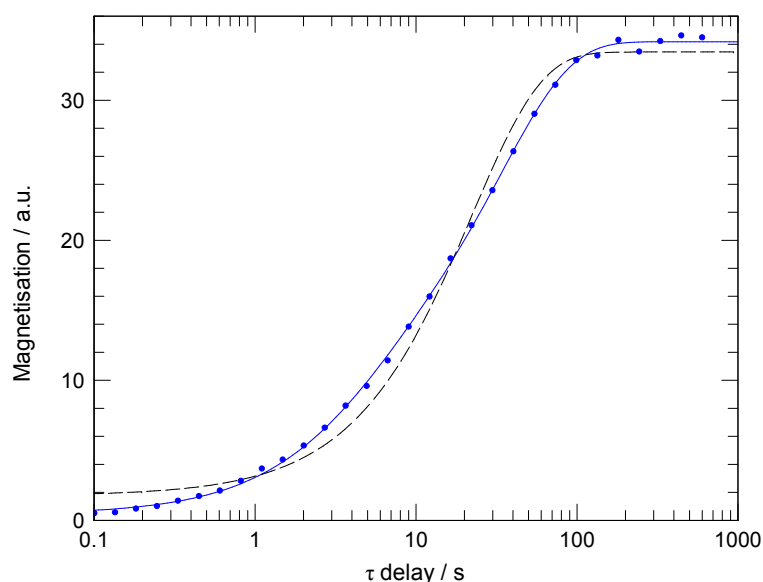


Figure 4.5: Magnetisation relaxation curve for partially annealed sample of complex **VII** (*p*-xylene guest), $B_r = 0.7\text{T}$. Relaxation displays bi-exponential character, with time constants $T_1 = 34$ and 3.9s . The dashed line shows the poor agreement with mono-exponential recovery.

tude, and could therefore be separated and measured fairly accurately. The long component of the relaxation curves dominated, and was similar to the relaxation time measured from the monoexponential relaxation curves of the annealed sample, therefore only this relaxation time was considered. The biexponential behaviour was attributed to partial annealing of the sample

and a multi-phase sample developing after temperature cycling.

4.3.3 Methyl group dynamics in an annealed sample

The difference in T_1 values between quench cooled and annealed samples has been attributed to the level of disorder present in the sample. The potential barriers of guest methyl-groups are more likely to be determined in the well ordered, annealed samples, as there is a limit to the number of distinct environments that can be separated from NMR relaxometry measurements, as shall be demonstrated in the following sections.

The temperature dependence of T_1 was measured at three different relaxation fields in an annealed sample of complex **VII** (Fig.4.6). The T_1 -inverse temperature curves display T_1 minima at low temperature, indicating the presence of weakly hindered methyl groups in the annealed sample. The T_1 values measured at higher fields converge at high temperatures as the methyl-group rotation enters the fast motion regime, however the low field values do not.

More information regarding the dynamic processes that drive the proton relaxation at low temperatures can be obtained by making high-resolution frequency-dependent measurements of the relaxation rate. This reveals the spectral density function of the fluctuating dipolar interaction, from which the correlation rate of the methyl-group can be measured.

For sample **VII**, the frequency dependence of T_1 was measured at six different temperatures between 5.4K and 9.1K. The resulting spectral density functions are displayed in figure 4.7. Fitting the curves to a single component gave unsatisfactory results. Better fitting was achieved by assuming the presence of two components. The data were fitted to the following expression;

$$T_1^{-1}(B_r) = C_{EE}^{(1)} \sum_{m=1}^2 \frac{m^2 \tau_{c1}}{1 + m^2 \gamma^2 B_r^2 \tau_{c1}^2} + C_{EE}^{(2)} \sum_{m=1}^2 \frac{m^2 \tau_{c2}}{1 + m^2 \gamma^2 B_r^2 \tau_{c2}^2}. \quad (4.2)$$

The fit parameters are the dipolar coupling constants, $C_{EE}^{(1)}$ and $C_{EE}^{(2)}$, and the correlation rates, τ_{c1}^{-1} and τ_{c2}^{-1} . In the frequency region explored here, the tunnelling frequency was found to make a negligible contribution to the

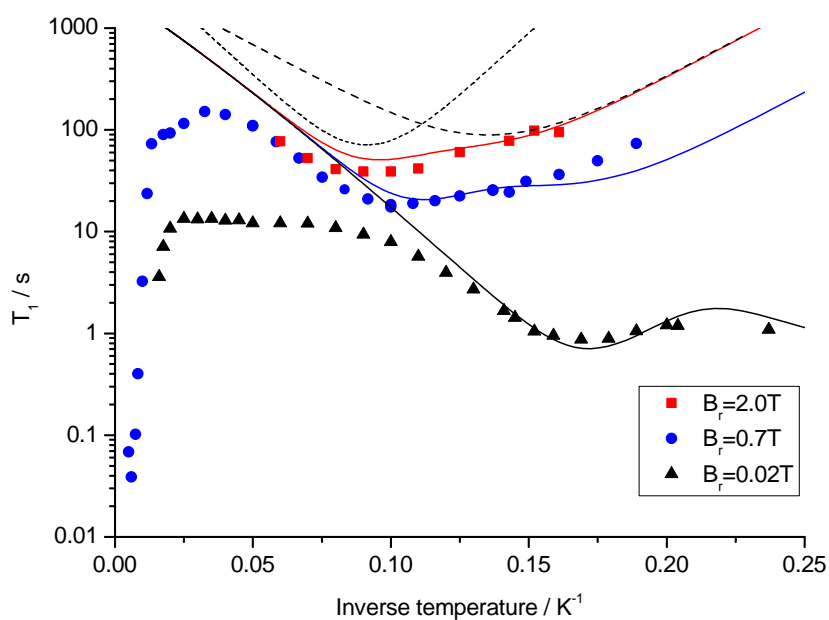


Figure 4.6: T_1 versus inverse temperature, sample **VII** (*p*-xylene guest), annealed. T_1 measured at three different relaxation fields, $B_r = 0.02, 0.7$ and 2.0T (probe **A**). Error bars are small compared to marker size. Solid lines are calculated based on BPP relaxation model and two distinct methyl group environments. Dashed lines show the individual contribution of each distinct methyl-group environment, calculated for $B_r = 2.0\text{T}$.

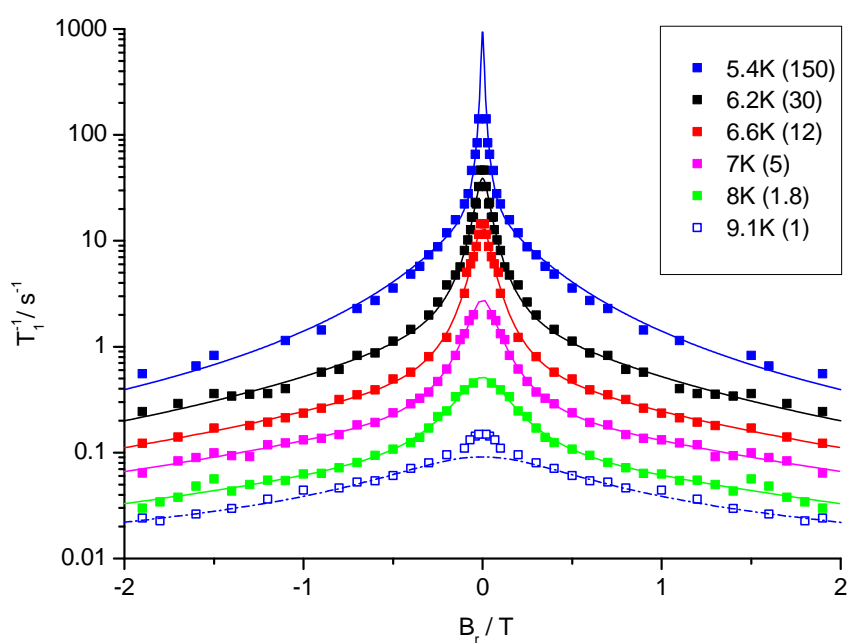


Figure 4.7: Dispersion of T_1^{-1} in annealed sample of complex **VII** (*p*-xylene guest), $T = 5.4$ – 9.1 K. For clarity, the curves have been offset by the scale factor given in brackets. Data points have been reflected about $B_r = 0$ in order to accentuate the Lorentzian nature of the spectral density functions. Solid lines are fits to expression (4.2).

relaxation; consequently, tunnelling terms (the AE terms in equation (2.57)) have not been included in the fit.

By fitting the data to equation (4.2), unconstrained fits provided good accounts of the spectral density functions (with the exception of the $T = 9.1\text{K}$ data; see below). The average values of the dipolar coupling constants were found to be $\overline{C_{EE}^{(1)}} = (4 \pm 1) \times 10^6 \text{s}^{-2}$ and $\overline{C_{EE}^{(2)}} = (5 \pm 1) \times 10^6 \text{s}^{-2}$.

The two components observed in the spectral density functions have been interpreted as being due to two different methyl-group environments, each with a distinct correlation rate τ_c^{-1} . In figure 4.8 the two correlation rates measured by fitting the spectral density functions are plotted as a function of inverse temperature. The solid lines are fits to the Arrhenius rate law

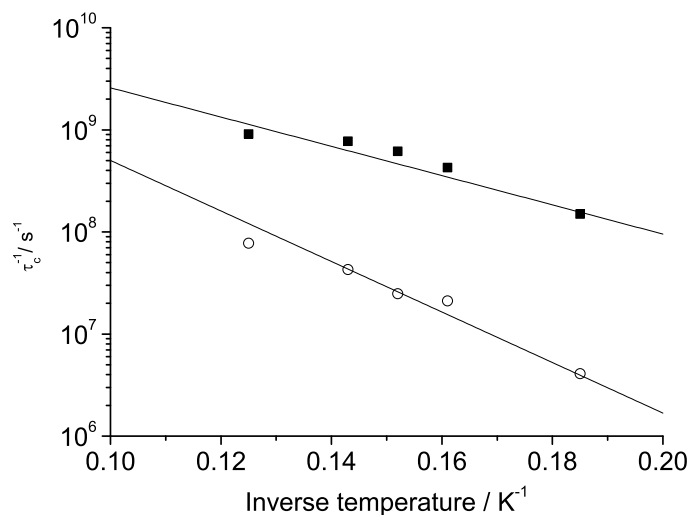


Figure 4.8: Plot of τ_c^{-1} as a function of inverse temperature, sample **VII** (*p*-xylene guest), annealed. Black squares and white circles correspond to the broad and narrow components of the spectral density functions, respectively. Solid lines shown are fits to the Arrhenius rate law; measured activation energy parameters are $E_a^{(1)} = 33 \pm 3\text{K}$ and $E_a^{(2)} = 57 \pm 3\text{K}$. Error bars are small compared to marker size.

(equation (2.58)). From the fits, it is clear that of the correlation rates of the methyl groups closely follow the Arrhenius law. The respective gradients of the lines of best fit measure the torsional splitting E_{01} of each distinct methyl environment, and these values have been used in order to estimate the magnitude of the potential barriers. The fit parameters, and resulting estimates of the barriers are listed in table 4.2 (calculation of barrier height

assumed a purely threefold potential). As mentioned in section 2.3.2, E_{01} is the difference in energy between the E -symmetry states in the ground and first excited torsional states. It is appropriate to identify this as the activation energy as the difference in energy between A -symmetry states in the ground and the first excited torsional states is significantly larger than the energy difference between the E -symmetry states, and the process of conversion between states of E and A -symmetry is spin-restricted.

Component	$\overline{C_{EE}} / \text{s}^{-2}$	$\tau_0^{-1} / \text{s}^{-1}$	E_{01}/K	V_3/K	$\nu_t^{(0)}/\text{meV}$
(1) Broad	$(4 \pm 1) \times 10^6$	7.0×10^{10}	33 ± 3	47 ± 9	0.46 ± 0.04
(2) Narrow	$(5 \pm 1) \times 10^6$	1.5×10^{11}	57 ± 3	107 ± 8	0.20 ± 0.03

Table 4.2: Fit parameters and calculated barrier heights and ground state tunnel splitting for methyl groups in sample **VII** (*p*-xylene guest), annealed.

The field-dependent T_1^{-1} data for $T = 9.1\text{K}$ provided an unsatisfactory fit when attempting an unconstrained fit to equation 4.2. This is due to the observed components broadening into regions beyond our experimental window, making unconstrained fitting unstable and unreliable. The appearance of another narrow spectral density component at this temperature also makes fitting complicated. The dashed line shown in figure 4.7 is based on values of τ_c extrapolated from figure 4.8. The model appears to be consistent with the data above $B_r = 0.3\text{T}$.

Further evidence in support of the model of the dynamics comes from comparing the model with the temperature dependence of T_1 at fixed field. In figure 4.6 the solid lines correspond to the values of T_1 computed using a BPP model of relaxation, with two inequivalent methyl group environments, characterised by the parameters in table 4.2. The computed behaviour agrees very well with the experimental data at temperatures below 10K. Above this temperature the experimental points deviate away from the model, especially at low field. This reveals the presence of an additional motional process, which is relatively slow and has a narrow spectral density component at low temperature. It is likely that the additional narrow feature observed in the field dependent data measured at 9.1K is associated with this motional process, the exact nature of which is still undetermined.

4.4 Rotation of toluene methyl groups in a calixarene host-guest complex

Sample **I** was a (1 : 1) complex of toluene and *p*-*tert*-butylcalix[4]arene. Toluene is a benzene molecule with one methyl-group substituent. In complex **I** the C–CH₃ bond of the toluene molecule is aligned along the axis of four-fold symmetry of the calixarene molecule (figure 4.9). X-ray crys-

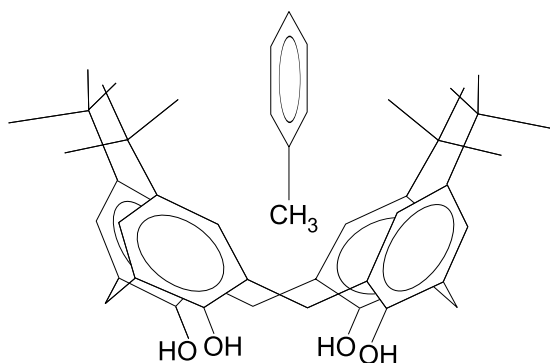


Figure 4.9: Sketch of calixarene complex, sample **I**.

tal diffraction measurements (XRD), carried out by our collaborators at the University of Southampton, revealed two-fold dynamic disorder of the toluene molecule in the calixarene cavity.

4.4.1 Thermal history effects

T_1 was measured as a function of temperature at $B_r = 0.7T$, in quench cooled and annealed samples of complex **I** using probe **C**. T_1 was observed to be monoexponential for both annealed and quench cooled samples, however T_1 was dependent on the thermal history of the sample. The T_1 -inverse temperature curve for the quenched sample (figure 4.10) clearly displays a very shallow T_1 minimum at $\theta_{\min} = 7.7\text{K}$ (0.13K^{-1}). The curve for the annealed sample has two apparent minima at $\theta_{\min} = 9.1$ and 5.2K (0.11 and 0.19K^{-1} , respectively), suggesting the presence of inequivalent methyl groups, which are weakly hindered. The difference in T_1 values observed between the two thermal preparations is not as dramatic as the difference seen in sample **VII**; the values differ by a factor of 2.5 at most, compared

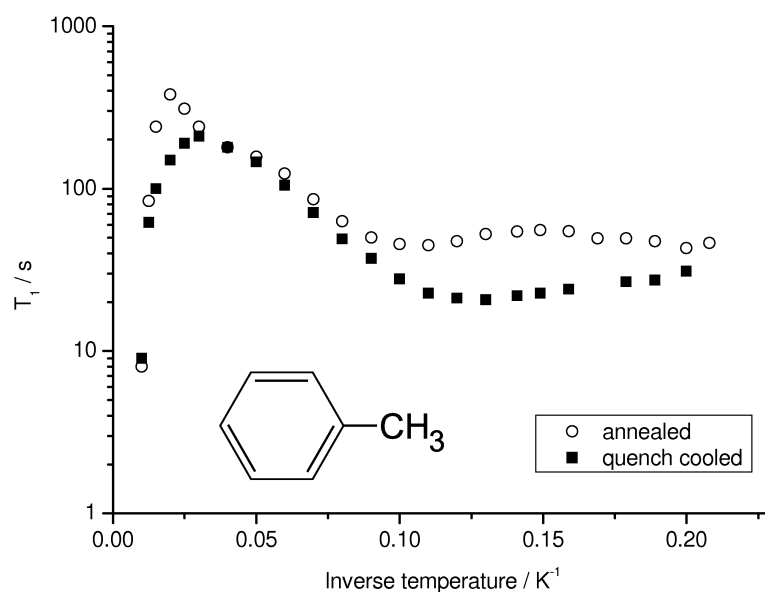


Figure 4.10: Temperature dependence of T_1 , sample I (toluene guest), $B_r = 0.7\text{T}$ (probe C, field-cycling). Error bars are small compared to marker size.

to a factor of 80 in the *p*-xylene complex.

4.4.2 Methyl-group dynamics in an annealed sample

The temperature dependence of T_1 in the annealed sample was measured at three different relaxation fields; the T_1 -inverse temperature curves are presented in figure 4.11. The $B_r = 0.7$ and 2.0T curves display two T_1 minima. At low field, the minima are expected to appear at lower temperature and at shorter values of T_1 . The 0.025T curve displays a single T_1 minimum, which corresponds to the minimum observed at higher temperature for $B_r \geq 0.7\text{T}$. At 0.025T , the other T_1 minimum is apparently shifted to a temperature beyond the minimum temperature accessible by the experimental apparatus.

The reproducibility of the T_1 measurements was checked by cooling the sample to low temperature after the initial temperature sweep was completed, and repeating measurements at low temperature. The repeated measurements of T_1 at 0.025T and 2.0T were in good agreement with the values measured from the initial run, however a difference was observed in the measurements performed at $B_r = 0.7\text{T}$ (open circles, Fig.4.11). The T_1 curve of the measurements repeated at 0.7T converges with the 2.0T curve

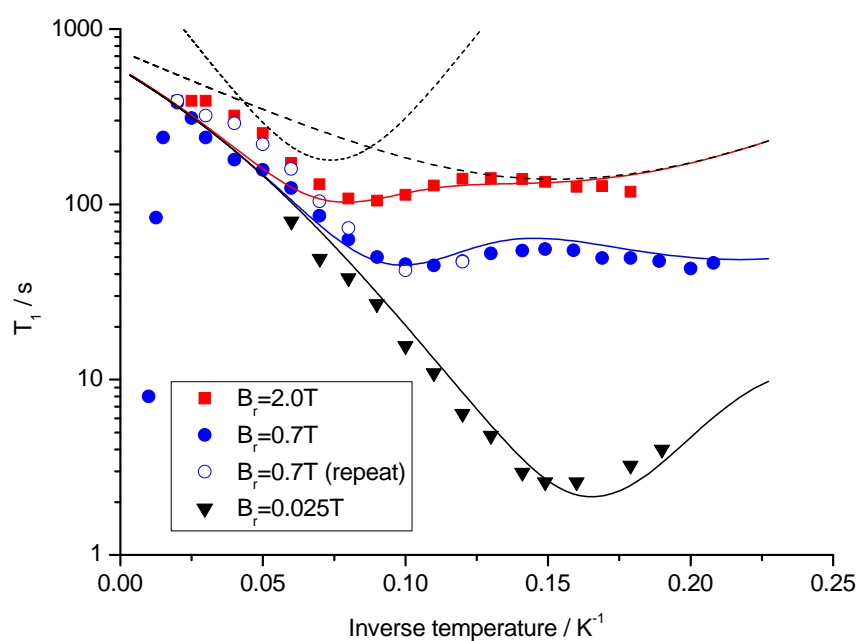


Figure 4.11: T_1 versus inverse temperature measured at a range of magnetic field strengths in annealed sample of complex **I** (toluene guest), measured using probe **C**. Error bars are small compared to marker size. Solid lines are computed from BPP model and parameters in table 4.3. Dashed lines show the individual contribution of each distinct methyl-group environment, calculated for $B_r = 2.0T$.

at high temperature, as is expected for a methyl group in the fast rotation limit. The difference in T_1 values after cycling from high to low temperatures suggests that the sample was only partially annealed during the initial measurements (filled circles, Fig.4.11).

The dispersion of T_1 was measured at four different temperatures between $T = 5.3$ – 10 K, and the resulting T_1^{-1} versus B_r curves are presented in figure 4.12. As observed in the *p*-xylene complex (**VII**), the spectral density

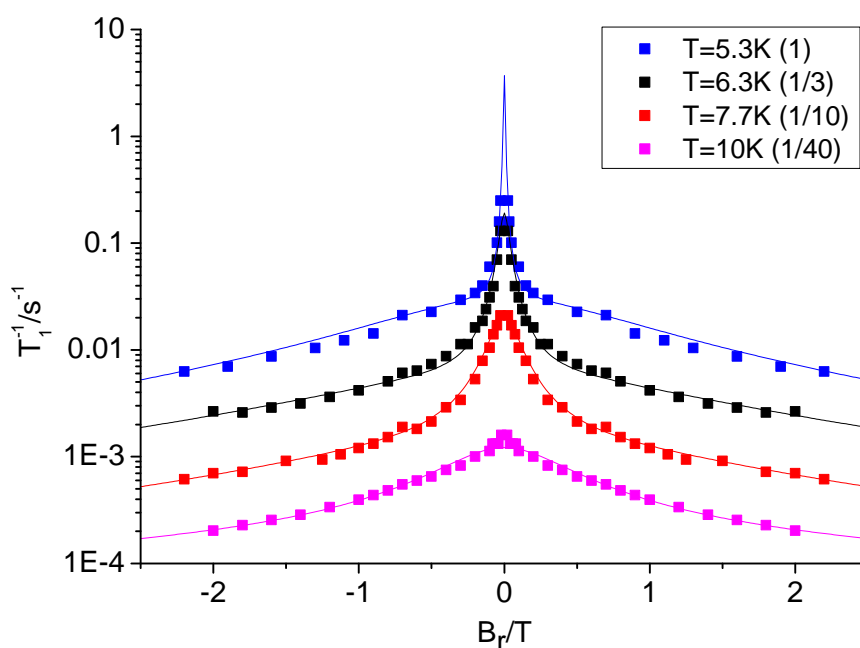


Figure 4.12: Dispersion of T_1^{-1} in annealed sample of complex **I** (toluene guest), $T = 5.3$ – 10 K. For clarity, the curves have been offset by the scale factor given in brackets. Data points have been reflected about $B_r = 0$ in order to accentuate the Lorentzian nature of the spectral density functions.

functions comprised more than one component.

The presence of two components in the spectral density functions can cause complications when fitting the data, and accurate separation of the two components may only be possible by constraining some of the fit parameters. This is especially true if one of the spectral density components is very narrow. The solid lines in figure 4.12 are fits to expression (4.2), with a constraint on the value of $C_{EE}^{(1)}$, the amplitude factor of the narrow component. Unconstrained fitting resulted in a large variation in $C_{EE}^{(1)}$ across the

data set.

With $C_{EE}^{(1)}$ constrained to an appropriate value, fitting the field-dependent data to equation (4.2) gives a satisfactory account of the data. At $T = 10\text{K}$ the agreement at low field suffers as the spectral density components broaden, and other narrow components manifest themselves in the T_1^{-1} dispersion curve. A similar observation was made when fitting the field-dependent data acquired from sample **VII**.

The Arrhenius plots of τ_c^{-1} versus inverse temperature show close agreement with the Arrhenius rate law, for both components of the spectral density functions (figure 4.13). The parameters measured from the Arrhe-

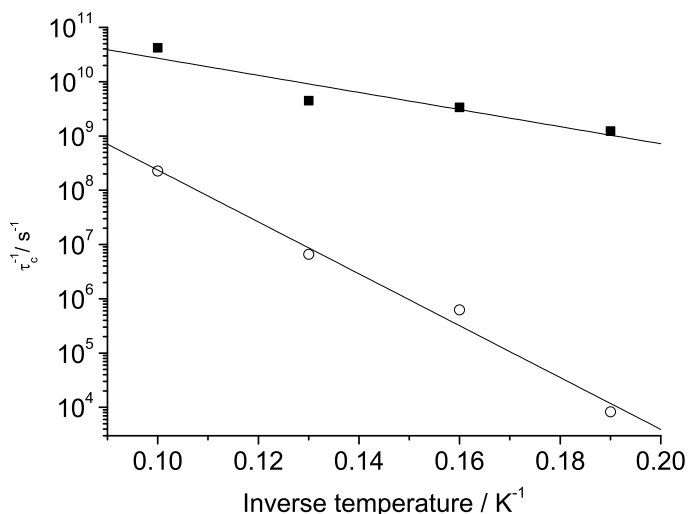


Figure 4.13: Plot of τ_c^{-1} as a function of inverse temperature, sample **I** (toluene guest), annealed. Black squares and white circles correspond to the broad and narrow components of the spectral density functions, respectively. Solid lines shown are fits to the Arrhenius rate law; measured activation energy parameters are $E_a^{(1)} = 48 \pm 3\text{K}$ and $E_a^{(2)} = 16 \pm 4\text{K}$. Error bars are small compared to marker size.

nius plots and spectral density functions are listed in table 4.3. The barrier heights required to produce the torsional splittings measured from the Arrhenius plots are also listed. The barriers were calculated by diagonalisation of the methyl-group rotational Hamiltonian, and assuming a purely threefold barrier.

It is interesting to note that the Arrhenius plot of τ_{c2}^{-1} (correlation rate of the broad component of the spectral density function) measures a torsional

Component	$\overline{C_{EE}}/s^{-2}$	τ_0^{-1}/s^{-1}	E_{01}/K	V_3/K	$\nu_t^{(0)}/meV$
(1) Narrow	2.1×10^6	3×10^{10}	48 ± 4	90 ± 10	0.26 ± 0.04
(2) Broad	$(2.7 \pm 0.3) \times 10^6$	1×10^{10}	16 ± 4	≈ 0	≈ 0.65

Table 4.3: Fit parameters, calculated barrier heights and ground state tunnel splitting for methyl groups in sample **I** (toluene guest), annealed. Value of $C_{EE}^{(1)}$ constrained during fitting.

splitting of $16 \pm 4K$, which is less than the smallest value of E_{01} possible for a methyl group, i.e. when $V_3 = V_6 = 0K$, $E_{01} = 22.8K$.

The solid lines plotted in figure 4.11 are the computed values of T_1 based on the BPP relaxation model and the parameters in table 4.3. Agreement between the model and the experimental data is good at low temperatures. The depths and positions of the T_1 minima are described well for each field. The notable deviation of the model from the experimental data occurs at $B_r = 0.7$ and $2.0T$, on the high temperature side of the T_1 minima. There is good agreement between the model and T_1 measured at $0.7T$ in the partially annealed sample. T_1 values measured at high temperature in the fully annealed sample are longer than the predicted values, however the gradient of the T_1 -inverse temperature curve is similar to that of the model.

4.5 Rotation of γ -picoline methyl groups in a calixarene host-guest complex

γ -picoline (or 4-methyl-pyridine) has one of the weakest methyl-group hindering potentials measured for any sample in the solid state, which gives rise to a large tunnel splitting of $0.52meV$ ($6.0K$) [29]. Complexation with a calixarene host causes modification of the hindering barrier. In this section, results from measurements of the temperature dependence of T_1 in quench cooled and annealed samples of a (1:1) complex of *p-tert*-butylcalix[4]arene and γ -picoline (sample **II**) are presented, along with measurements of the dispersion of T_1^{-1} in the temperature range 5–20K. Characterisation of the methyl-group environments is attempted.

4.5.1 Thermal history effects

T_1 was measured as a function of temperature at $B_r = 0.7T$, in quench cooled (probe **C**) and annealed samples (probe **A**) of complex **II**. T_1 was monoexponential in both cases, however the value of T_1 was dependent on the thermal history of the sample. The plots of T_1 versus inverse temperature

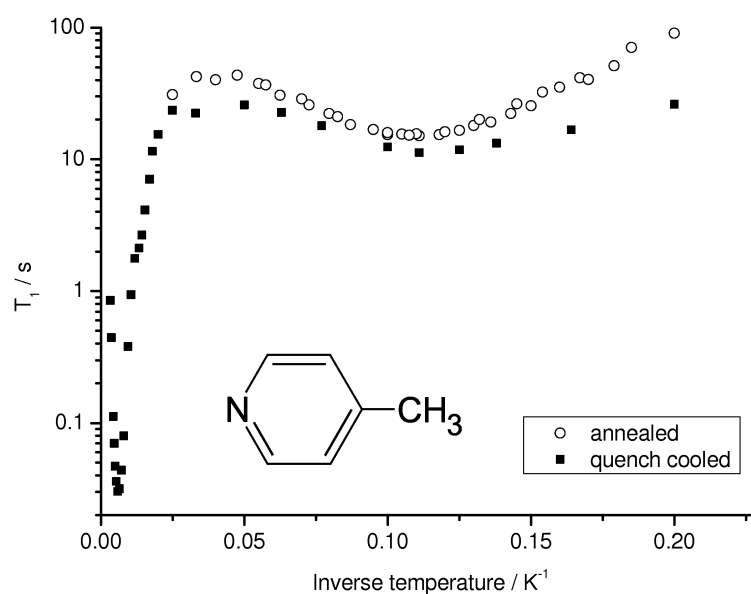


Figure 4.14: Temperature dependence of T_1 in sample **II** (γ -picoline guest), $B_r = 0.7T$. Quench cooled sample measured with probe **A** (constant field); annealed sample measured with probe **C** (field-cycling). Error bars are small compared to marker size.

(figure 4.14) display a T_1 minimum at low temperature; $\theta_{\min} = 8.9$ and 9.3K for the quench cooled and annealed samples, respectively. The appearance of a low-temperature T_1 minimum is consistent with the presence of weakly hindered methyl groups in this sample. At the T_1 minima, the measured T_1 values differ by a factor of 1.3, and the greatest difference between the measured values is at 5K , where the difference is a factor of 3.5.

4.5.2 Methyl group dynamics in an annealed sample

The temperature dependence of T_1 , measured at four distinct relaxation fields ranging from 0.02 to $2.0T$, is presented in figure 4.15. The low temperature T_1 minimum can be clearly seen at each field strength and, as ex-

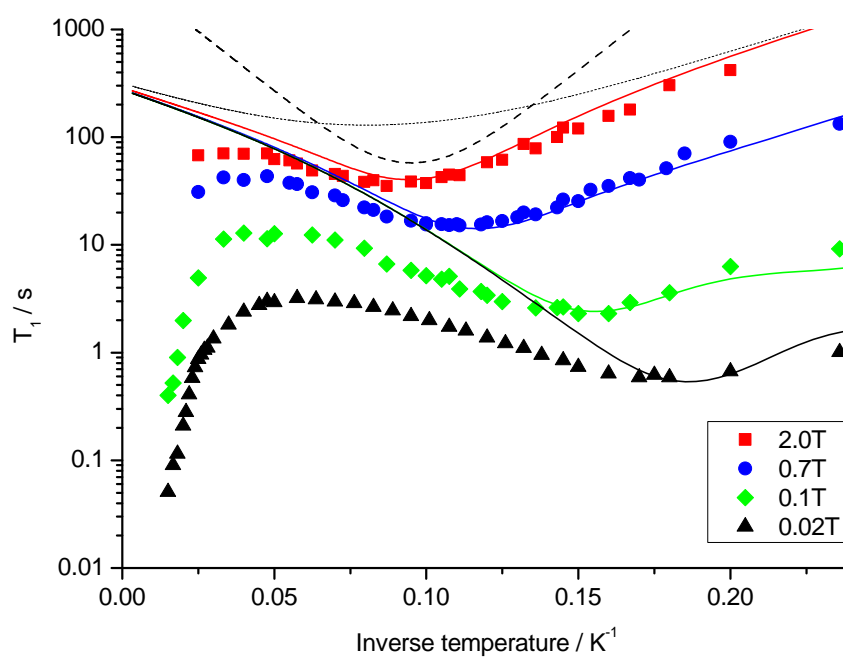


Figure 4.15: Temperature dependence of T_1 in sample **II** (γ -picoline guest), annealed, measured at $B_r = 0.02, 0.1, 0.7, 2.0\text{T}$ (probe **C**). Error bars are small compared to marker size. Solid lines are computed from BPP model and parameters in table 4.3. Dashed lines show the individual contribution of each distinct methyl-group environment, calculated for $B_r = 2.0\text{T}$.

pected from the BPP model, the position of the low temperature minimum moves to higher temperature, and longer values of T_1 , as B_r is increased. The curves are also expected to converge to the same value of T_1 at high temperature as the methyl group motion enters the fast-motion regime and the spectral density function flattens out, however the curves in figure 4.15 clearly do not. The line that describes the locus of the T_1 minima has a gradient of around 40K, whereas the T_1 -inverse temperature curves on the low temperature side of θ_{\min} have a gradient of ~ 25 K. The BPP model dictates that these gradients should be equal. It is therefore obvious that the curves cannot be described by a single methyl group environment and a simple BPP model.

The T_1^{-1} dispersion curves measured at low temperatures (figure 4.16), illustrate the multi-component nature of the proton relaxation. The broad component becomes increasingly wide as the temperature increases. A narrow component is consistently present at all temperatures. Attempts to fit the dispersion curves to two components, described by equation (4.2), yielded unsatisfactory fits, and parameters varied greatly across the data set. A better description of the broad component was achievable by discounting the low-field data from the fit and fitting the $B_r \geq 0.8$ T data to the expression for a single spectral density component (i.e. equation (4.2) with $C_{EE}^{(2)} = 0$), therefore attenuating the influence of the narrow component on the broad component. Satisfactory fits were not possible with a global value of the dipolar coupling constant, as a result of the presence of the narrow component. The average value of C_{EE} , from fits of the $T = 6.9$ – 14.29 K data, is $8 \pm 2 \times 10^6 \text{s}^{-2}$. The resulting correlation rates are presented on the Arrhenius plot in figure 4.18. The data follow an Arrhenius rate law fairly well, with the Arrhenius law characterised by $E_a = 21 \pm 1$ K and $\tau_0^{-1} = 4 \times 10^9 \text{s}^{-1}$.

The activation energy of the Arrhenius law was interpreted as E_{01} , and modelling of the T_1 -temperature dependence was attempted, based on a single unhindered methyl-group. It was found that a satisfactory description of the T_1 -temperature curves is impossible with a single BPP component. As a result INS spectra were consulted in order to inform and develop the modelling.

INS experiments on complex **II** have been previously reported by Caciuffo and co-workers [56]. The low-temperature spectrum is presented in fig-

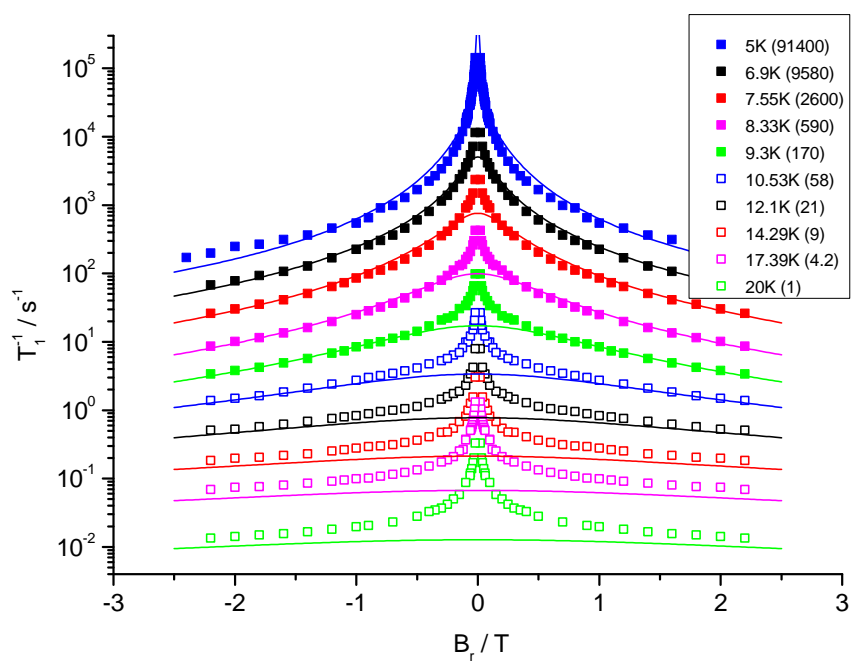


Figure 4.16: Dispersion of T_1^{-1} in annealed sample of complex **II** (γ -picoline guest), $T = 5$ – 20 K. For clarity, the curves have been offset by the scale factor given in brackets. Data points have been reflected about $B_r = 0$ in order to accentuate the Lorentzian nature of the spectral density functions. Solid lines show calculated dispersion curves, based on the model summarised in table 4.4.

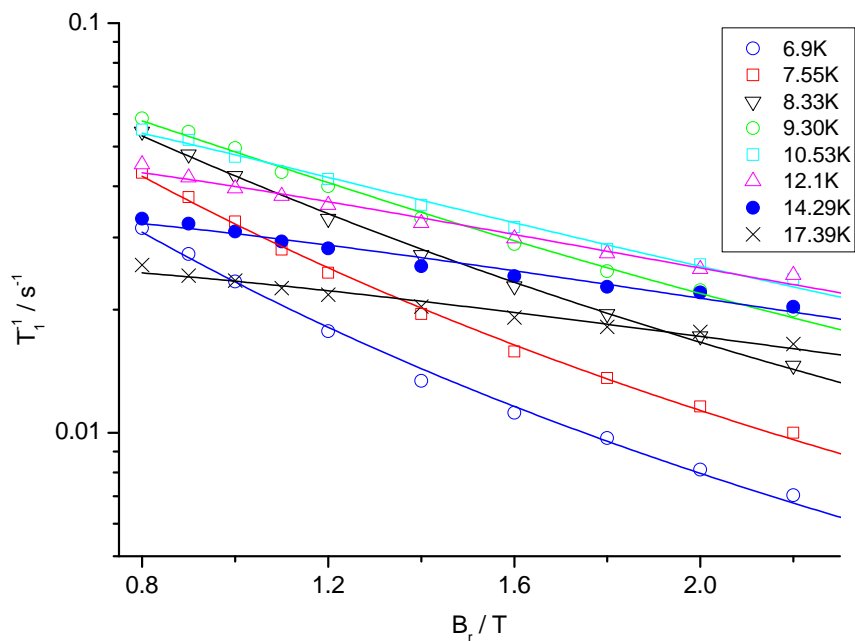


Figure 4.17: High field ($B_r \geq 0.8$) regions of T_1^{-1} dispersion curves in sample **II** (γ -picoline guest), annealed. Solid lines are fits to single spectral density component.

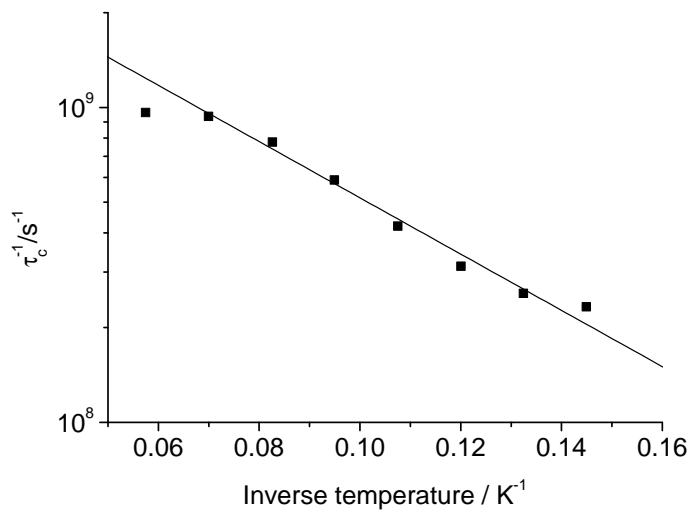


Figure 4.18: Plot of τ_c^{-1} versus inverse temperature for broad component of T_1^{-1} dispersion curves in annealed sample of complex **II** (γ -picoline guest). Error bars are small compared to marker size. Solid line shown is a fit to the Arrhenius rate law; measured activation energy $E_a = 21 \pm 1$ K. Data point at $T = 17.39$ K omitted from fit.

ure 4.19(a). There are multiple excitation bands in the range 0.17–0.63meV,

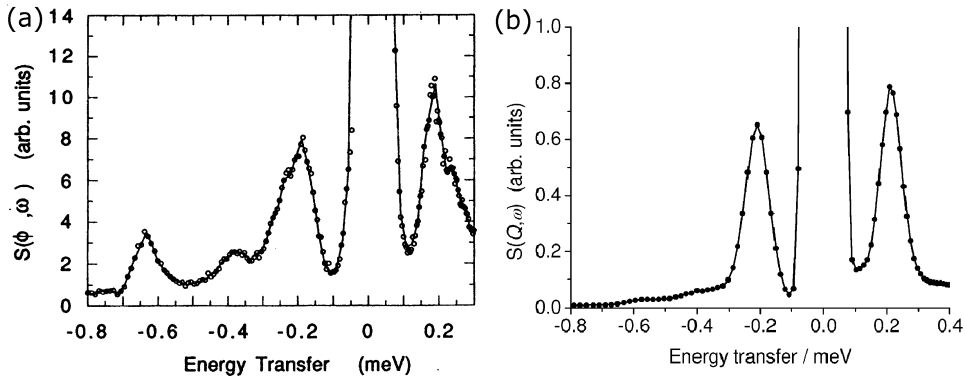


Figure 4.19: (a) INS spectrum of *p-tert*-butylcalix[4]arene(1:1) γ -picoline at 5K (taken from Ref. [56]); (b) INS spectrum of sample **II** (γ -picoline guest) at $T = 2.5$ K (courtesy of A.J. Horsewill [57]).

with the most intense at 0.23meV. These have been interpreted as being the various tunnel splitting lines for several crystallographically inequivalent methyl-group environments. Figure 4.19(b) displays a spectrum that has recently come to light, acquired from the same sample that has been analysed in this thesis by field-cycling NMR [57].

There are some very noticeable differences between the two spectra in figure 4.19. Spectrum (b) displays a single excitation at 0.210meV; all other peaks observed in spectrum (a) are absent from spectrum (b). The position of the peak in (b) is approximately coincident with the most intense peak in spectrum (a), and is characteristic of the tunnel-splitting of a methyl-group hindered by a barrier of $V_3 = 105$ K ($E_{01} = 56$ K). The presence of unhindered methyl-groups, as indicated by the broad component of the spectral density functions and subsequent Arrhenius plot, should be revealed by an excitation at ~ 0.65 meV. There is no feature in this region in spectrum (b), but there is an excitation at 0.627meV in spectrum (a).

An additional component, with parameters based on the tunnel splitting observed in spectrum (b), was included in the modelling of the T_1 -inverse temperature curves. The values of τ_0^{-1} , C_{EE} and E_{01} were adjusted, for both components, in order to gain the best description of the experimental data. The resulting model is displayed as solid lines in figure 4.15. The parameters for the model are listed in table 4.4. The model gives a fairly good account of the data at temperatures below θ_{\min} , for all fields. The

	E_{01}/K	$\tau_0^{-1}/\text{s}^{-1}$	C/s^{-2}	V_3/K	V_6/K	$\nu_t^{(0)}/\text{meV}$
(1)	20	4.35×10^9	2.9×10^6	0	0	0.65
(2)	51	1.11×10^{11}	6.5×10^6	69	105	0.22

Table 4.4: Parameters of methyl-group environments in sample **II** (γ -picoline guest). Environment (1) based on the broad component of the spectral density functions (figure 4.17); environment (2) based on the tunnelling excitation observed in INS spectrum (figure 4.19)(b). Values of V_3 , V_6 , and $\nu_t^{(0)}$ are from calculations.

depths and positions of the T_1 minima are in good agreement with the data. However, at temperatures greater than θ_{\min} , the data diverges from the model. The relaxation times predicted by the model are much longer than those observed, and the gradients of the T_1 -temperature curves are overestimated.

The solid lines plotted in figure 4.16 display the field-dependence of the relaxation rate, as predicted by the model. The calculated T_1^{-1} dispersion curves poorly describe the low-field data at all but the lowest temperatures. The calculated curves broaden as temperature increases, whilst the narrow component observed in the spectral density function persists and broadens very little. The agreement in the high-field region is good at temperatures below 10.53K; above this temperature, the calculated curves broaden out beyond the experimental window, and contribute to the broad background component observed in the spectral density functions.

The narrow component of the T_1^{-1} dispersion curves, which is unaccounted for by the model, is characteristic of a slow motional process with a small activation energy. It is this motion that is responsible for the broad, shallow features at $T > \theta_{\min}$ in the T_1 -inverse temperature data. The exact nature of this motion remains undetermined, however the likelihood that it is due to the rotation of guest methyl-groups is slim.

4.6 The effect of host molecule deuteration on proton T_1

The relaxation power of a methyl rotor is shared between all protons it is coupled to, via the process of spin diffusion. By reducing the number of protons in the sample, for example by replacing some of the protons with deuterons, the heat capacity of the proton Zeeman reservoir decreases. This

can increase the efficiency of spin-lattice relaxation and therefore reduce T_1 . The strength of the magnetic dipole-dipole coupling between protons is reflected in the homonuclear dipolar coupling constant C_{HH} . The magnetic dipole-dipole interaction is dependent on the internuclear distances and also the number of protons in the sample.

Two samples of complex **I** with partially deuterated calixarene host molecules were prepared by the University of Southampton synthesis laboratory. In sample **I**_{d2} the protons belonging to the *tert*-butyl groups and the phenolic units were replaced with deuterons (close to 70% of the total number of hydrons in the complex). In sample **I**_{d1} only the *tert*-butyl groups were deuterated, which account for around 56% of total number of hydrons. The *tert*-butyl protons account for over half of all the protons in the complex (72 protons out of every 128 in a unit cell; one unit cell consists of two (1:1) complexes), therefore by replacing them all with deuterons, a large difference in the dipolar coupling constant, and T_1 , was expected.

4.6.1 Temperature dependence of T_1

In figure 4.20 the temperature dependence of T_1 in quenched cooled samples of the deuterated complexes are presented along with data from the fully protonated sample.

T_1 minima are well resolved in each T_1 -inverse temperature curve. $T_1(\theta_{\text{min}})$ appears to become shorter with increased deuteration; the fully protonated sample has the longest T_1 (20.7s), followed by **I**_{d1} (16.7s) and **I**_{d2} (13.9s). The gradient of the curves either side of the T_1 minima also vary according to this trend. On the low temperature side of the T_1 minimum, the gradient increases with the degree of deuteration, and on the high temperature side, the gradient decreases (see table 4.5). It has been demonstrated in previous

Sample	θ_{min} / K	$T_1(\theta_{\text{min}})$	$E_a^{(+)}/K$	$E_a^{(-)}/K$
I	7.7	20.7	-34.9 ± 0.9	5.6 ± 0.5
I _{d1}	8.8	16.7	-32.2 ± 0.6	9.5 ± 0.4
I _{d2}	9.1	13.9	-31 ± 2	11.0 ± 0.6

Table 4.5: Parameters of T_1 -inverse temperature curves of partially deuterated samples of complex **I** (toluene guest), quench cooled. $E_a^{(+)}$ and $E_a^{(-)}$ denote gradient of curves on high-temperature and low-temperature side of θ_{min} .

sections that the features of the T_1 -inverse temperature curves in quench

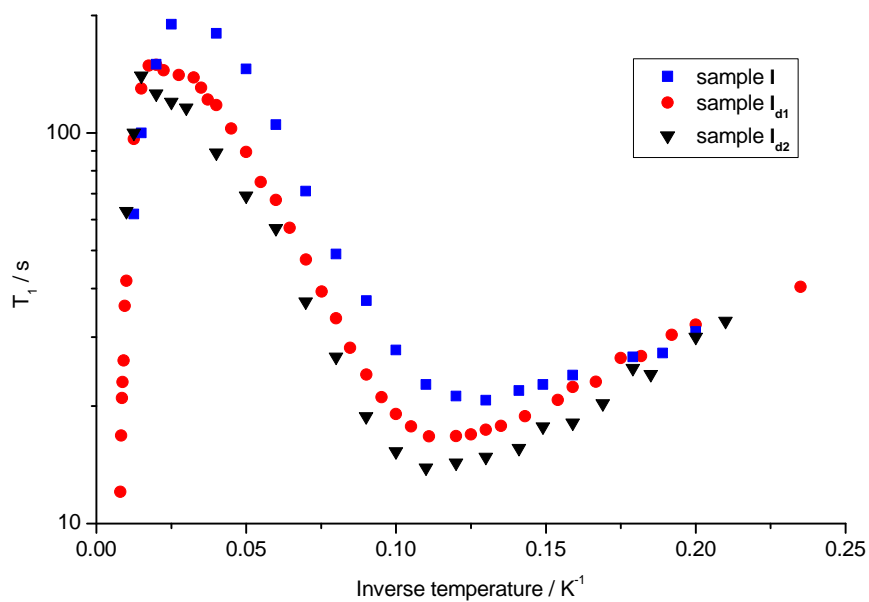


Figure 4.20: Temperature dependence of T_1 in fully protonated and partially deuterated samples of *p-tert*-butylcalix[4]arene(1:1)toluene (quench cooled), $B_r = 0.7T$. Error bars are small compared to marker size.

cooled samples are due to numerous methyl-group environments, therefore it is not possible to draw firm conclusions about the modification of potential barriers caused by deuteration, based on the data from figure 4.20 alone.

4.6.2 Calculation of the dipolar coupling constant

A model was formulated in order to explain quantitatively the effect that deuteration has on the proton relaxation time. The differences in $T_1(\theta_{\min})$ were related to the difference in the calculated values of the dipolar coupling constant. The model was based on a model for proton transfer in benzoic acid dimers [58]. In this system, protons hop between two sites, thereby modulating the magnetic dipole-dipole interaction and inducing proton relaxation. The rotational motion of methyl groups is more complicated than two-site hopping, however this model may serve as a first approximation.

The total dipolar coupling constant has contributions from both *homo*- and heteronuclear interactions, i.e. $C_{\text{tot}} = C_{\text{HH}} + C_{\text{HD}}$. C_{tot} was calculated by performing a lattice sum of the internuclear vectors between the protons of a methyl group (located at the centre of the generated lattice; see below) and all other protons (or deuterons) that do not belong to guest methyl-groups. These hydrons are *probe nuclei*, which act as observers of the methyl-group rotation.

The internuclear distances and angles were determined by simulating the crystal lattice of complex **I** using Matlab. The simulated lattice was based on crystal parameters found from room temperature XRD measurements, undertaken by our aforementioned collaborators, on a single-crystal sample of complex **I** (table 4.6). It was assumed that deuteration would not sig-

Crystal system	tetragonal
Space group	$P4/n$
Unit cell dimensions	$a = 12.5503(2)\text{\AA}$ $c = 13.7878(4)\text{\AA}$
Z	2

Table 4.6: Crystal structure parameters of complex **I** (toluene guest), determined by XRD measurements on single crystal at room temperature

nificantly alter the crystal structure of the calixarene-toluene complex. A crystal lattice of $5 \times 5 \times 5$ unit cells was used in calculations, as this size was found to be large enough to approximate an infinite lattice.

The geometrical parameters used in the model are defined in figure 4.21. A methyl group, located at the centre of the generated crystal lattice, is

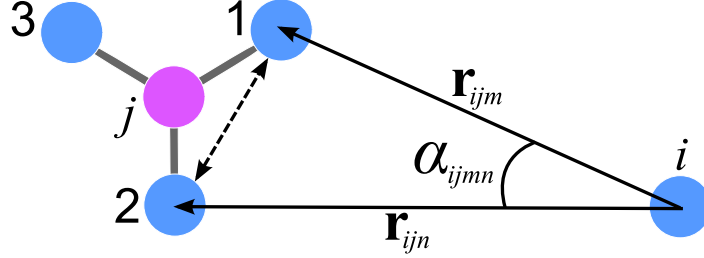


Figure 4.21: Definition of geometrical parameters used in model for approximating methyl group rotation.

labelled j . r_{ijm} is the internuclear vector from a probe nucleus i to the m^{th} proton in methyl group j , and α_{ijmn} is the angle between r_{ijm} and r_{ijn} . The probe nucleus may be at the position of any proton in the lattice, with the exception of the ‘stationary’ proton in methyl group j . T_1 is inversely proportional to C_{HH} , which is given by the following expression adapted from [58]:

$$C_{\text{HH}} = \frac{1}{2} \frac{1}{3} \frac{3\gamma_{\text{H}}^4 \hbar^2}{40} N \left(\frac{\mu_0}{4\pi} \right)^2 \times \sum_{\substack{m,n \\ m \neq n}}^3 \sum_i \left[r_{ijm}^{-6} + r_{ijn}^{-6} + r_{ijm}^{-3} r_{ijn}^{-3} (1 - 3 \cos^2 \alpha_{ijmn}) \right]. \quad (4.3)$$

This is a lattice sum of the dipolar contacts between the central methyl-group j , and the rest of the proton positions in the lattice (sum over i). In this model, C_{HH} is calculated for hopping between all pairs of sites in a methyl group (summation over m and n) and averaged (hence the pre-factor of $1/3$). The pre-factor of $1/2$ corrects for the summation over equivalent cases (i.e. $m \rightarrow n \equiv n \rightarrow m$). N is the ratio of the number of methyl protons to the total number of protons in the crystal lattice. In the deuterated samples, the heteronuclear contribution to the total dipolar coupling constant

is given by:

$$C_{\text{HD}} = \frac{1}{2} \frac{1}{3} \frac{\gamma_{\text{H}}^2 \gamma_{\text{D}}^2 \hbar^2}{40} \left(\frac{\mu_0}{4\pi} \right)^2 \times \sum_{\substack{m,n \\ m \neq n}}^3 \sum_k \left[r_{kjm}^{-6} + r_{kjn}^{-6} + r_{kjm}^{-3} r_{kjn}^{-3} (1 - 3 \cos^2 \alpha_{kjm}) \right]. \quad (4.4)$$

In this expression k labels the position of the deuterium atoms in the lattice, and γ_{D} is the magnetogyric ratio of deuterium ($\gamma_{\text{D}} \approx \gamma_{\text{H}}/6.5$).

The values of C_{tot} calculated using the described model (referred to as C_{calc}) are presented in table 4.7, and compared with C_{exp} , an estimate value based on the measured T_1 -inverse temperature curves. C_{exp} was determined

Sample	$C_{\text{calc}}/\text{s}^{-2}$	$C_{\text{exp}}/\text{s}^{-2}$
I	4.3×10^7 (1)	6.5×10^6 (1)
I_{d1}	9.1×10^7 (2.1)	8.0×10^6 (1.2)
I_{d2}	10.9×10^7 (2.5)	9.7×10^6 (1.5)

Table 4.7: Calculated values of the dipolar coupling constant in fully protonated and partially deuterated samples of complex **I** (toluene guest). The numbers in brackets compare the values of $C_{\text{calc/exp}}$ in the deuterated samples with the values from the fully protonated sample.

by finding a suitable value of the dipolar coupling constant that simulated well the depth of the T_1 minimum. Comparison of the absolute values C_{calc} and C_{exp} shows that the calculated values are an order of magnitude larger than C_{exp} . C_{exp} and C_{calc} differ by a similar factor for the deuterated samples (~ 0.09), however the factor for sample **I** is almost twice this value. There is not enough evidence from these experiments to appeal to an ‘efficiency factor’, which is common to all samples, to account for the difference in the values of C_{calc} and C_{exp} .

The calculated values of the dipolar coupling constant increase with the degree of deuteration, and this is in agreement with what is observed experimentally. Although there are discrepancies between the absolute values of C_{tot} , the relative values in deuterated samples compared to the value in the fully protonated sample are of the same order of magnitude, and are in good qualitative agreement.

4.7 T_1 measurements in other calixarene complexes

Sample III (chlorotoluene guest)

T_1 was measured for both quench cooled and annealed samples, at $B_r = 0.7T$, using probe C (figure 4.22). The relaxation curves were monoexponen-

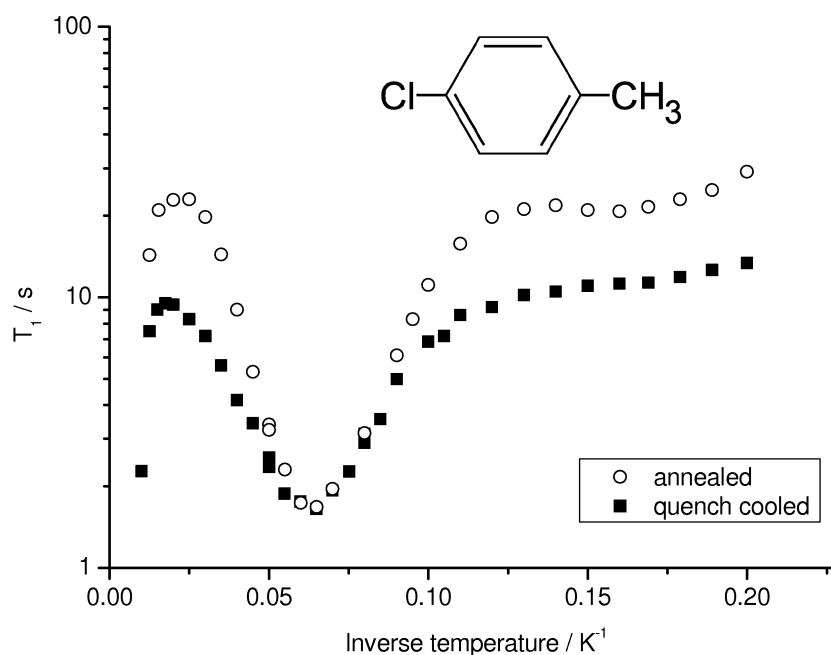


Figure 4.22: Temperature dependence of T_1 , sample III (chlorotoluene guest), $B_r = 0.7T$ (probe C field-cycling).

tial (i.e. characterised by a single relaxation time, and fitted to equation 3.4). At temperatures below 8.33K ($T^{-1} = 0.12K^{-1}$) T_1 differs by a factor of ~ 2 between slow cooled and quench cooled samples. Both curves are fairly flat and broad at low temperatures, and there is a hint of a minimum in the slow cooled sample at 6.25K ($0.16K^{-1}$). Above 8.33K the difference in T_1 narrows. Indeed at the T_1 minimum there is no difference between the values of T_1 measured; in both cases $T_1(\theta_{\min}) = 1.7s$. The T_1 minimum appears at 15.5K ($0.0645K^{-1}$) for both thermal preparations. The gradient on the high temperature side of θ_{\min} is 98K for the annealed sample.

In general, θ_{\min} is higher for rotors that are more hindered. For bulk toluene the T_1 minimum at 30MHz ($B = 0.704T$) has been observed at

17K [31], indicating perhaps that the methyl rotor in sample **III** is less hindered than in bulk toluene. However, the potential barrier of bulk toluene, as measured by INS [31], predicts a librational splitting of 85K, which is less than the gradient measured from the T_1 vs. T^{-1} curve.

Sample IV (fluorotoluene guest)

The relaxation curves for sample **IV** were monoexponential for both quench cooled and annealed samples. The T_1 versus inverse temperature curves (figure 4.23) are fairly flat below 28.6K ($3.5 \times 10^{-3} \text{K}^{-1}$) for both annealed and quenched samples. The curves run almost parallel to each other,

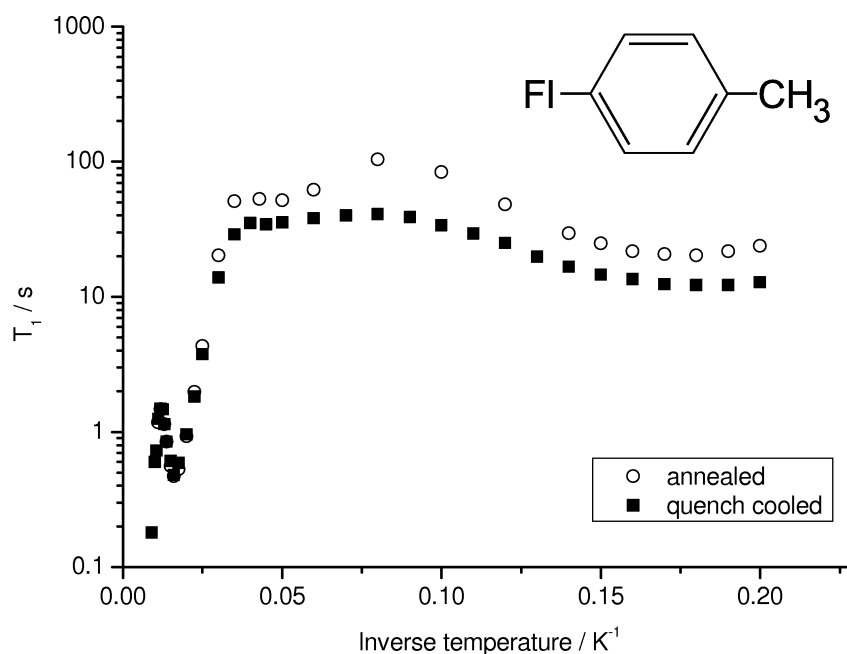


Figure 4.23: Temperature dependence of T_1 , sample **IV** (fluorotoluene guest), $B_r = 0.7T$ (probe **C**, field-cycling).

with T_1 differing by a factor of 1.5–2.7. As with sample **III** the curves begin to converge as the T_1 minimum is approached. Both curves are coincident at $\theta_{\min} = 62\text{K}$ ($1.62 \times 10^{-3} \text{K}^{-1}$), where $T_1 = 0.47\text{s}$. The gradient on the low temperature side of θ_{\min} is equal to 309K for the annealed sample. Although this T_1 minimum occurs at high temperature, and with relatively high activation energy, it is almost certainly due to the motion of the guest methyl

group and not the strongly hindered *tert*-butyl groups of the calixarene host. Above $\sim 83\text{K}$ ($1.2 \times 10^{-3}\text{K}^{-1}$) a steep gradient is apparent, which is the low temperature side of the T_1 minimum due to the motion of the *tert*-butyl groups.

Sample V (4-methylanisole guest)

T_1 was measured as a function of temperature in a quench cooled sample of complex **V** at $B_r = 0.91\text{T}$ (probe **C**). The relaxation was monoexponential for temperatures above 14.3K ($6.99 \times 10^{-2}\text{K}^{-1}$). The biexponential character of the relaxation curve below this temperature was slight, and the relaxation was estimated as being monoexponential. The change in the nature of the relaxation may be due to a structural phase transition in the sample. Below

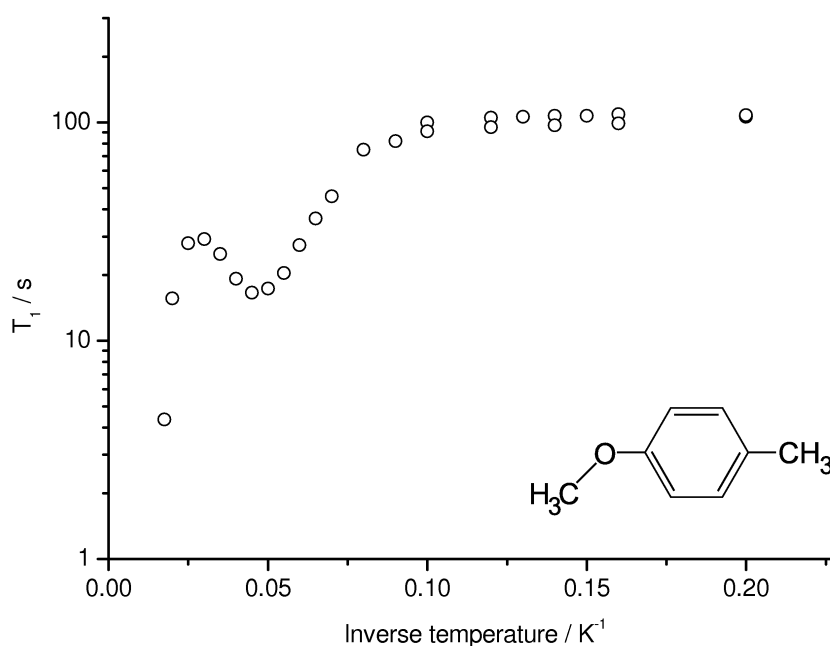


Figure 4.24: Temperature dependence of T_1 in quench cooled sample of **V** (4-methylanisole guest), $B_r = 0.91\text{T}$, (probe **C**, constant field). Relaxation was biexponential below 14.3K .

12.5K (0.08K^{-1}) T_1 is practically independent of temperature. The T_1 minimum occurs at $\theta_{\min} = 21\text{K}$ ($4.76 \times 10^{-2}\text{K}^{-1}$), and $T_1(\theta_{\min}) = 16.6\text{s}$.

Sample VI (acetone guest)

Sample **VI** was studied in the quench cooled configuration. The temperature dependence of T_1 was measured at $B_r = 0.7\text{T}$ using probe **A**. Below 15.3K ($6.54 \times 10^{-2}\text{K}^{-1}$) the relaxation was observed to be biexponential. However the relative amount of each component was not constant between measurements, and this gave rise to a degree of scatter in the values of T_1^a and T_1^b , therefore in figure 4.25 the approximation to monoexponential recovery is shown for temperatures below 15.3K. As with sample **V** the

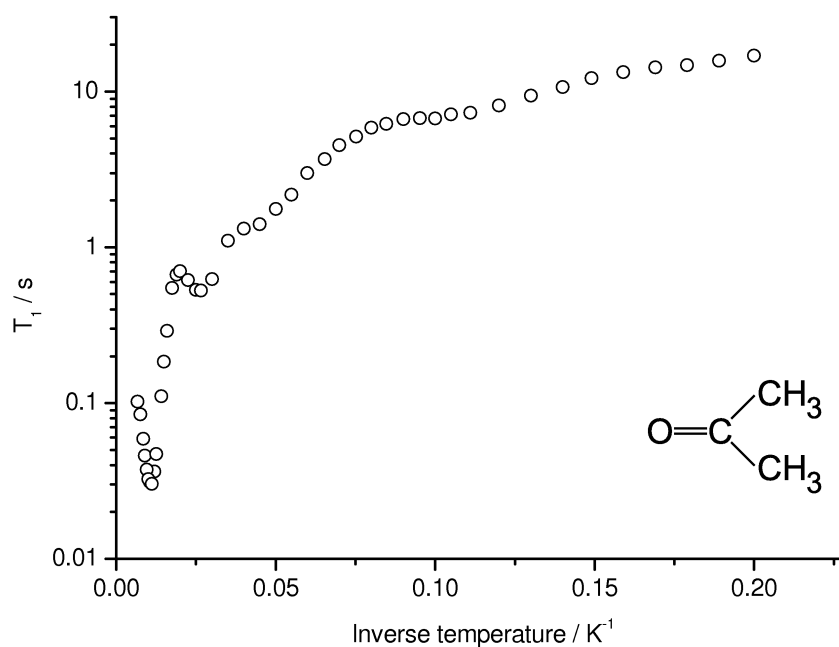


Figure 4.25: Temperature dependence of T_1 in sample **VI** (acetone guest), quench cooled, $B_r = 0.7\text{T}$ (probe **A**, constant field). Relaxation was biexponential below 15.3K.

change from biexponential to monoexponential relaxation is most probably due to a phase change.

The T_1 temperature curve is relatively featureless; with the exception of the *tert*-butyl minimum at high temperature, there are few other clear features. An apparent T_1 minimum can be seen at 40K, but it is not distinct enough to make an estimation of the environment of the methyl group that causes it.

Sample VIII (iodomethane guest)

Relaxation curves of quench cooled sample **VIII** (probe **A**, $B_r = 0.7T$) were observed to be biexponential, and unlike the previous samples discussed in this section, the biexponential nature was maintained right up to high temperatures (figure 4.26). The relaxation was biexponential up to 66.7K; at temperatures greater than this the relaxation was monoexponential in nature.

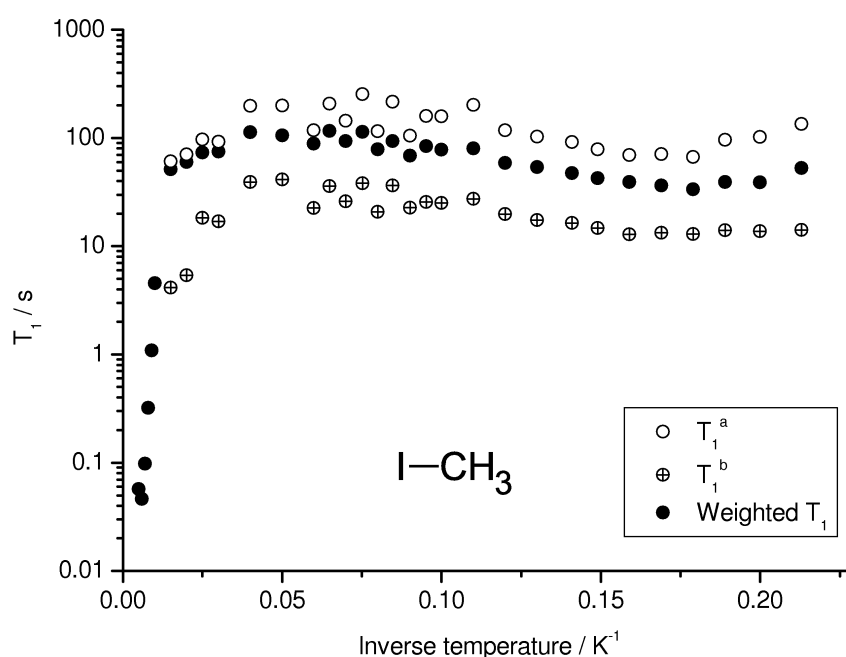


Figure 4.26: Temperature dependence of T_1 in sample **VIII** (iodomethane guest), quench cooled, $B_r = 0.7T$ (probe **A**, constant field). Relaxation was observed to be biexponential up to 66.7K.

At low temperatures the relaxation curves were dominated by the T_1^b component, the quicker of the two components. At 5K the $M_0^{(a)} : M_0^{(b)}$ ratio was 1 : 2.5. With increasing temperature, the ratio gradually favoured the slower T_1^a component; by 66.7K the $M_0^{(a)} : M_0^{(b)}$ ratio was 5 : 1. The change in the relative proportions of the components could be indicative of gradual structural changes in the sample.

In figure 4.26 the relaxation components are plotted, along with the

weighted value of T_1

$$T_1^w = \frac{(M_0^{(a)} \cdot T_1^a) + (M_0^{(b)} \cdot T_1^b)}{M_0^{(a)} + M_0^{(b)}} , \quad (4.5)$$

which is a measure of the average relaxation time of the system. The T_1^w versus inverse temperature curve for sample **VIII** is very flat and broad at low temperatures, with a shallow minimum at 5.6K (0.18K^{-1}). The methyl group in bulk iodomethane has a relatively large hindering barrier ($V_3 = 476\text{K}$ [31]), and the large T_1 values measured for sample **VIII** at low temperatures are consistent with this.

Sample IX (2-butyne guest)

Sample **IX** proved to be rather sensitive to temperature cycling, and it was difficult to find a configuration or thermal treatment that was robust to cycling from high to low temperatures. T_1 was initially measured as a function of temperature for a slowly cooled sample ($B_r = 0.86\text{T}$, probe **B**) and the relaxation curves were of monoexponential character. Typical experimental protocol for determining the temperature dependence of T_1 involved making measurements at the lowest temperatures before ascending to higher temperatures. After the initial temperature sweep, sample **IX** was slow cooled back down to low temperatures in order to complete the T_1 vs. T^{-1} curve. After cooling, the relaxation curves were observed to have become biexponential in nature. The two components differed by around a factor of 8. The longer component had a relaxation time that was similar to the T_1 measured from the monoexponential relaxation curves, and accounted for around 80% of the amplitude of the biexponential relaxation curves.

Further attempts were made to anneal the sample by bringing it to room temperature for an hour and repeating the slow cooling process. However this again changed the nature of the relaxation and put the sample into yet another configuration. After this cooling process the relaxation was of biexponential character, but a very long T_1 component ($> 200\text{s}$) emerged in the relaxation curves. However, the dominant component was the shorter component. Approximating the relaxation curve by fitting to monoexponential recovery resulted in values of T_1 similar to the components measured previously.

In figure 4.27 the T_1 component that appeared consistently in all relax-

ation curves of sample **IX** is plotted as a function of temperature. There is a distinct T_1 minimum at 53K ($1.89 \times 10^{-2} \text{K}^{-1}$). The gradient of the curve at the low temperature side of θ_{\min} is $114 \pm 7 \text{K}$. The hindering potential in bulk 2-butyne has been measured to be $V_3 = 324 \text{K}$ and $V_6 = 26 \text{K}$ [31]. Using these values, the torsional splitting is predicted to be equal to 137K, which is similar to the gradient measured below θ_{\min} . It is very likely therefore that this minimum is due to the rotation of the methyl groups of 2-butyne.

In a (1 : 1) complex of *p*-isopropylcalix[4]arene and 2-butyne, the butyne molecule sits in the calixarene cavity with its molecular axis running along the four-fold symmetry axis of the calixarene molecule. Each methyl group belonging to the 2-butyne molecule experiences a different hindering potential, therefore at least two minima (excluding the iso-propyl minimum) should be manifested in the T_1 vs. inverse temperature data. The apparent minima at 10.6K ($9.4 \times 10^{-2} \text{K}^{-1}$) and 21.4K ($4.7 \times 10^{-2} \text{K}^{-1}$) could be due to the inequivalent methyl rotors. Presumably, the methyl group within the calixarene cavity is the less hindered rotor, giving rise to the low temperature minimum. This assignment could be tested perhaps measuring the temperature dependence of T_1 in a (2 : 1) complex of calixarene and 2-butyne, analogous to sample **VII**, if indeed it is possible for such a complex to be crystallised.

Sample **X** (nitromethane guest)

The calixarene host of sample **X** was functionalised with ethylcarbonate group substituents at the hydroxyl positions (figure 4.2(a)). The ethyl groups each have one methyl rotor, which are expected to be strongly hindered in this complex.

Relaxation in sample **X**, after quench cooling, was observed to be biexponential. The biexponential nature of the relaxation persisted up to 50K (0.02K^{-1}), and unlike the previous samples, the relative amount of each component remained fairly constant. The short component, T_1^b , dominated the relaxation curve, and between 5–50K the average value of M_0^a/M_0^b was 0.34 with a standard deviation of 0.04. Above 50K the relaxation curves appeared much less biexponential, and were therefore fitted using the monoexponential expression.

In figure 4.28 the two relaxation components are plotted, along with the weighted value of T_1 . Above 50K, the T_1 values from monoexponential

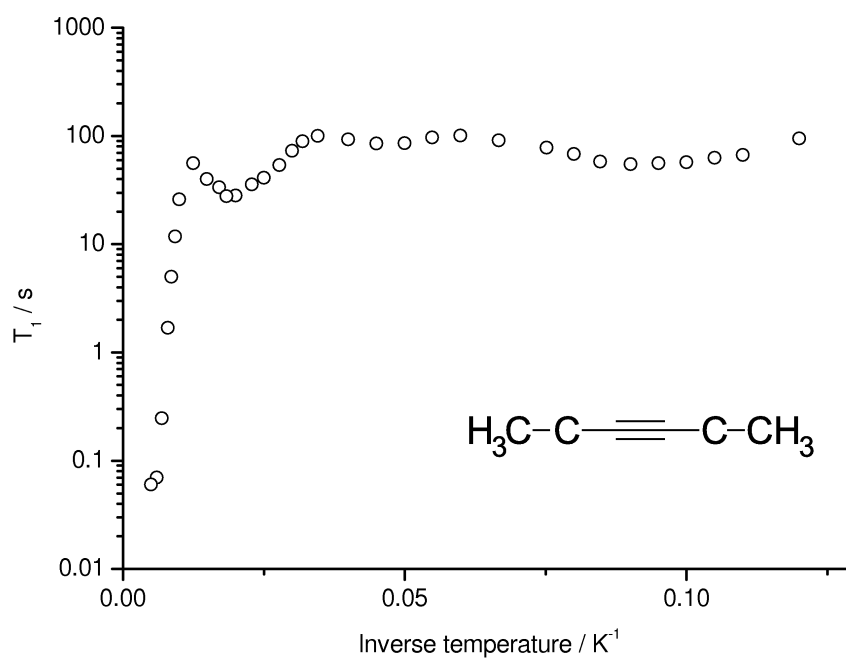


Figure 4.27: Temperature dependence of T_1 , sample **IX** (2-butyne guest), slow cooled, $B_r = 0.86T$ (probe **B**, constant field).

fits of the relaxation curves are plotted. At low temperatures, there are no

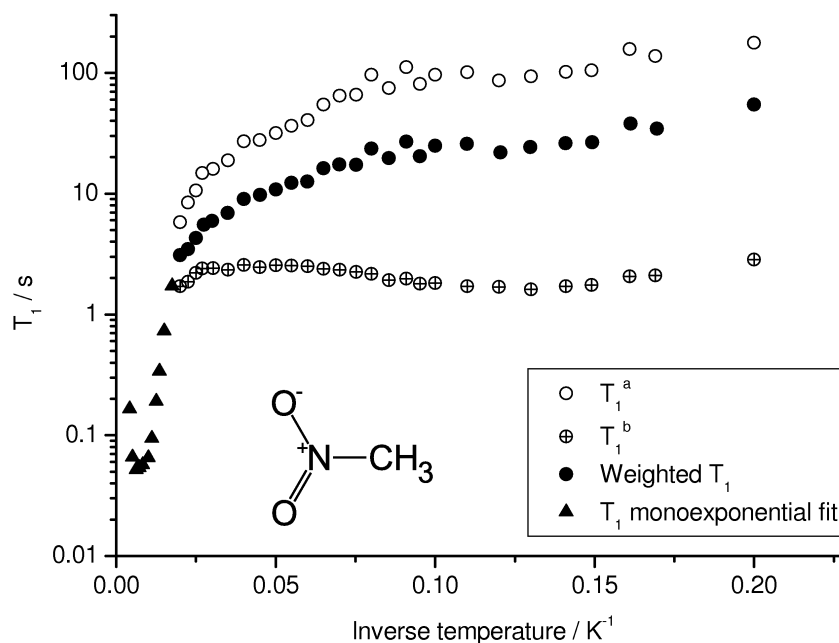


Figure 4.28: Temperature dependence of T_1 , sample **X** (nitromethane guest), quench cooled, $B_r = 0.7\text{T}$ (probe **A**, constant field).

distinct features in the T_1 dependence that can be attributed to guest methyl group dynamics. T_1^w becomes shorter at high temperatures and the change is gradual. The T_1 minimum at 138K ($7.25 \times 10^{-3}\text{K}$) due to the strongly hindered methyl groups of the calixarene host is the only clear feature.

Sample XI

The temperature dependence of T_1 was measured for a quench cooled sample of complex **XI**. The relaxation curves collected were of monoexponential character, and remained as such even after cycling back down to low temperature after an initial batch of measurements. As with several of the other samples, the only distinct feature of the T_1 vs. T^{-1} curve is the high temperature minimum, which for sample **XI** is located at 150K. The high temperature minimum cannot be described by a single BPP minimum. It is likely to be a superposition of minima from the two types of methyl group present i.e. the groups that comprise the *tert*-butyl groups, and those

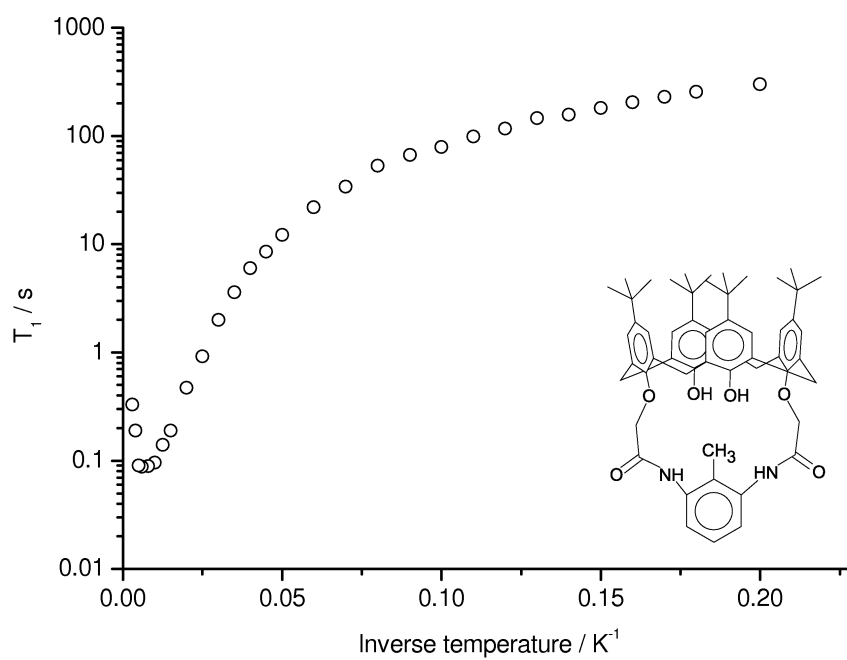


Figure 4.29: Temperature dependence of T_1 , sample **XI**, quench cooled, $B_r = 0.91T$ (probe **C**, constant field).

bonded to the aromatic ring on the ‘bridge’ of the molecule. There is not enough information to determine the contribution of these components, however measurement of the temperature dependence of T_1 at different field strengths, and measurement of the dispersion of T_1 could aid in separation of the components.

4.8 Discussion and Summary

NMR-relaxometry has been demonstrated to be a useful technique for studying molecular motion in organic complexes. Measurements of the proton spin-lattice relaxation time as a function of temperature can reveal the presence of particular dynamic processes, and frequency-dependent measurements can be used to measure the correlation times of the motion. From Arrhenius plots of the measured correlation rates, the torsional splitting E_{01} may be measured. In the cases of the (2:1) complex of calixarene/*p*-xylene (sample **VII**) and the (1:1) complex of calixarene/toluene (sample **I**), this approach has yielded estimates for the tunnel-splitting in annealed samples that agree well with INS spectra.

Results from INS measurements on sample **VII** have recently become available, and tunnelling peaks have been observed at 0.20 and 0.39meV [57]—the model based on the NMR relaxometry measurements predicts tunnel splittings of $0.20 \pm 0.03\text{meV}$ and $0.46 \pm 0.04\text{meV}$, assuming purely three-fold barriers. The methyl-group environments determined by field-cycling NMR measurements lead to predictions of the tunnelling frequencies which are in very good agreement with the observed INS spectrum. The two inequivalent environments are most likely due to methyl groups belonging to different guest molecules; there is no evidence to suggest that the symmetry between the methyl groups bonded to the same *p*-xylene molecule is broken.

Low-temperature INS spectra for *p*-*tert*-butylcalix[4]arene(1:1)toluene (complex **I**), acquired by Caciuffo and co-workers [56], are displayed in figure 4.30. At temperatures below and including 6K, there is a prominent transition peak at 0.63meV, and relatively broad excitation bands at $\sim 0.40\text{meV}$ and $\sim 0.20\text{meV}$. These features can be interpreted as the tunneling peaks of crystallographically inequivalent methyl groups. The peak at 0.63meV indicates the presence of almost free methyl-rotors. A tunnel splitting of $\nu_t^{(0)} = 0.26 \pm 0.04\text{meV}$ is predicted by characterisation of the nar-

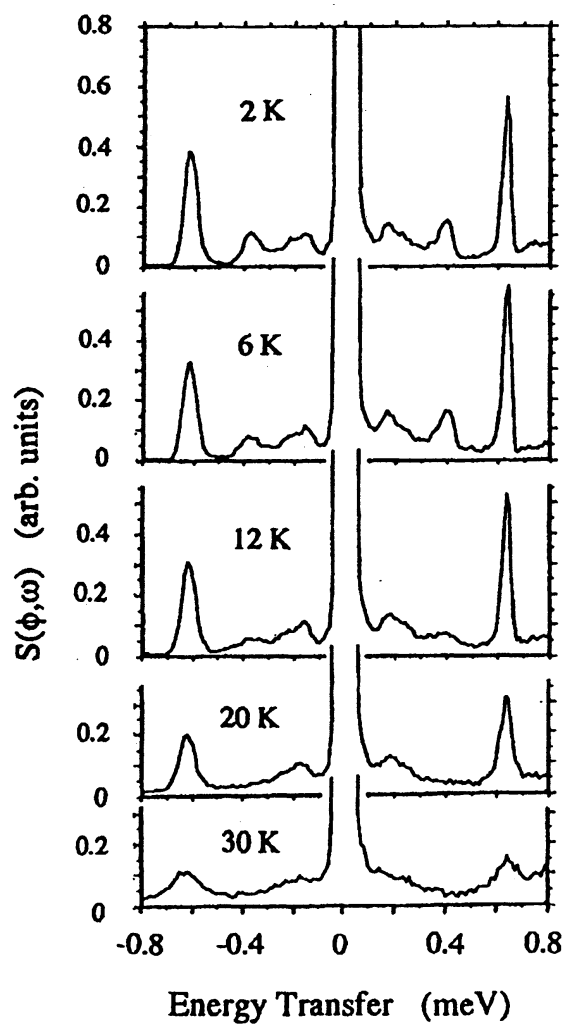


Figure 4.30: Low-temperature INS spectra of complex I (toluene guest). Figure adapted from Ref.[56].

row component of the spectral density functions in sample **I**; presumably, the narrow spectral density component that has been observed and characterised from NMR experiments is an average of the components which give rise to the broad features in the INS spectra. The distinct methyl-group environments may be linked to the two-fold disorder of the aromatic ring observed in XRD measurements.

The characterisation of the methyl-group dynamics in the calixarene/ γ -picoline sample (**II**) is less well defined, and the experiments have raised some interesting observations. Previous INS measurements have indicated the presence of almost-free methyl rotors, an observation that is supported by the NMR measurements reported in section 4.5. However, this contradicts the INS spectra acquired from the sample studied by NMR, which indicates the presence of a single environment in which the methyl-group rotation is more hindered. An adequate description of the temperature dependence of T_1 is possible, for $T < \theta_{\min}$, by assuming the presence of both of these components.

It is very clear however, that at low temperatures, the proton spin-relaxation in the calixarene complexes studied is not solely dictated by methyl-group rotation. The disparity between the experimental data and the predicted T_1 -inverse temperature curves at $T > \theta_{\min}$ for sample **II** (figure 4.15) is perhaps the most convincing evidence for the existence of an additional motional process that contributes to proton spin-lattice relaxation. This motion is also probably responsible for the very broad and shallow T_1 -inverse temperature curves observed in the other calixarene complexes. Although the nature of this motion is as yet undetermined, its effect is only revealed by field-cycling NMR, and cannot be predicted from INS measurements.

The experiments presented in this chapter clearly demonstrate that, at cryogenic temperatures, the spin-lattice relaxation of protons within this class of complexes are affected by the thermal treatment. Proton T_1 values measured in samples that are cooled quickly from room temperature are consistently shorter than T_1 measured in slowly cooled samples. The difference has been attributed to the level of structural disorder present in the sample. Presumably, quick cooling ‘freezes-in’ metastable configurations of the crystal lattice, which gives rise to highly mobile, unhindered molecular moieties.

Thermal history effects have also been observed in complementary NMR measurements carried out by the University of Southampton group. ¹³C spectra of sample **VII** were acquired via proton-decoupled MAS-NMR [46]. Using this method the dipolar broadening is averaged out by physical spinning of the sample at the magic angle, and the heteronuclear *J*-coupling is eliminated by applying an RF field at the proton Larmor frequency, during the acquisition of the ¹³C FID [44].

The room temperature spectrum (not shown) displays narrow lines; many of the lines broaden at lower temperatures as the effect of motional narrowing decreases. Figure 4.31 shows how the spectrum responded to different cooling protocols. The peaks exhibit broader line widths in the quickly

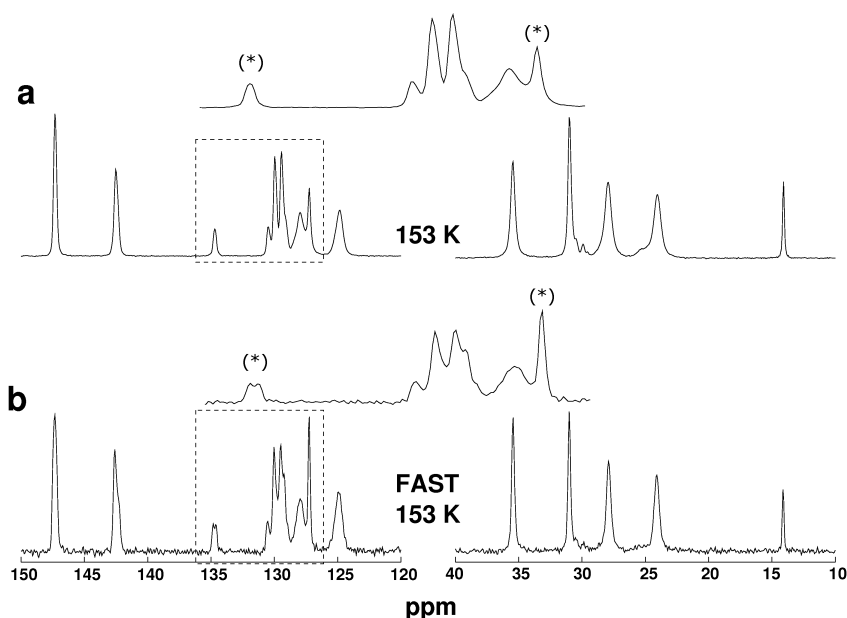


Figure 4.31: Proton-decoupled ¹³C MAS-NMR spectra of sample **VII** (*p*-xylene guest); (a) slowly cooled to 153K from room temperature over 12 hours; (b) quench-cooled to 153K from room temperature over 3 minutes. Spectra recorded at 9.4T, with a sample rotation frequency of 10.0kHz. Region most affected by different cooling procedures is enlarged. Asterisks denote carbon nuclei that belong to the *p*-xylene guest molecule [46].

cooled sample (figure 4.31b), and there are visible shoulders on many of the peaks. The peak at 135ppm has been assigned to the carbon atoms in the *p*-xylene molecule that are bonded to the methyl groups. Peaks assigned to carbon atoms in the host molecule also exhibit splitting upon quick cooling.

The comparatively broad peaks and increased peak splitting in the quickly cooled sample is consistent with the observations from the relaxometry measurements, which suggest that cooling the sample quickly freezes disorder into the structure, thereby preventing the guest molecules to explore the potential energy surface and settling into the configuration of lowest energy.

The thermal history effect described here has implications for the experimental protocol for NMR studies of large biomolecules at cryogenic temperatures. A similar effect is expected to be observed in such molecules, due to their size and complexity. If this is found to be the case, then disordered configurations may be preferential due to the increase in relaxation efficiency. Shorter T_1 would result in shorter experimental times thereby making NMR experiments, in which many transients are collected and averaged in order to increase signal-to-noise, much more practical.

The measurements presented in this chapter have explored the possibility of such complexes being used as cryorelaxors in cryoMAS experiments. The target operational temperature for cryoMAS, limited by the technical challenges associated with stable rotation of the sample rotor, is around 20K. It is desirable for a cryorelaxor to have a T_1 minimum, or at least a small value of T_1 (~ 1 s), at this temperature and at the operational field of the cryoMAS experiments (likely to be larger than the greatest field explored in this work). None of the calixarene complexes studied here appear to satisfy these criteria, with the exception perhaps of sample **VII** in the quench cooled state. The calculation of the dipolar coupling constant in section 4.6.2 suggests that although gains may be made from further deuteration of the complexes, these will be limited. Rather than the proximity of protons to relaxation centres, it is the number of protons which dominates the value of C_{tot} , and deuteration of the *tert*-butyl groups is the single largest substitution of protons possible in these complexes.

Currently, complexes of molecular hydrogen trapped in fullerene cages appear to display more promise in the context of application as cryorelaxors [15].

Chapter 5

Quantum rotation and translation of endohedral hydrogen confined within a fullerene cage

Molecular hydrogen confined inside a fullerene cavity provides an extremely interesting system in which quantum mechanical motion may be studied [40, 15, 59]. Confinement within the fullerene cavity results in quantisation of the translational motion; the rotational motion is also quantised. The energies of these excitations and the large scattering cross-section of hydrogen make this system well suited to study by inelastic neutron scattering (INS). Also, unlike NMR, INS is able to directly probe the spin-dependent transitions between *para*- and *ortho*hydrogen (parahydrogen is a spin-0 species, and is therefore NMR silent). NMR and INS are alike in that they are both sensitive to the changes in spin that accompany changes in *para*- and *ortho*states— however the splitting is on the energy scale of INS whereas it is too large for NMR.

Results from INS experiments on an endohedral hydrogen-fullerene complex, performed using the IN4 spectrometer at ILL, Grenoble, France (see section 3.2 for details), are presented in this chapter.

5.1 Structure

The complex studied was an inclusion complex of molecular hydrogen in an open cage fullerene, namely aza-thia-open-cage-fullerene (ATO CF) (figure 5.1). This complex, referred to as H₂@ATO CF, is an intermediate in the synthesis of a complex of molecular hydrogen incarcerated in C₆₀ (H₂@C₆₀). In order to insert molecular hydrogen into a fullerene cavity, it is necessary to first create an opening in the fullerene by chemical reaction, before the hydrogen can be inserted. After insertion of the hydrogen at high pressure [13], the opening can be closed by performing several further reactions. This synthesis process is referred to as ‘molecular surgery’ [14][12].

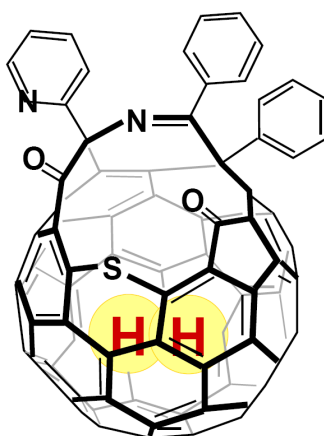


Figure 5.1: Sketch of H₂@ATO CF complex. The exohedral protons of the aromatic groups around the orifice contribute to the neutron scattering spectra. The contribution can be removed by taking the difference spectrum of H₂@ATO CF and ATO CF, which leaves just the spectrum of the endohedral hydrogen molecule.

In ATO CF the presence of the orifice causes the spherical symmetry of the fullerene cage to be broken. The cavity can be approximated as a scalene ellipsoid, i.e. the three orthogonal diameters that describe the ellipsoid each have unique values. The ellipsoid diameters, from the crystal structure determined by x-ray diffraction, are $d_x^C \approx 7.00\text{\AA}$, $d_y^C \approx 7.35\text{\AA}$ and $d_z^C \approx 7.70\text{\AA}$. The longest axis, which runs through the centre of the ellipsoid and points towards the orifice, is defined as the z -axis. The x and y -axes are coincident with the semi-minor and semi-major axes, respectively, of the ellipse that describes the fullerene skeleton ‘equator’.

For the purposes of analysis it is useful to approximate the ellipsoidal

cavity as a spherical box with well defined edges. In this case the effective spherical radius that the endohedral hydrogen molecule is confined to is given by [40]

$$r_{\text{eff}} = \frac{1}{2}d_{\text{rms}} - r_{\text{H}} - r_{\text{C}} = 0.777\text{\AA} , \quad (5.1)$$

where $d_{\text{rms}} = \sqrt{\frac{1}{3}[(d_x^{\text{C}})^2 + (d_y^{\text{C}})^2 + (d_z^{\text{C}})^2]}$ is the root-mean-square diameter of the fullerene cavity. $r_{\text{H}} = 1.20\text{\AA}$ and $r_{\text{C}} = 1.70\text{\AA}$ are the van der Waals radii of hydrogen and carbon, respectively.

5.2 Energy level diagram

The Hamiltonian for the quantum motion of confined molecular hydrogen was introduced in section 2.5, equation (2.72). The spatial states of the confined molecule are describable by five quantum numbers; the rotational quantum numbers $\{J, m_J\}$ and the translational quantum numbers $\{n, l, m_l\}$.

The rotational eigenstates of confined H₂ are expected to be close to those of H₂ gas i.e.

$$E_J = B_J J(J + 1) . \quad (5.2)$$

According to this, the rotational splitting $\Delta_{\text{rot}} \cong 172\text{K}$ (14.8meV), so it can be assumed that only the two lowest rotational states are populated at the temperatures explored in this investigation (i.e. 2.5–110K). At low temperatures, and thermal equilibrium, all of the hydrogen is expected to be in the $J = 0$ parahydrogen state. However a metastable population of orthohydrogen will persist if there are no spin-dependent interactions facilitating ortho-to-parahydrogen conversion. The low-temperature stability of orthohydrogen in ATOCF has been previously verified via investigation by solid-state NMR [40].

In a perfectly spherical rotational potential, the H₂ rotational levels have a g_J -fold degeneracy, where $g_J = 2J + 1$. In the cavity of ATOCF the spherical symmetry is broken, which causes the H₂ molecule to experience a non-isotropic rotational potential. This lifts the degeneracy of the excited rotational levels, and splitting of these levels is expected to be observed in the INS spectra (figure 5.2(b)).

The translational splitting of the confined H₂ molecule can be estimated by approximating the molecule as a single spherical particle, and treating

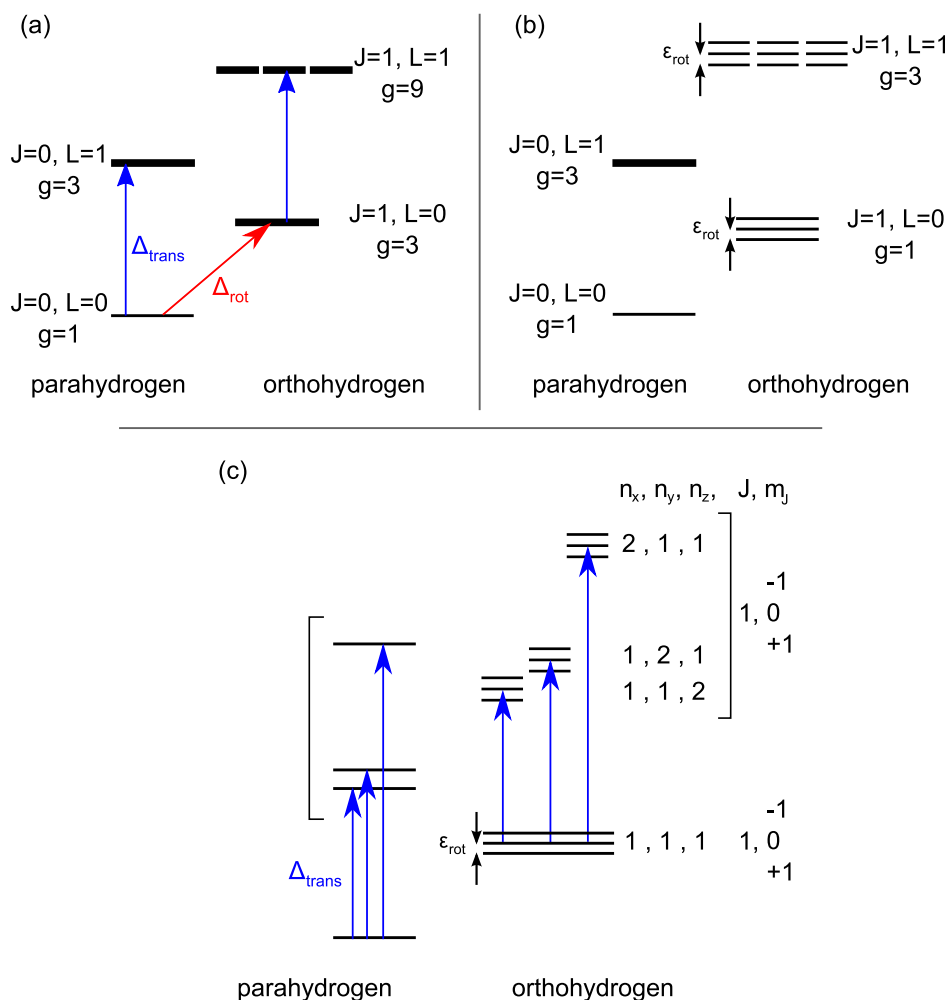


Figure 5.2: (a) Energy level diagram for H₂ molecule encapsulated in perfectly spherical cavity. Spatial states described by the quantum number $\{J, m_J, n, L, m_L\}$, and g is the degeneracy; (b) Degeneracy of rotational sub-levels of orthohydrogen lifted due to non-isotropic rotational potential; (c) Degeneracy of translational sub-levels lifted due to cavity elongation. Orbital angular momentum is quenched and translational states are denoted by $\{n_x, n_y, n_z\}$, where the subscript denotes the principal axis of the cavity along which the translational state is polarised.

it as a particle in a spherical box [60], of radius r_{eff} . The eigenfunctions that satisfy the three-dimensional Schrödinger equation can be found by the separation of variables method, and the resulting eigenfunctions and eigenvalues are

$$\psi_{\text{trans}}^{(l,m)}(r, \theta, \phi) = A j_l(kr) Y_l^{m_l}(\theta, \phi) \quad (5.3)$$

$$E_{\text{trans}}^{(n,l)} = \frac{\beta_{n,l}^2 \hbar^2}{2\mu r_{\text{eff}}^2}, \quad (5.4)$$

where A is a normalisation constant, and $k = \frac{\sqrt{2\mu E}}{\hbar}$. $\beta_{n,l}$ is the n^{th} root of $j_l(kr)$, the l^{th} order spherical Bessel function. Using this approximation, the translational splitting $\Delta_{\text{trans}} \cong 200\text{K}$ (17meV). Based on this estimated splitting and the temperature range of our measurements, all but the two lowest translational states are neglected.

As with the rotational energy levels, the broken spherical symmetry of the ATOCF cavity has implications for the degeneracy of excited translational states. The symmetry lowering lifts the three-fold degeneracy of the translational excited state (degeneracy $g_l = 2l + 1$). This has the effect of quenching the orbital angular momentum of the confined H₂ molecule [61][40]. In this case, translational motion of the molecule in the ellipsoidal cavity is analogous to a particle in a rectangular box and the translational spatial states are denoted by $\{n_x, n_y, n_z\}$ (figure 5.2(c)) [62]. The translational states are real spatial states that represent the translational motion of the molecule along the orthogonal principal axes of the ellipsoidal cavity.

5.3 INS Results

In order to isolate the INS spectrum of the endohedral hydrogen molecule it is necessary to remove any contributions due to scattering from exohedral hydrogen atoms (the protons attached to the aromatic groups at the orifice). This was achieved by acquiring a spectrum from a sample of ATOCF with an unoccupied cavity ('empty cage'), and subtracting this from the spectrum of H₂@ATOFCF. The remaining difference spectrum is due to transitions of H₂ molecules. The difference spectrum is also free of contributions from vibrational modes of the fullerene cage.

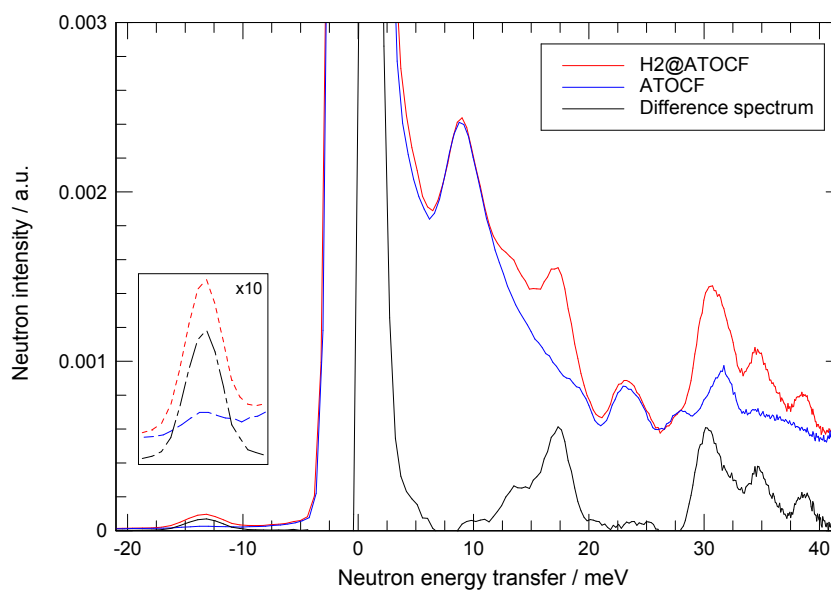


Figure 5.3: INS spectra, and difference spectrum, for H₂@ATOCF and ‘empty cage’ ATOCF; $\lambda = 1.24\text{\AA}$, $T = 2.5\text{K}$. The ATOCF spectrum has been scaled appropriately, in order to account for the difference in mass between each sample. Inset shows ortho- to parahydrogen transition peak enlarged for clarity.

Scaling of the ATOCF spectra was necessary due to the larger mass of sample available (510mg, compared to 492mg of H₂@ATOFCF). The difference in sample mass and slight differences of the orientation of the sample with respect to the beam contribute to the difference in intensity of the spectra, hence the need for scaling.

Figure 5.3 shows the spectra collected at $T = 2.5\text{K}$, neutron wavelength $\lambda = 1.24\text{\AA}$. The energy axis shows neutron energy transferred *to* the sample; by this convention, energy > 0 corresponds to neutron energy lost, and energy < 0 corresponds to neutron energy gained. The peak at -13.3meV can immediately be identified as the ortho-para transition ($J = 1 \rightarrow 0$) of the endohedral hydrogen. At 2.5K the only possible excited state that may impart energy to a neutron is the metastable population of orthohydrogen. An equivalent peak is observed at $+13.3\text{meV}$, corresponding to the $J = 0 \rightarrow 1$ transition. In H₂ gas this transition is expected to be 14.8meV . The difference suggests that the rotation of the endohedral hydrogen molecule is coupled to other degrees of freedom.

Figure 5.4 shows the difference spectrum in the -17 - 20meV energy range, acquired with greater resolution at $\lambda = 1.8\text{\AA}$. In this configuration, the energy resolution of the spectrometer was 0.8meV FWHM at the elastic peak. The spectrum clearly reveals some underlying structure to the peaks observed in the $\lambda = 1.24\text{\AA}$ spectrum (figure 5.3). The spectrum in the 12 - 20meV energy range can be simulated with five Gaussian functions, which can apparently be grouped into a triplet and a doublet of peaks that have a similar amplitude. The triplet has peaks centred at 13.3meV , 14.7meV and 16.1meV . The similar amplitudes and uniform splitting (1.4meV) indicate that these peaks belong to the same manifold. They are strong candidates for the $J = 0 \rightarrow 1$ rotational transitions from the translational ground state of parahydrogen $\{0, 0, 1, 1, 1\}$ to the translational ground state of orthohydrogen $\{1, m_J, 1, 1, 1\}$, which is rendered non-degenerate due to the non-isotropic rotational potential.

The broad feature centred about 17.5meV is well simulated by fitting it to two Gaussian functions at 17.1meV and 17.9meV . The positions of these peaks are similar to the estimated translational splitting predicted by the single particle in a spherical box approximation, $\Delta_{\text{trans}} \cong 17\text{meV}$ (section 5.2). The excited translational states are expected to be non-degenerate due to elongation of the fullerene cavity, therefore the peaks at 17.1meV and

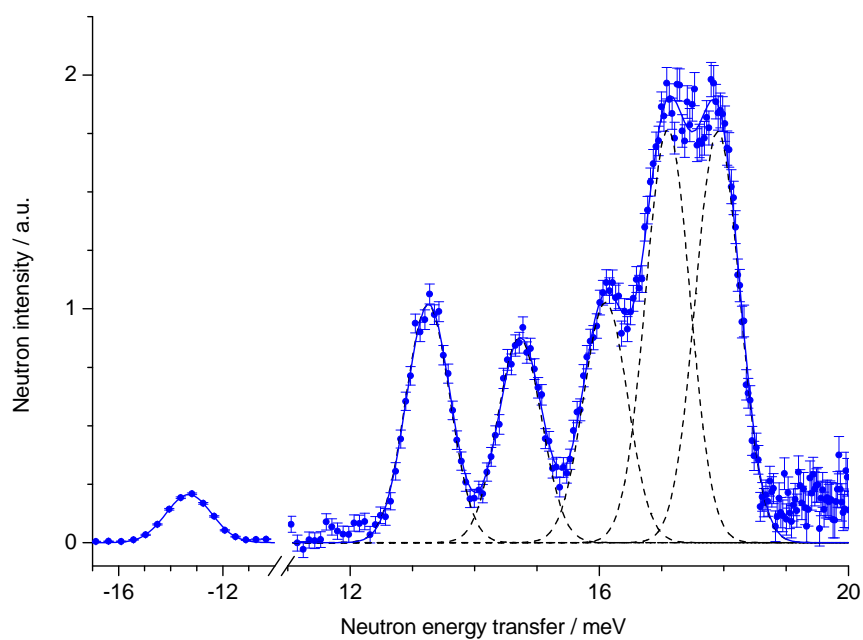


Figure 5.4: Difference spectrum, $\lambda = 1.8\text{\AA}$, $T = 2.5\text{K}$, 11–20meV. Triplet of rotational sub-levels can be clearly seen at 13.3meV, 14.7meV and 16.1meV. Doublet centred around 17.5meV due to translational transitions.

17.9meV are most likely due to translational transitions, from the ground state of orthohydrogen into the two lowest excited states. Assuming that translation along the longest axis of the cavity is the energetically most favourable direction, the peaks at 17.1 and 17.9meV can be assigned to transitions to the $\{1, 1, 2\}$ and $\{1, 2, 1\}$ translational states.

The translational excitations in parahydrogen are not expected to contribute to the INS spectrum. The scattering functions for transitions into the excited translational states of para- and orthohydrogen are proportional to the respective form factors [34]

$$\begin{aligned} F_{\text{para}}^{0 \rightarrow 1} &= 4[b_{\text{inc}} j_0(Qd_{\text{HH}}/2)]^2 \\ F_{\text{ortho}}^{0 \rightarrow 1} &= 4[b_{\text{coh}}^2 + \frac{2}{3}b_{\text{inc}}^2][2j_2(Qd_{\text{HH}}/2)^2 + j_0(Qd_{\text{HH}}/2)^2], \end{aligned} \quad (5.5)$$

where j_l is the l^{th} order spherical Bessel function, Q is the momentum transfer defined by equation (2.59), $d_{\text{HH}} = 0.74\text{\AA}$ is the inter-proton distance in H₂, and b_{inc} and b_{coh} are the incoherent and coherent scattering lengths, respectively. The scattering function for the translational excitation in parahydrogen is proportional to b_{coh}^2 , and for orthohydrogen, the scattering function is proportional to $(b_{\text{coh}}^2 + b_{\text{inc}}^2)$. b_{coh}^2 is smaller than b_{inc}^2 by a factor of 45, therefore the translational excitations of parahydrogen do not make a significant contribution to the INS spectrum.

5.3.1 Temperature dependence of rotational sub-levels

The population of the rotational sub-levels was investigated by acquiring spectra over a range of temperatures, and focusing on the neutron energy gained side of the spectrum. The spectra in figure 5.5 were acquired at $\lambda = 3.6\text{\AA}$, between $T = 2.5\text{K}$ and $T = 110\text{K}$. Up to and including $T = 30\text{K}$ the spectra for H₂@ATOFCF were suitably clear so that subtracting the ATOFCF spectra was not necessary. Above 30K subtraction was required due to interference from the quasi-elastic peak, and other temperature dependent features not associated with endohedral hydrogen motion.

At the lowest temperature only one peak is observed at -13.2meV . With increasing temperature the amplitude of the -13.2meV peak decreases, and other peaks at higher energy appear and grow in amplitude. At 110K all peaks have a similar amplitude.

Up to and including 40K the spectra were fitted to three Gaussian func-

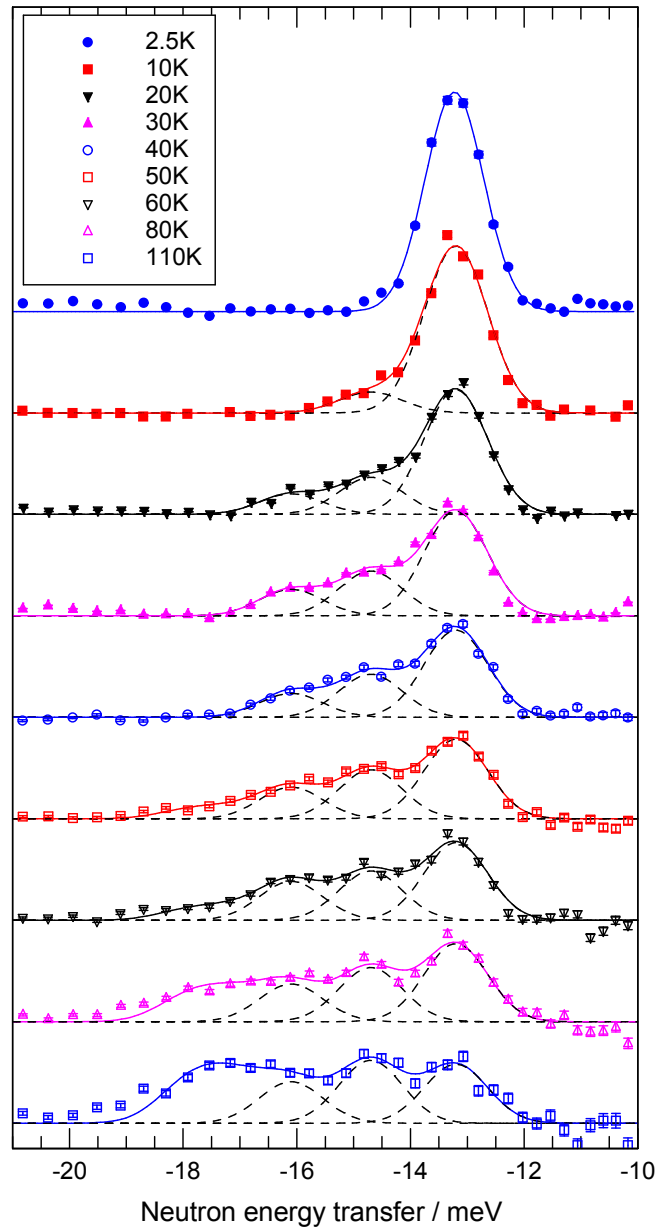


Figure 5.5: Temperature dependence of rotational sub-level peaks at -13.2meV , -14.7meV , and -16.1meV (dashed lines), $\lambda = 3.6\text{\AA}$. Solid lines are results of fitting spectra with up to 5 Gaussian functions, with fixed width and position. Filled symbols denote H₂@ATOCF spectra, corrected for sloping background; open symbols denote difference spectra.

tions, with the widths constrained to the instrument resolution (1.32meV FWHM), and the positions fixed to the positions of the rotational peaks on the neutron energy lost side of the spectrum.

Above 40K, a broader feature emerges at higher energy. This was identified as the doublet at 17.5meV, the transition from the first excited translational state of orthohydrogen to the ground state. Peaks at 17.1meV and 17.9meV were included in the fit. It was necessary to fix the amplitudes of the two translational peaks to be equal to each other, in order to sensibly fit the high temperature spectra.

The peak amplitudes reflect the populations of the rotational sub-levels and excited translational states of orthohydrogen. The spectra clearly show the higher rotational sub-levels of the translational ground state of orthohydrogen ($\{J, m_J\} = \{1, 0\}$ and $\{1, -1\}$) becoming occupied as the temperature increases. The amplitudes of the rotational peaks were normalised, and in figure 5.6 the relative amplitudes are plotted as a function of temperature (filled symbols). Also plotted (solid lines) is the relative occupancy of each

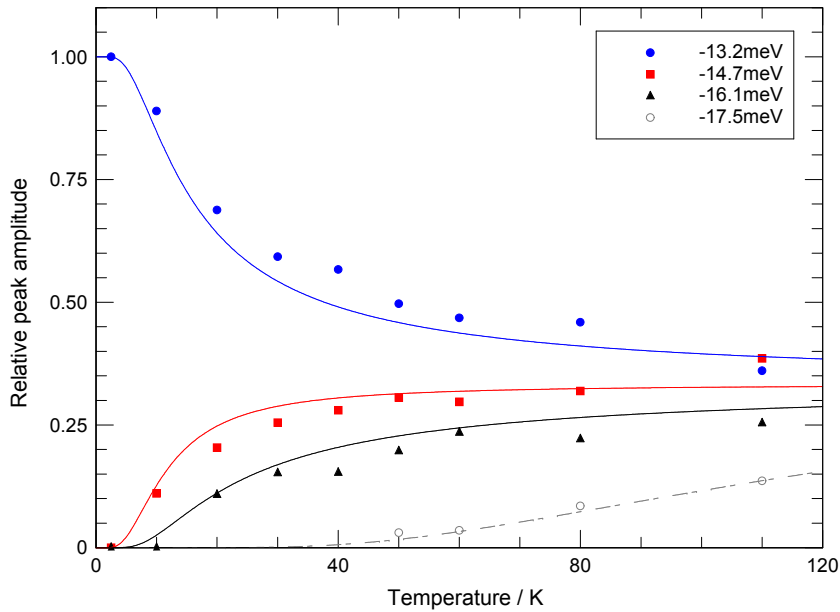


Figure 5.6: Relative peak amplitude of rotational sub-level triplet as a function of temperature. The relative amplitude reflects the relative population of each energy level. The populations closely follow a Boltzmann distribution (solid lines).

sub-level, n_i , as predicted by the Boltzmann distribution,

$$n_i = \frac{e^{-E_i/k_B T}}{Z(T)}, \quad (5.6)$$

where $E_{(1,2,3)} = \{13.2, 14.7, 16.1\}$ meV, and $Z(T)$ is the partition function of the three-level system. There is a strong agreement between the peak amplitudes and the Boltzmann model. This shows that among the rotational sub-levels of the translational ground state of orthohydrogen (itself a thermodynamically metastable state) a thermal equilibrium is maintained.

The dashed line on figure 5.6 is the relative occupancy of the excited state of a two-level system, separated by 17.5meV, as predicted by the Boltzmann distribution. The relative amplitudes of the 17.1 and 17.9meV peaks (empty circles) follow the predicted population fairly closely. It should be noted that normalisation of the amplitudes of these peaks was not possible, so the amplitudes were scaled by choosing an appropriate scaling factor.

Figure 5.6 shows that the states that give rise to the triplet of peaks at 13.2, 14.7 and 16.1meV are populated with an activation energy of ~ 1.5 meV, corresponding to the splitting of the rotational sub-levels ϵ_{rot} , whereas the peaks at 17.1 and 17.9meV belong to a different manifold, with an activation energy of ~ 17.5 meV, which corresponds to the translational splitting Δ_{trans} . The peak assignment is shown pictorially in figure 5.7.

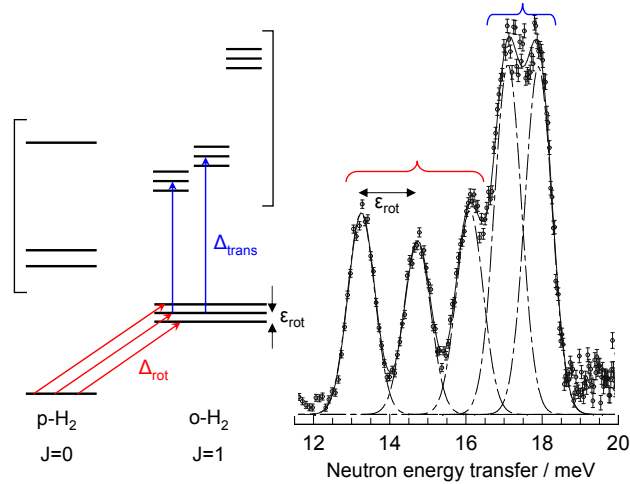


Figure 5.7: Assignment of peaks observed between 10 and 20meV, $\lambda = 1.8\text{\AA}$. Reverse transitions apply for peaks observed on opposite side of spectrum at higher temperatures.

5.3.2 Calculation of the rotational potential

The deformation of the spherical fullerene skeleton causes the endohedral hydrogen molecule to experience an anisotropic rotational potential. The results from preceding sections confirm that the anisotropy leads to splitting of the ground translational state of orthohydrogen. Given the magnitude of the splittings, as measured by the INS spectra, it is possible to determine the rotational potential.

The potential can be expressed as a Cartesian tensor, which is diagonal in the principal axis system. It is assumed that the principal axis of the lowest principal value of the tensor corresponds to the most elongated direction of the fullerene cage. Rotation in the plane parallel to this axis is expected to be relatively unhindered.

The internuclear unit-vector of the endohedral hydrogen molecule, with respect to the principal axis of the rotational potential $\{XYZ\}$, is expressed as

$$\mathbf{e}_{\text{HH}} = \mathbf{e}_X \sin \theta \cos \phi + \mathbf{e}_Y \sin \theta \sin \phi + \mathbf{e}_Z \cos \theta, \quad (5.7)$$

using spherical polar co-ordinates. The rotational potential can therefore be written

$$V(\theta, \phi) = V_X[1 - (\sin \theta \cos \phi)^2] + V_Y[1 - (\sin \theta \sin \phi)^2] + V_Z[1 - (\cos \theta)^2], \quad (5.8)$$

where V_X , V_Y and V_Z are the principal values of the rotational tensor, which represent the magnitudes of the respective rotational barriers. The two-fold symmetry of the barriers reflects the two-fold symmetry of the hydrogen molecule.

Suitable values for the barrier heights were found by numerically solving the rotational Hamiltonian $\hat{\mathbf{H}}_{\mathbf{R}} = \frac{\hbar^2}{B_J} \hat{L}^2 + \hat{V}(\theta, \phi)$ in the basis of the free-rotor functions (i.e. the spherical harmonic functions). The values of V_X , V_Y and V_Z were systematically varied in order to find eigenvalues that gave rise to the $J = 0 \leftrightarrow 1$ energy transfers observed experimentally $\{13.2, 14.7, 16.1\text{meV}\}$. Good agreement with these values was achieved with $V_X = 3.58$, $V_Y = -3.46$, and $V_Z = -0.12\text{meV}$. There is some coupling between the $J = 0$ and $J = 2$ states that results in the eigenvalue of the former state to be modified by -0.075meV . The resultant $J = 0 \leftrightarrow 1$ energy transfer are $\{13.38, 14.86, 16.20\text{meV}\}$.

The values of the potential barriers listed above agree very closely with the rotational splitting of the $\{J = 1, L = 0\}$ state observed experimentally. Each transition energy calculated is systematically larger than the experimental values, however the offset is comparable to the offset between the centre of the elastic peak in the difference spectrum and $\hbar\omega = 0$.

5.3.3 Q -dependence of rotational and translational peaks

The incoherent scattering function S_{inc} (equation (2.70)) is a function of energy and Q , the momentum transfer. The form of $S_{inc}(Q)$ is dependent on the nature of the transition, and so by examining the intensity of a INS peak as a function of Q , the origin of the peak may be assigned. Analysis of the Q -dependence can also give details of the size of the cavity in which the molecule is trapped.

The scattering functions due to translational and rotational transitions of molecular hydrogen in the interstitial sites of solid C₆₀ have been formulated by Yildirim and Harris [37]. Despite the differences in the cavity geometry, the same scattering functions can be applied to hydrogen trapped in a fullerene cage.

Rotational transitions

The powder averages of the scattering functions for purely rotational transitions are proportional to the amplitude factors A and B , which correspond to the $J = 0 \rightarrow 1$ and $J = 1 \rightarrow 0$ transitions, respectively: [37]

$$\begin{aligned} A &= \frac{3}{4} \exp(-\frac{2}{3}Q^2\langle u^2 \rangle) [b_{inc}j_1(Qd_{HH}/2)]^2 \\ B &= \frac{1}{4} \exp(-\frac{2}{3}Q^2\langle u^2 \rangle) [b_{inc}j_1(Qd_{HH}/2)]^2, \end{aligned} \quad (5.9)$$

where $\langle u^2 \rangle$ is the mean squared displacement of the hydrogen molecule.

The Q -dependence of the ortho- to parahydrogen conversion peak at -13.2meV is shown in figure 5.8, for three neutron wavelengths, giving access to a range of Q from 1.4\AA^{-1} to 10\AA^{-1} . The data were combined and fitted to equation (5.9), giving a remarkably good fit with $\langle u^2 \rangle = 0.067 \pm 0.001\text{\AA}^2$.

In figure 5.9 the Q -dependences of the individual peaks observed at 13.2, 14.7 and 16.1meV on the high resolution $\lambda = 1.8\text{\AA}$, $T = 2.5\text{K}$ spectrum are plotted, along with the Q -dependence of the 11–15meV region of the lower resolution $\lambda = 1.24\text{\AA}$ spectrum, acquired at the same temperature.

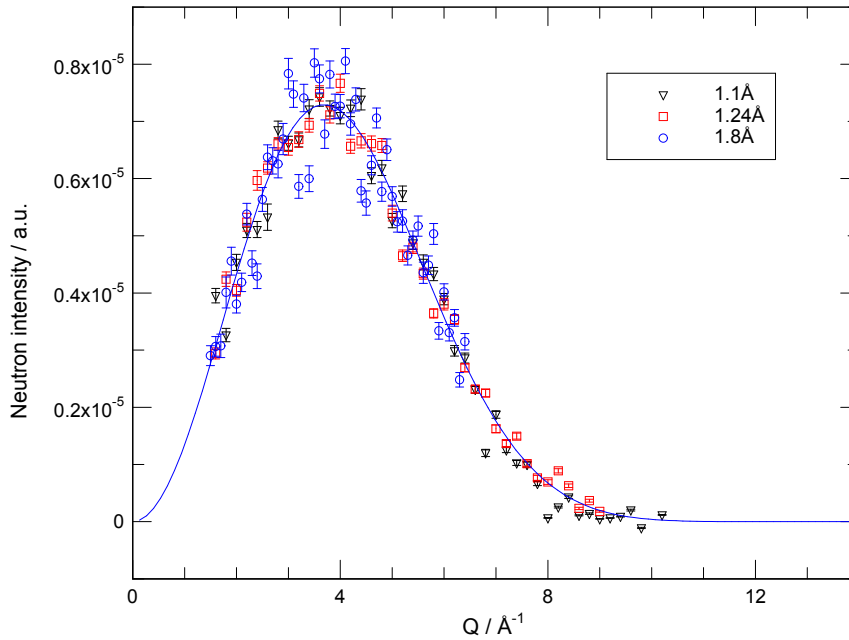


Figure 5.8: Q -dependence of ortho- to para-hydrogen conversion peak at -13.2meV . All data points fitted to equation (5.9). Mean squared displacement $\langle u^2 \rangle = 0.067 \pm 0.001\text{\AA}^2$ from fit (solid line).

The latter energy window was chosen so as to avoid any contribution from the translational peaks at 17.1 and 17.9meV . The limited Q -range of the $\lambda = 1.8\text{\AA}$ data, and the scatter due to the limited resolution of the $\lambda = 1.24\text{\AA}$ spectrum ensure that this data does not give a consistent, reasonable fit to equation (5.9). However there is qualitative agreement between the data and the expression for the Q -dependence of rotational peaks with $\langle u^2 \rangle = 0.067\text{\AA}^2$ (fig. 5.9, solid line).

Translational transitions

The powder average of the scattering function for the transition from the ground to the first excited translational state in orthohydrogen is proportional to the amplitude factor [37] I_{trans} , where

$$I_{\text{trans}} = \frac{1}{2} b_{\text{inc}}^2 Q^2 \langle u^2 \rangle \exp(-2W) \left\{ \frac{1}{3} [j_0(Qd_{\text{HH}}/2)]^2 + \frac{2}{3} [j_2(Qd_{\text{HH}}/2)]^2 \right\}. \quad (5.10)$$

In this expression W is the Debye-Waller factor, given by $\frac{1}{3} Q^2 \langle u^2 \rangle$.

Figure 5.10 shows the Q -dependence of the peak doublet centred around

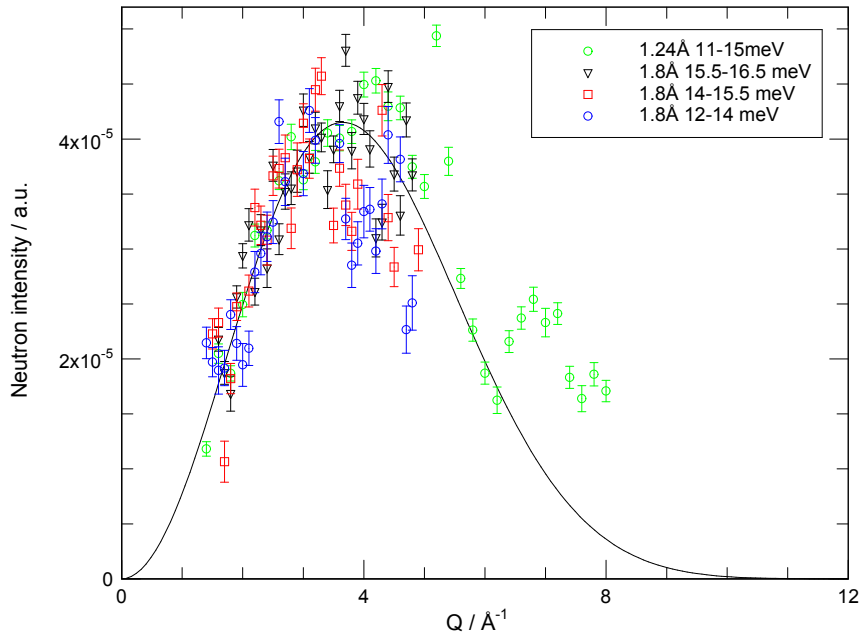


Figure 5.9: Q -dependence of rotational peaks observed on neutron energy lost side of spectra acquired at $\lambda = 1.24$ and 1.8 \AA , $T = 2.5 \text{ K}$. Solid line shows expected Q -dependence of a peak of rotational origin with $\langle u^2 \rangle = 0.067 \text{ \AA}^2$.

+17.5 meV. On first inspection there appears to be little qualitative difference between the shapes of the curves in this figure and those in figure 5.8. Indeed, fitting the +17.5 meV data to the expression for the Q -dependence of a rotational transition (equation (5.9)) appears to give a decent fit (dashed line, figure 5.10). However, fitting the data to equation (5.10) gives a much improved fit, with $\langle u^2 \rangle = 0.068 \text{ \AA}^2$, which agrees very well with the value from fits of the rotational peak at -13.2 meV .

In particular, the peaks at 17.1 and 17.9 meV haven been assigned to excitations from the translational ground state of orthohydrogen to the $\{1, 1, 2\}$ and $\{1, 2, 1\}$ states, respectively, in the first excited translational state (see sections 5.3 and 5.3.1). The peak due to transitions into the $\{2, 1, 1\}$ state has not been identified so far. This peak may be identified by examining the Q -dependence of candidate peaks.

Figure 5.11 displays the 10 to 45 meV region of the $\lambda = 1.24 \text{ \AA}$, $T = 2.5 \text{ K}$ spectrum. The features between 10 and 20 meV we recognise as the rotational sublevel triplet (broad peak centred at 14 meV), and the excitations into the $\{1, 1, 2\}$ and $\{1, 2, 1\}$ translational states (peak at 17.5 meV). The

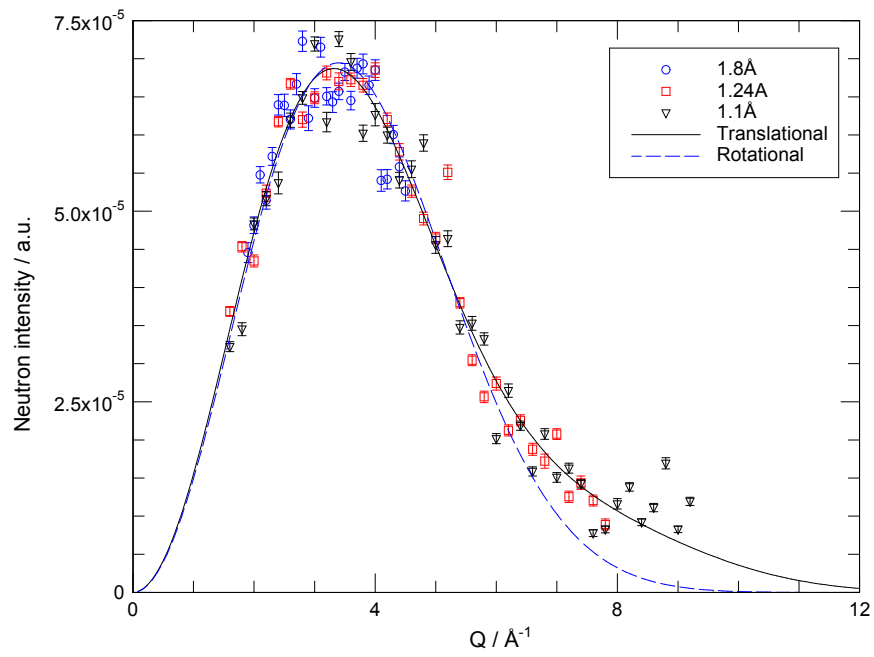


Figure 5.10: Q -dependence of translational peak doublet at 17.5 meV. All data points fitted to expressions for Q -dependence of translational (solid line, $\langle u^2 \rangle = 0.068 \pm 0.001 \text{ \AA}^2$) and rotational transitions (dashed line).

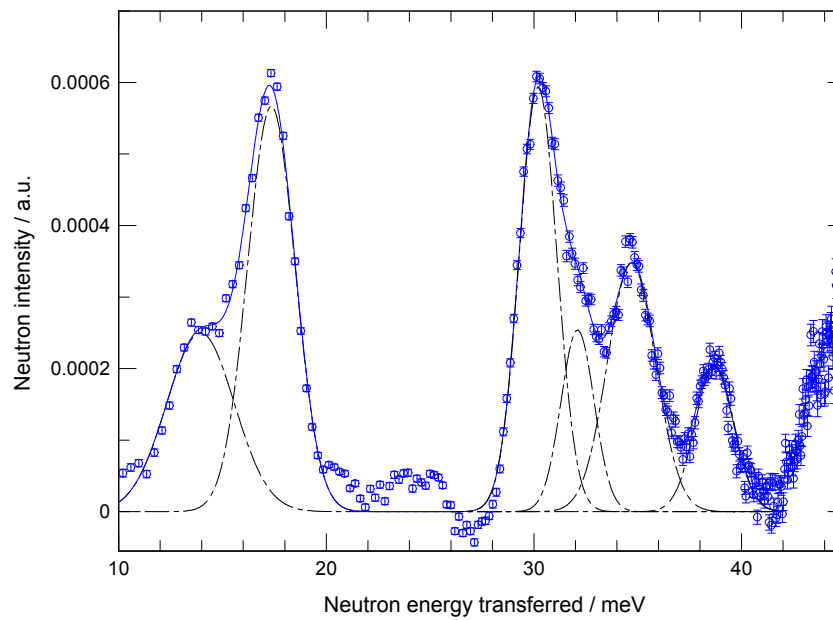


Figure 5.11: Difference spectrum, $\lambda = 1.24 \text{ \AA}$, $T = 2.5 \text{ K}$, 10–45 meV.

region between 20 and 28meV is featureless; the peak corresponding to transitions into the $\{2, 1, 1\}$ state is therefore likely to be among the group of peaks observed between 28 and 40meV. This part of the spectrum can be simulated fairly well by fitting it to four Gaussian peaks of variable widths between 1.9meV and 2.7meV FWHM.

Figure 5.12 shows the Q -dependence of the peak at 30.2meV. In figure 5.13 the Q -dependence of the peaks observed at higher energy are plotted. For the sake of comparison, the Q -dependence of the translational lines at ~ 17 meV is included on both figures. The Q -dependence of the 30.2meV

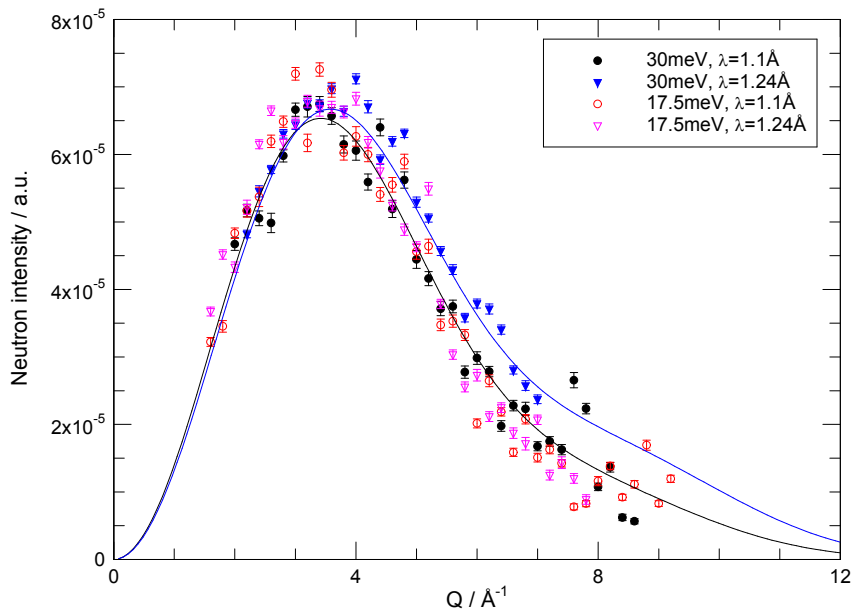


Figure 5.12: Q -dependence of peaks at 30.2meV (filled symbols) and 17.5meV (open symbols). 30.2meV data fitted to expression for translational transition (equation (5.10)). $\langle u^2 \rangle = 0.061 \pm 0.002 \text{ \AA}^2$ (black line) and $0.050 \pm 0.002 \text{ \AA}^2$ (blue line) for $\lambda = 1.1 \text{ \AA}$ and 1.24 \AA , respectively.

peak has a form that closely resembles the Q -dependence of the translational peaks. Indeed, fitting the data to the expression for the Q -dependence of a translational transition results in values of $\langle u^2 \rangle$ (see caption, fig. 5.12) that agree well with the fits of Q -dependence data from both rotational and translational peaks (figs. 5.8 and 5.10, respectively). It is therefore a strong candidate for the $\{1, m_J, 1, 1, 1\} \rightarrow \{1, m_J, 2, 1, 1\}$ excitation.

Figure 5.13 clearly illustrates the difference in Q -dependence between the

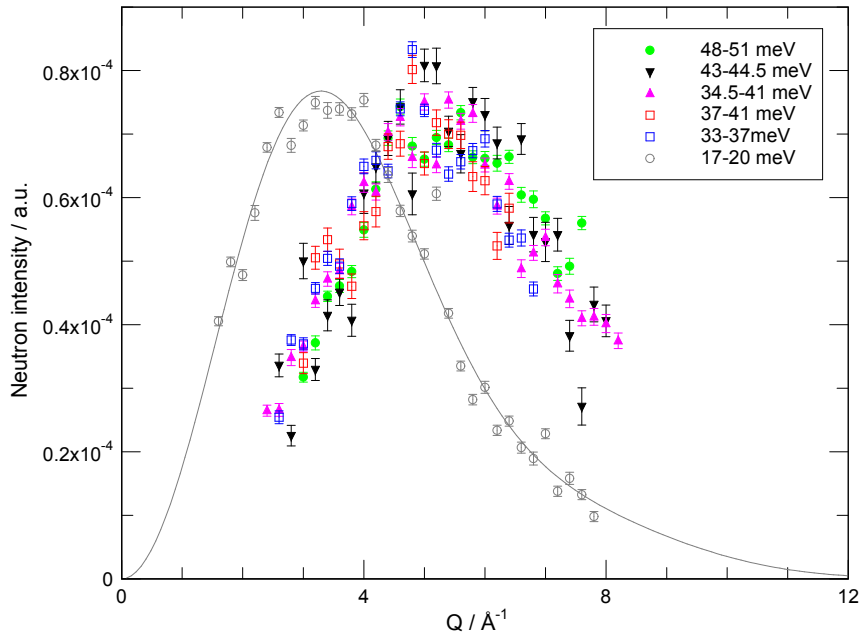


Figure 5.13: Q -dependence of unassigned peaks observed above 31meV, on spectra acquired using $\lambda = 1.1\text{\AA}$ (filled symbols) and $\lambda = 1.24\text{\AA}$ (open symbols). Q -dependence of translational doublet at 17.5meV included for comparison.

peaks observed above 33meV, and those identified as excitations between the ground and first excited translational states of orthohydrogen. The curves appear to give a good qualitative fit when fitting them to the expression for $J = 0 \rightarrow 1$ transitions, however the resultant value of $\langle u^2 \rangle$ from the fit is not reasonable. It is likely that these peaks are due to higher order transitions, for example the $J = 1 \rightarrow 2$ transition. The translational ground states of $J = 1$ orthohydrogen and $J = 2$ parahydrogen form a triplet and quintet of non-degenerate sub-levels, respectively; transitions between these states would produce a rich spectrum with many peaks.

5.4 Discussion and summary

INS measurements have shown how the quantum motion of molecular hydrogen is affected by confinement in a low-symmetry environment. The lifting of the degeneracy of translational and rotational energy levels due to the ellipsoidal shape of the fullerene cavity has been directly observed in the neutron spectra. Measurement of the splitting in the translational ground

state of orthohydrogen has allowed the anisotropic rotational potential to be characterised. The calculated principal values of the rotational potential tensor indicate that there is one axis that is almost neutral to rotation; this is presumed to be the axis aligned with the longest diameter of the ellipsoid, i.e. running through the centre of the carbon skeleton, pointing towards the orifice. The principal values are all less than half of the rotational constant of molecular hydrogen ($B_J = 7.4\text{meV}$), therefore the endohedral hydrogen is in the free-rotor limit, and tunnelling effects are minimal.

Peak assignment was aided by examining the Q -dependence of the peaks. The expressions for the Q -dependence of rotational and translational peaks have effectively only one free parameter, namely the mean squared displacement $\langle u^2 \rangle$ (the amplitude parameter has arbitrary units). Values of $\langle u^2 \rangle$ from fitting Q -dependence curves for both rotational and translational peaks are in good agreement, ranging from 0.05\AA^2 to 0.068\AA^2 .

The tenability of the values of $\langle u^2 \rangle$ determined by these experiments is supported by estimations made by approximating the endohedral hydrogen as a single particle, in a spherical box of radius r_{eff} . According to this approximation, the mean squared displacement of the molecule is given by the following:

$$\begin{aligned} \langle u^2 \rangle &= \langle \psi_{\text{trans}}^{(0)} | r^2 | \psi_{\text{trans}}^{(0)} \rangle \\ &= \frac{\int_0^{r_{\text{eff}}} r^2 |\psi_{\text{trans}}^{(0)}|^2 dr}{\int_0^{r_{\text{eff}}} |\psi_{\text{trans}}^{(0)}|^2 dr}, \end{aligned} \quad (5.11)$$

where r is the position operator, and $\psi_{\text{trans}}^{(0)}$ is the wavefunction of the endohedral hydrogen molecule. According to equation (5.3) the wavefunction of the ground state ($n = 1, l = 0$) is described by a zeroth order spherical Bessel function [60]. $\psi_{\text{trans}}^{(0)}(r)$ is scaled appropriately, so that its first root coincides with the effective radius of the fullerene cavity $r_{\text{eff}} = 0.74\text{\AA}$. Evaluation of equation (5.11) results in $\langle u^2 \rangle = 0.069\text{\AA}^2$, which is in excellent agreement with the values measured from fits of the Q -dependence data. It is worth highlighting that the calculated value of $\langle u^2 \rangle$ is remarkably similar to the value that results from fitting the ortho- to parahydrogen rotational peak at -13.2meV ($\langle u^2 \rangle = 0.067 \pm 0.001\text{\AA}^2$). This is arguably the most reliable measurement of $\langle u^2 \rangle$ due to the fact that this peak is assigned with absolutely no ambiguity, and is free from contributions of neighbouring

peaks due to its relative isolation.

The single particle approximation also lends support to the assignment of the 30.2meV peak as the $\{1, m_J, 1, 1, 1\} \rightarrow \{1, m_J, 2, 1, 1\}$ transition. The $\{2, 1, 1\}$ translational state corresponds to translation along the shortest axis of the fullerene cage, namely the x -axis. The energy of this state can be estimated by calculating the translational splitting of a single particle in a spherical box of radius $r_x = \frac{1}{2}d_x^C - r_H - r_C = 0.6\text{\AA}$. This estimation results in a translational splitting of 29.8meV, which is encouragingly similar to the position of the peak that has been assigned as the $\{2, 1, 1\}$ state.

One aspect of the quantum motion that is currently unresolved is the coupling between the translational and rotational degrees of freedom. Despite being neglected in the treatment of confined hydrogen presented in this thesis, translation-rotational coupling is certainly expected to affect the quantum dynamics. Arrelano and co-workers [63] have performed density functional theory calculations exploring the physisorption[§] of molecular hydrogen on a graphene surface. It was determined that the preferred orientation of the physisorbed molecule was with the molecular axis parallel to the graphene surface. It is likely therefore that a molecule moving towards the edge of the fullerene cage, with its molecular axis perpendicular to the carbon skeleton, will be forced to change its orientation via rotation in order to minimise its potential energy.

[§]Physisorption; Adsorption of an adsorbate to a surface, exclusively via van der Waals interactions.

Chapter 6

Summary and Concluding Remarks

In this thesis, the dynamics of guest molecules has been studied in an endohedral fullerene complex, and in a number of calixarene host-guest complexes.

Field-cycling NMR has been used to study the rotational motion of methyl-groups in calixarene complexes with *p*-xylene (sample **VII**), toluene (**I**), and γ -picoline (**II**) guest molecules. Measurements of the dispersion of T_1^{-1} have revealed the presence of crystallographically inequivalent methyl-groups in these samples. The rotational potential barriers determined by NMR measurements agree very well with the INS spectra for samples **VII** and **I**. Measurement of the temperature dependence of T_1 at range of field strengths has revealed the existence of an additional motional process that contributes to proton spin-lattice relaxation at low temperature; further work is required in order to characterise this motion, and identify its origins.

Further work will also be required in order to gain better understanding of the thermal history effects observed in the calixarene samples. The work here suggests that the disorder of the molecular crystal is a very important factor for the proton spin-lattice relaxation at cryogenic temperature. However, preliminary INS measurements on sample **VII** suggest that the efficient relaxation in quench cooled samples is not solely caused by methyl-groups with a distribution of hindering barriers, as was originally hypothesized [57][46].

Eleven calixarene complexes have been studied in order to determine

their suitability as cryorelaxors in cryoMAS NMR. The methyl-groups of the guest molecules remain mobile at cryogenic temperature due to quantum tunnelling. By binding a cryorelaxor complex to a larger molecule, the tunneling motion encourages relaxation in protons belonging to large molecules. This study has shown that despite the existence of freely rotating methyl-groups in some of the samples, the proton T_1 at low temperatures is too long, by at least an order of magnitude, for these complexes to be used practically as cryorelaxors. Deuteration of the host molecule has been shown to increase the efficiency of proton relaxation and reduce T_1 , however the reduction is small.

Molecular hydrogen confined to the cavity of aza-thia-open-cage fullerene has proved to be a very interesting model system for studying quantum dynamics. The ellipsoidal shape of the fullerene molecule causes the degeneracy of excited translational states to be lifted. Also due to the asymmetry of the cage, the hydrogen molecule experiences an anisotropic rotational potential, which causes splitting of translational states for hydrogen molecules with $J > 0$. Both of these effects have been directly observed by INS measurements.

Excitation peaks due to transitions between the translational ground state of parahydrogen and the rotational sub-levels of the translational ground state of orthohydrogen ($J = 0, L = 0 \leftrightarrow J = 1, L = 0$) have been identified. Studying the temperature dependence of these peaks has revealed that the relative populations of the rotational sub-levels in the $J = 1, L = 0$ state maintain a thermal equilibrium.

Analysis of the Q -dependence of the excitation peaks has aided in identification of the peak origins, and in determining the mean-squared displacement of the endohedral hydrogen molecule. The value of $\langle u^2 \rangle = 0.067 \pm 0.001 \text{ \AA}^2$ measured from fitting the $J = 1 \rightarrow J = 0$ peak at -13.2 meV shows remarkable agreement with the estimated value of $\langle u^2 \rangle = 0.069 \text{ \AA}^2$, calculated by treating the hydrogen molecule as a single particle in a spherical cavity of radius equal to the root-mean-squared radius of the ATOCF cavity.

The INS investigations described in this thesis have clearly demonstrated the feasibility of studying samples of relatively low mass and limited availability. It is hoped that this investigation will be the first in a line of studies on similar systems, including HD@ATOCF and H_2 confined in the spherical cavity of C_{60} ($\text{H}_2@C_{60}$).

Bibliography

- [1] CJ Pedersen. Cyclic polyethers and their complexes with metal salts. *Journal of the American Chemical Society*, 89:7017–7036, 1967.
- [2] CJ Pedersen. The discovery of crown ethers. *Angewandte Chemie International Edition in English*, 27:1021–1027, 1988.
- [3] JM Lehn. Supramolecular chemistry. *Angewandte Chemie*, 27:89–112, 1988.
- [4] JM Lehn. *Supramolecular Chemistry: Concepts and Perspectives*. VCH, 1995.
- [5] PD Beer, PA Gale, and DK Smith. *Supramolecular Chemistry*. Oxford University Press, 1999.
- [6] C David Gutsche. *Calixarenes: An Introduction*. RSC Publishing, 2nd edition, 2008.
- [7] MD Dresselhaus, G Dresselhaus, and PC Eklund. *Science of fullerenes and carbon nanotubes*. Academic Press, 1996.
- [8] Z Asfari, V Böhmer, J Harrowfield, and J Vincens, editors. *Calixarenes 2001*. Kluwer Academic Publishers, 2001.
- [9] HW Kroto, JR Heath, SC O'Brien, RF Curl, and RE Smalley. C₆₀: Buckminsterfullerene. *Nature*, 318:162–163, 1985.
- [10] JB Howard, JT McKinnon, Y Makarovsky, AL Lafleur, and ME Johnson. Fullerenes C₆₀ and C₇₀ in flames. *Nature*, 352:139–141, 1991.
- [11] Y Rubin, T Jarrosson, G Wang MD Bertberger, KN Houk, and G Schick. Insertion of helium and molecular hydrogen through the

- orifice of an open fullerene. *Angewandte Chemie International Edition*, 40:1543–1546, 2001.
- [12] Y Murata, M Murata, and K Komatsu. Synthesis, structure, and properties of novel open-cage fullerenes having heteroatom(s) on the rim of the orifice. *Chemistry - A European Journal*, 9:1600–1609, 2003.
- [13] Y Murata, M Murata, and K Komatsu. 100% encapsulation of a hydrogen molecule into an open-cage fullerene derivative and gas-phase generation of $\text{H}_2@C_{60}$. *Journal of the American Chemical Society*, 125:7152–7153, 2003.
- [14] K Komatsu, M Murata, and Y Murata. Encapsulation of molecular hydrogen in fullerene C_{60} by organic synthesis. *Science*, 307:238–240, 2005.
- [15] M Carravetta, A Danquigny, S Mamone, F Cuda, OG Johannessen, I Heinmaa, K Panesar, R Stern, MC Grossel, AJ Horsewill, A Samoson, M Murata, Y Murata, K Komatsu, and MH Levitt. Solid-state NMR of endohedral hydrogen-fullerene complexes. *Physical Chemistry Chemical Physics*, 9:4879–4897, 2007.
- [16] W Press. *Single-Particle Rotations in Molecular Crystals*. Springer-Verlag, 1981.
- [17] AJ Horsewill. Quantum tunnelling in the hydrogen bond. *Progress in Nuclear Magnetic Spectroscopy*, 52:170–196, 2008.
- [18] AJ Horsewill. Quantum tunnelling aspects of methyl group rotation studied by NMR. *Progress in Nuclear Magnetic Resonance Spectroscopy*, 35:359–389, 1999.
- [19] HS Gutowsky and GE Pake. Structural investigations by means of nuclear magnetism. *Journal of Chemical Physics*, 18:162–170, 1950.
- [20] CP Smyth. The dielectric constants of solids and molecular rotation. *Chemical Reviews*, 19:326–361, 1936.
- [21] N Bloembergen, EM Purcell, and RV Pound. Relaxation effects in nuclear magnetic resonance absorption. *Physical Review*, 73:679–712, 1948.

- [22] JH Van Vleck. The dipolar broadening of magnetic resonance lines in crystals. *Physical Review*, 74:1168–1183, 1948.
- [23] JG Powles and HS Gutowsky. Investigation of six tetrasubstituted methanes. *Journal of Chemical Physics*, 21:1695–1703, 1953.
- [24] JG Powles and HS Gutowsky. Solid solutions of t-butyl chloride in carbon tetrachloride. *Journal of Chemical Physics*, pages 1704–1709, 1953.
- [25] JG Powles and HS Gutowsky. Proton magnetic resonance of the CH₃ group. III. Reorientation mechanism in solids. *Journal of Chemical Physics*, 23:1692–1699, 1955.
- [26] EO Stejskal and HS Gutowsky. Proton magnetic resonance of the CH₃ group. IV. Calculation of the tunneling frequency and of T₁ in solids. *Journal of Chemical Physics*, 28:388–396, 1958.
- [27] EO Stejskal, DE Woessner, TC Farrar, and HS Gutowsky. Temperature dependance of T₁ in several molecular crystals. *Journal of Chemical Physics*, 31:55–65, 1959.
- [28] J Haupt. Einfluß von quanteneffekten der methylgruppenrotation auf die kernrelaxation in festkörpern. *Z. Naturforsch.*, 26a:1578, 1971.
- [29] B Alefeld, A Kollmar, and BA Dasannacharya. The one-dimensional CH₃-quantumrotator in solid 4-methyl-pyridine studied by inelastic neutron scattering. *Journal of Chemical Physics*, 63:4415–4417, 1975.
- [30] W Muller-Warmüth, R Schüler, M Prager, and A Kollmar. Rotational tunnelling in methylpyridines as studied by NMR relaxation and inelastic neutron scattering. *Journal of Chemical Physics*, 69:2382–2392, 1978.
- [31] M Prager and A Heidemann. Rotational tunneling and neutron spectroscopy: A compilation. *Chemical Review*, 97:2933–2966, 1997.
- [32] DK Ross. Hydrogen storage: The major technological barrier to the development of hydrogen fuel cell cars. *Vacuum*, 80:1084–1089, 2006.

- [33] AC Dillon, KM Jones, TA Bekkedahl, CH Kiang, DS Bethune, and MJ Heben. Storage of hydrogen in single-walled carbon nanotubes. *Nature*, 386:377–379, 1997.
- [34] PA Georgiev, DK Ross, A De Monte, U Montaretto-Marullo, RAH Edwards, AJ Ramirez-Cuesta, MA Adams, and D Colognesi. In situ inelastic neutron scattering studies of the rotational and translational dynamics of molecular hydrogen adsorbed in single-wall carbon nanotubes (SWNTs). *Carbon*, 43:895–906, 2005.
- [35] PA Georgiev, A Giannasi, DK Ross, M Zoppi, JL Sauvajol, and J Stride. Experimental Q-dependence of the rotational $J = 0$ -to-1 transition of molecular hydrogen adsorbed in single-wall carbon nanotube bundles. *Chemical Physics*, 328:318–323, 2006.
- [36] SA FitzGerald, T Yildirim, LJ Santodonato, DA Neumann, JRD Copley, JJ Rush, and F Trouw. Quantum dynamics of interstitial H₂ in solid C₆₀. *Physics Review B*, 9:6439–6451, 1999.
- [37] T Yildirim and AB Harris. Rotational and vibrational dynamics of interstitial molecular hydrogen. *Physical Review B*, 66:214301, 2002.
- [38] M Tomaselli and BH Meier. Rotational-state selective nuclear magnetic resonance spectra of hydrogen in a molecular trap. *Journal of Chemical Physics*, 115:11017–11020, 2001.
- [39] M Tomaselli. Dynamics of diatomic molecules confined in a chemical trap I. Nuclear magnetic resonance experiments on hydrogen in solid C₆₀. *Molecular Physics*, 101:3029–3051, 2003.
- [40] M Carravetta, OG Johannessen, MH Levitt, I Heinmaa, R Stern, A Samoson, AJ Horsewill, Y Murata, and K Komatsu. Cryogenic NMR spectroscopy of endohedral hydrogen-fullerene complexes. *Journal of Chemical Physics*, 124:104507, 2006.
- [41] SM McMurry. *Quantum mechanics*. Prentice Hall, 1993.
- [42] EM Purcell, HC Torrey, and RV Pound. Resonance absorption by nuclear magnetic moments in a solid. *Physical Review*, 69:37–38, 1946.
- [43] F Bloch. Nuclear induction. *Physical Review*, 70:460–474, 1946.

- [44] MH Levitt. *Spin Dynamics: Basics of Nuclear Magnetic Resonance*. Wiley, 2001.
- [45] G Davidson. *Group Theory for Chemists*. MacMillan, 1991.
- [46] KS Panesar, AJ Horsewill, F Cuda, M Carravetta, S Mamone, A Danquigny, MC Grossel, and MH Levitt. Thermal history effects and methyl tunnelling dynamics in a supramolecular complex of calixarene and para-xylene. *Journal of Chemical Physics*, 128, 2008.
- [47] GL Squires. *Introduction to the theory of thermal neutron scattering*. Cambridge University Press, 1978.
- [48] BH Bransden and CJ Joachain. *Quantum Mechanics*. Pearson Education, second edition, 2000.
- [49] J Natterer and J Bargon. Parahydrogen induced polarization. *Progress in Nuclear Magnetic Resonance Spectroscopy*, 31:293–315, 1997.
- [50] R Kimmich and E Anoardo. Field-cycling NMR relaxometry. *Progress in Nuclear Magnetic Resonance Spectroscopy*, 44:257–320, 2004.
- [51] E Fukushima and SBW Roeder. *Experimental Pulse NMR: A Nuts and Bolts Approach*. Addison-Wesley, 1981.
- [52] Q Xue. *Proton tunnelling in the hydrogen bond studied by NMR*. PhD thesis, University of Nottingham, 2003.
- [53] <http://www.ill.eu/instruments-support/instruments-groups/yellowbook/>.
- [54] H Mutka. Coupled time and space focusing for time-of-flight inelastic scattering. *Nuclear Instruments & Methods in Physics Research*, 338:144–150, 1994.
- [55] R Scherm, C Carlile, J Dianoux, J Suck, and J White. Another time of flight spectrometer? Technical Report 76S235S, ILL, 1976.
- [56] R Caciuffo, G Amoretti, CJ Carlile, F Fillaux, O Francescangeli, M Prager, and F Ugozzoli. Methyl group tunnelling studies in calixarenes. *Physica B*, 202:279–286, 1994.

-
- [57] AJ Horsewill. Unpublished.
- [58] W Wu, DL Noble, JR Owers-Bradley, and AJ Horsewill. A ^{13}C field-cycling NMR relaxometry investigation of proton tunnelling in the hydrogen bond. *Journal of Magnetic Resonance*, 175:210–221, 2005.
- [59] AJ Horsewill, KS Panesar, S Rols, MR Johnson, Y Murata, K Komatsu, S Mamone, A Danquigny, F Cuda, S Maltsev, MC Grossel, M Carravetta, and MH Levitt. Quantum translator-rotator: Inelastic neutron scattering of dihydrogen molecules trapped inside anisotropic fullerene cages. *Physical Review Letters*, 102:013001, 2009.
- [60] PF Newhouse and KC McGill. Schrodinger equation solutions that lead to the solution for the hydrogen atom. *Journal of Chemical Education*, 81:424–426, 2004.
- [61] CP Slichter. *Principles of Magnetic Resonance*. Springer-Verlag, 3rd edition, 1963.
- [62] AIM Rae. *Quantum Mechanics*. IOP Publishing, fourth edition, 2002.
- [63] JS Arellano, LM Molina, A Rubio, and JA Alonso. Density functional study of adsorption of molecular hydrogen on graphene layers. *Journal of Chemical Physics*, 112:8114–8119, 2000.